NOVA SCHOOL OF SCIENCE & TECHNOLOGY

DEPARTMENT OF MECHANICAL AND INDUSTRIAL ENGINEERING

JOÃO MIGUEL CORREIA DOS SANTOS LOPES

Bachelor of Science in Mechanical Engineering

NUMERICAL SIMULATION OF 3D FLUID-STRUCTURE INTERACTION IN FLOATING WAVE ENERGY CONVERTER DEVICES

MASTER IN MECHANICAL ENGINEERING

NOVA University Lisbon
September, 2022

NOVA SCHOOL OF SCIENCE & TECHNOLOGY

DEPARTMENT OF MECHANICAL AND INDUSTRIAL ENGINEERING

NUMERICAL SIMULATION OF 3D FLUID-STRUCTURE INTERACTION IN FLOATING WAVE ENERGY CONVERTER DEVICES

JOÃO MIGUEL CORREIA DOS SANTOS LOPES

Bachelor of Science in Mechanical Engineering

Adviser: PhD Moisés Gonçalves de Brito
Invited Assistant Professor, Department of Mechanical and Industrial Engineering, NOVA School of Science and Technology

Co-adviser: MSc Francisco Ramos Bernardo
Researcher, Department of Mechanical and Industrial Engineering, NOVA School of Science and Technology

Examination Committee

Chair: PhD José Fernando de Almeida Dias
Associate Professor, NOVA University Lisbon

Rapporteur: PhD Maria da Graça Reis e Silva de Oliveira Neves
Associate Professor with Aggregation, NOVA University Lisbon

Adviser: PhD Moisés Gonçalves de Brito
Invited Assistant Professor, NOVA University Lisbon

MASTER IN MECHANICAL ENGINEERING

NOVA University Lisbon
September, 2022

Numerical simulation of 3D fluid-structure interaction in floating wave energy converter devices

This document was created with the (pdf/Xe/Lua)LaTeX processor and the NOVAthesis template (v6.9.6) [1].

To my family and friends.

Acknowledgements

First and foremost, I would like to acknowledge my supervisor, Professor Moisés Gonçalves de Brito, for his expertise and unquantifiable support. The constant availability and willingness to help were crucial for the development of this thesis.

I would also like to acknowledge my co-supervisor, Francisco Ramos Bernardo, for all the advices, exchanged ideas and help provided.

I wish to acknowledge Nova School of Science and Technology (FCT NOVA) and the Department of Mechanical and Industrial Engineering (DEMI) for providing the facilities and resources required throughout the course and, specifically, for the development of this thesis.

I would like to thank my long time friends for their valuable friendship and for always believing in me.

To my university friends, thank you for entering my life and for being part of the best memories I will keep of these five years. Your fellowship was key to keep me motivated in the times of struggle and your sincere friendship is, without a doubt, the reason for all the unforgettable moments of joy we shared together.

I would especially like to thank my girlfriend, Rita, for her immeasurable support, love and commitment.

Finally, I would like to express my sincere gratefulness to my family, particularly my parents, for providing me this opportunity despite all the necessary sacrifices.

"The winds and waves are always on the side of the ablest navigators." (Edward Gibbon)

Abstract

Global energy consumption and, consequently, energy related carbon dioxide (CO_2) emissions have been increasing in the last few decades. Currently, the large majority of countries cover most of their energy needs with fossil fuels, contributing for CO_2 emissions to the atmosphere, which have a strong impact on global warming. Recently, there has been growing concern about the significant increase in energy demands and environmental pollutants emissions by worldwide governments and organizations, resulting in the implementation of policies that promote the investment in non-polluting natural resources.

The need to diversify the available renewable energy sources intensified the interest in ocean renewable energy. Research and development (R&D) of devices capable of extracting energy from the oceans (waves, wind, currents, tides) and transform it into electrical energy has, therefore, been one of the main focus of ocean engineering in recent years. Wave energy technology is not recent but, as opposed to wind and solar energy, it is still lacking a design convergence, contributing for a higher levelized cost of energy (LCOE), when compared to other sources. Wave energy technology has a strong potential of development and may have a fundamental contribution on achieving carbon neutrality and satisfying the increasing global energy demand.

One of the main challenges of offshore renewable energies is to reduce costs, common to both wave and wind energy. Consequently, the incentive to couple semisubmersible platforms (SSPs), for the support of offshore wind turbines, and wave energy converters (WECs) emerges, allowing the reduction of installation costs. Although there are many advantages, the coupling of WECs with offshore wind turbines also introduces the influence of the interaction between both, resulting in a complex hydrodynamic system.

Therefore, this work consists in studying a WEC which can be coupled with a floating SSP. The study is performed using the OpenFOAM software, augmenting its functionalities using olaFlow's library for the generation and propagation of waves. In this context, the objectives of this thesis are: i) validation of the numerical model using experimental data from literature; ii) analysis of large amplitudes of motion effects of the device; iii) study of regular wave interaction with the wave energy hyperbaric converter (WEHC)

device; iv) study of irregular wave interaction with the WEHC device; and v) study of the influence of the WEHC power take-off (PTO) damping characteristics.

In the first part of this study the validation of wave generation and propagation is executed, comparing the wave parameters of simulated regular waves with analytical values. After the validation, a mesh convergence study is done.

Afterwards, regular wave interaction with the WEC device is studied. First, a free heave and pitch decay tests are carried out to calculate the WEC's natural period. Then, simulations without the PTO system are performed, enabling the characterization of the WEC's behaviour for the different maritime conditions considered. The obtained results allow to conclude that the WEC is in resonance with the waves for frequencies around 0.20 Hz. It is also observed that both the heave amplitude and the pitch angle present small variations for shorter period waves. The influence of the pitch angle on the WEC's heave amplitude is also studied.

After, simulations with the PTO system are carried out, with results about the extracted power and optimal PTO's linear damping coefficient being obtained. A power curve in function of the PTO's linear damping coefficient, for each case considered, is presented.

Finally, irregular wave interaction with the WEC device is studied. The influence of the PTO system when the WEC is under irregular waves is characterized.

Keywords: Fluid-structure interaction (FSI), OpenFOAM, Floating WECs, Numerical modelling

Resumo

O consumo global de energia e, consequentemente, as emissões de CO_2 derivadas da sua produção, têm vindo a aumentar nas últimas décadas. Atualmente, a maioria dos países asseguram a maior parte das suas necessidades energéticas com recurso a combustíveis fósseis, contribuindo para as emissões de CO_2 para a atmosfera, que têm um enorme impacto no aquecimento global. Recentemente, tem havido um crescente interesse sobre o aumento significativo das necessidades energéticas e emissão de gases poluentes, por parte de governos e organizações mundiais, resultando na implementação de políticas que promovem o investimento em recursos naturais não-poluentes.

A necessidade de diversificar as fontes de energia renováveis disponíveis intensificou o interesse nas energias renováveis provenientes dos oceanos. A investigação e desenvolvimento de dispositivos capazes de extrair energia dos oceanos (ondas, vento, correntes, marés) e transformá-la em energia elétrica tem sido, assim, um dos principais temas de estudo da engenharia dos oceanos em anos recentes. A tecnologia da energia das ondas não é recente mas, ao contrário da energia solar e do vento, ainda não tem uma configuração comum estabelecida, contribuindo para um maior custo nivelado da energia, quando comparado a outras fontes. A tecnologia da energia das ondas tem um enorme potencial de desenvolvimento e pode ter um contributo fundamental para atingir a neutralidade carbónica e satisfazer o aumento das necessidades energéticas globais.

Um dos principais desafios das energias renováveis *offshore* é reduzir custos, comum tanto à energia das ondas como do vento. Consequentemente, surge o incentivo de acoplar plataformas semi-submersíveis, para o suporte de turbinas eólicas *offshore*, e WECs, permitindo a redução dos custos de instalação. Apesar de existirem imensas vantagens, o acoplamento de WECs com turbinas eólicas *offshore* introduz a influência da interação entre ambos, resultando num sistema hidrodinâmico complexo.

Desta forma, este trabalho consiste no estudo de um WEC que pode ser acoplado a uma SSP flutuante. O estudo é realizado com recurso ao software OpenFOAM, aumentando as suas funcionalidades utilizando a biblioteca olaFow para a geração e propagação das ondas. Assim, os objetivos desta dissertação são: i) validar o modelo numérico com recurso a dados experimentais da literatura; ii) analisar os efeitos das grandes amplitudes

de movimento do dispositivo; iii) estudar a interação do WEC com ondas regulares; iv) estudar a interação do WEC com ondas irregulares; e v) estudar a influência das características de amortecimento do sistema de PTO.

Na primeira parte deste estudo a validação da geração e propagação das ondas é realizada, comparando parâmetros das ondas regulares simuladas com valores analíticos. Após a validação é realizado um estudo de independência da malha.

Em seguida, foi estudada a interação do WEC com ondas regulares. Primeiro, foram realizados testes de decaimento com afundamento e arfagem livres, de forma a calcular o período natural do WEC. Depois, simulações sem o sistema de PTO são realizadas, permitindo a caracterização do comportamento do WEC para as diferentes condições marítimas consideradas. Os resultados obtidos permitem concluir que o WEC entra em ressonância com as ondas para frequências por volta dos 0.20 Hz. Também é observado que tanto o afundamento como a arfagem do WEC apresentam pequenas variações para ondas de períodos mais curtos. A influência da arfagem nos movimentos de afundamento do WEC é também estudada.

Depois, simulações com o sistema de PTO são realizadas, com resultados sobre a potência extraída e o valor ideal do coeficiente linear de amortecimento a serem obtidos. É também apresentada uma curva de potência, em função do coeficiente linear de amortecimento do PTO, para cada caso considerado.

Por fim, foi estudada a interação do WEC com ondas irregulares. A influência do sistema de PTO, quando o WEC interage com ondas irregulares, é caracterizada.

Palavras-chave: Interação fluido-estrutura (FSI), OpenFOAM, WECs flutuantes, Modelação numérica

Contents

Appendices

List of Figures

List of Tables

List of Listings

Acronyms

BC	boundary condition
CFD	computational fluid dynamics
CWR	capture width ratio
DIC	diagonal incomplete-Cholesky
DoF	degrees of freedom
FEM	finite element method
FSI	fluid-structure interaction
FVM	finite volume method
GAMG	generalised geometric-algebraic multi-grid
GUI	graphical user interface
JONSWAP	joint north sea wave project
LCOE	levelized cost of energy
MPI	message passing interface
MULES	Multidimensional Universal Limiter for Explicit Solution
NWT	numerical wave tank
O&M	operation and maintenance
OpenFOAM	Open Source Field Operation and Manipulation
OWC	oscillating water column
OWSC	oscillating wave surge converter

PCG	preconditioned conjugate gradient
PISO	pressure-implicit with splitting of operators
PTO	power take-off
R&D	research and development
RANS	Reynolds-averaged Navier-Stokes
RAO	response amplitude operator
SIMPLE	semi-implicit method for pressure-linked equations
SPH	Smooth Particle Hydrodynamics
SSP	semisubmersible platform
VARANS	volume-averaged Reynolds averaged Navier-Stokes equations
VOF	volume-of-fluid
WEC	wave energy converter
WEHC	wave energy hyperbaric converter

Symbols

a	wave amplitude (L)
A_χ	normalized amplitude error (-)
A_p	cross section area of the pump piston (L^2)
α	phase fraction (-)
α_E	energy scale (-)
b	distance between the pump piston and the lever arm rotation point (L)
β	wave angle of incidence (-)
c	wave phase speed ($L\ T^{-1}$)
C_o	Courant number (-)
C_{PTO}	angular damping coefficient ($M\ L^2\ T^{-1}$)
c_{PTO}	linear damping coefficient ($M\ T^{-1}$)
χ_i	magnitude of the signal (-)
d	still water depth (L)
D_{50}	mean nominal diameter (L)
E	floater efficiency (L^{-1})
ν_t	eddy viscosity ($L^2\ T^{-1}$)
$\varepsilon_{i,21}$	changes between medium and fine parameters (-)
$\varepsilon_{i,32}$	changes between coarse and medium parameters (-)
η	free surface elevation (L)
η_M	measured elevation at the wave maker (L)
η_R	reflected wave height (L)
η_T	target elevation at the wave maker (L)
f	frequency (T^{-1})
$F_e(t)$	wave incident force ($M\ L\ T^{-2}$)

$F_f(t)$	total force applied on the floater (M L T^{-2})
F_i^{ST}	surface tension force (M T^{-2})
$F_p(t)$	PTO force (M L T^{-2})
f_{peak}	peak frequency (T^{-1})
g	gravitational acceleration (L T^{-2})
$G(f)$	peak-enhancement function (-)
g_i	acceleration vector due to gravity (L T^{-2})
γ	peak-enhancement factor (-)
F_i	generic force (M L T^{-2})
H	wave height (L)
H_s	significant wave height (L)
J	propagated wave power per unit width of a wavefront (M L^2 T^{-3})
k	wave number (L^{-1})
K_{PTO}	angular spring coefficient (M L^2 T^{-2})
KC	Keulegan–Carpenter number (-)
λ	wave length (L)
δ	logarithmic decrement (-)
m	number of cycles (-)
m_f	buoy mass (M)
N	number of samples (-)
ω	wave angular frequency (T^{-1})
ω_d	damped frequency (T^{-1})
ω_n	natural frequency (T^{-1})
P_a	averaged absorbed power (M L^2 T^{-3})
p^*	pseudo-cc pressure (M L^{-1} T^{-2})
p_c	pump actuator pressure (M L^{-1} T^{-2})
ϕ	porosity (-)
ϕ_a	represents any variable (-)
ϕ_a^{00}	represents the variable's values at previous time steps (-)
p	pressure (M L^{-1} T^{-2})
ψ	generic flow variable (-)

ψ'	fluctuating value of ψ (-)
$\overline{\psi}$	mean value of ψ (-)
ρ	density (M L^{-3})
R_i	convergence ratio (-)
$S_\eta(f)$	free surface elevation power spectrum (L^2 T)
$\hat{S}_{i,1}$, $\hat{S}_{i,2}$, $\hat{S}_{i,3}$	solutions with fine, medium and coarse input parameters (-)
$S_\theta(f)$	pitch angle power spectrum (T)
$S_y(f)$	heave amplitude power spectrum (L^2 T)
σ	peak-width parameter to account for the slightly different widths on the two sides of the spectral peak (-)
σ_{ij}	stress tensor (M L^{-1} T^{-2})
ϵ_{ij}	strain (T^{-1})
T	wave period (T)
t	time (T)
T_d	damped period (T)
T_n	natural period (T)
T_p	peak wave period (T)
τ_{ij}	viscous stress tensor (M L^{-1} T^{-2})
θ	rotation angle of the WEC (-)
$\dot{\theta}$	angular velocity of the WEC (T^{-1})
C, α_t, β_t	tuning factors (-)
μ_t	turbulent viscosity (M L^{-1} T^{-1})
$\mathbf{U}$	velocity vector (L T^{-1})
u	velocity component (L T^{-1})
U_c	correction velocity applied to a vector perpendicular to the boundary (L T^{-1})
μ_{eff}	effective viscosity (M L^{-1} T^{-1})
μ	dynamic viscosity (M L^{-1} T^{-1})
$v_f(t)$	velocity of the floater (L T^{-1})
ε	wave steepness (-)
φ_χ	normalized phase error (-)
X	position vector in cartesian coordinate system (L)
x	position component (L)
x_i, x_{i+1}	first and last amplitude (displacement) (-)

ξ	damping factor (-)

1

Introduction

This chapter provides an overview of the thesis. This first section explains the motivation behind the theme selection. The objectives are defined and the adopted methodology to complete the work is presented. At last, the structure followed along the thesis is presented.

1.1 Motivation

Global energy consumption and, consequently, energy related CO_2 emissions have been increasing in the last few decades and, due to population and economic growth, these numbers will only continue to rise. If there is no change in the current applied policies and used technologies, the global energy use is expected to increase by nearly 50% until 2050, in comparison with the values of 2020 [2].

Currently, the large majority of countries cover most of their energy needs with fossil fuels, making them the primary source of energy consumed globally. Processes for energy production using fossil fuels sources have a negative environmental impact, contributing for CO_2 emissions to the atmosphere, which have a strong impact on global warming.

In recent years, following the signing of the Kyoto Protocol [3] and the Paris Climate Change Agreement [4], there has been a growing concern about the significant increase in energy demands and environmental pollutants emissions by worldwide governments and organizations, resulting in the implementation of policies that promote the investment in non-polluting natural resources [5]. Nonetheless, more progress has to be made in order to reduce greenhouse gases emissions, which is one of the main challenges of the 21st century.

In order to achieve the objectives proposed in the Paris Agreement, a major part of the total energy produced globally will have to result from renewable sources by 2050. The oil crisis of 1973 triggered a worldwide interest in renewable sources for the production of electrical energy, with the idea of harvesting energy from the sun, wind and oceans using large-scale energy production being promoted, forever changing the paradigm of these resources. Solar and wind have become well established technologies in the energy

market, on the other hand, wave energy has had difficulties in following the same path of success.

However, wave energy offers some advantages, when compared to solar and wind, such as: it offers the advantage of being consistent throughout the day and night, increasing predictability, and has a higher density of energy which contributes to increase the global energy yield per unit area of marine space, contributing to a better use of the natural resources. Wave energy technology has a strong potential of development and may have a fundamental contribution on achieving carbon neutrality and satisfying the increasing global energy demand [6]. R&D of devices capable of extract energy from the oceans (waves, wind, currents, tides) and transform it into electrical energy has, therefore, been one of the main focus of ocean engineering in recent years, both in industry and academia.

Wave energy technology is not recent, as the first ever patent was filed around 200 years ago. Nonetheless, a major part of the R&D only happened in the last 40 years, with countless WECs designs being presented [7]. The wave energy sector, as opposed to wind and solar energy, is still lacking a design convergence, with several different technologies being continually studied and developed [8]. This factor dilutes the scarce available financial resources and may be the reason for a higher LCOE, when compared to other sources.

Offshore renewable energies include both wave and wind energy. These renewable energy sources face similar challenges, nonetheless, they are not equally developed. While offshore wind energy, with 25 GW of installed capacity in Europe [9], is an established technology transferred from the extensive research on the aerodynamic field of onshore wind blades [10] and from technology used in oil and gas industries on offshore support structures [11, 12], wave energy is still a developing technology. In order to improve the exploration of natural resources, promoting a sustainable development of offshore wave and wind energies, devices efficiency has to be assured.

Consequently and due to the challenge of reducing costs, common to both industries, the incentive to couple SSPs, for the support of offshore wind turbines, and WECs emerges. Recent studies focus on studying this type of coupled platforms [13, 14], which result in hybrid SSPs, allowing the reduction of installation costs, due to the sharing of electric grid connections, support platforms and mooring systems. The most known hybrid SSPs are the WindWaveFloat and W2Power concepts, nevertheless there are many other studied concepts [10].

Although there are many advantages, the coupling of WECs with offshore wind turbines also introduces the influence of the interaction between both, resulting in a complex hydrodynamic system. Pitch and roll movements affect the structural integrity of wind turbines, as they induce large external loads on the structures and reduce the fatigue life of devices. Zhu and Hu [15] mention that a variation of five degrees on the pitch angle will cause a 50% increase in the sectional modulus of a blade to avoid fatigue failure.

Therefore, deepening the knowledge about the loads that these structures are submitted when under the influence of maritime agitation, current and wind is of utmost importance for the accurate project of hybrid devices. FSI phenomenons are of great importance in many areas of science and engineering, however, due to their strong nonlinear and multidisciplinary nature, they are still not fully comprehended, being only possible to consider rigid structures or with minimal deformations, in numerical studies [16]. Numerical simulation has been working as a tool to support scientific research, in order to improve the comprehension of this type of phenomenons [17–22].

This work consists in studying a WEC which can be coupled with a floating SSP for the support of offshore wind turbines, as illustrated in Figure 1.1. Recent numerical studies have shown advantages in installing the WECs concentrically [23, 24].

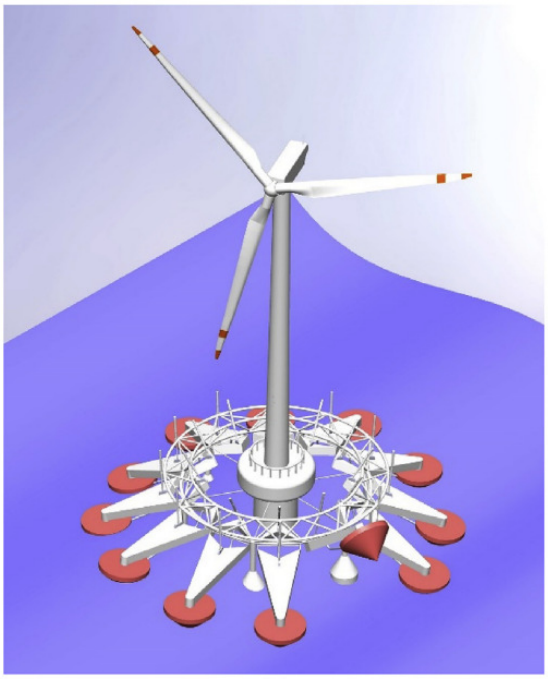

Figure 1.1: Concentrically installed WECs array on a floating SSP, adapted from [13].

The WEC in study is a WEHC. This type of WEC is composed of three different subsystems: floater, lever and a hydraulic PTO system which is responsible for converting the waves' energy, absorbed by the device, in electrical energy. This system is based in a hydraulic system which consists of a hydraulic pump, a hydropneumatic accumulator, connected to a hyperbaric chamber, and a Pelton turbine. A simplified scheme of the WEHC is shown in Figure 1.2.

The working principle of a WEHC is based on the oscillatory movement of the floater-lever group, caused by the waves action. This oscillatory movement drives the hydraulic pump which pumps fresh water, from a closed circuit, to a hydropneumatic accumulator at a very high pressure.

The hydropneumatic accumulator, connected to the hyperbaric chamber, is used to

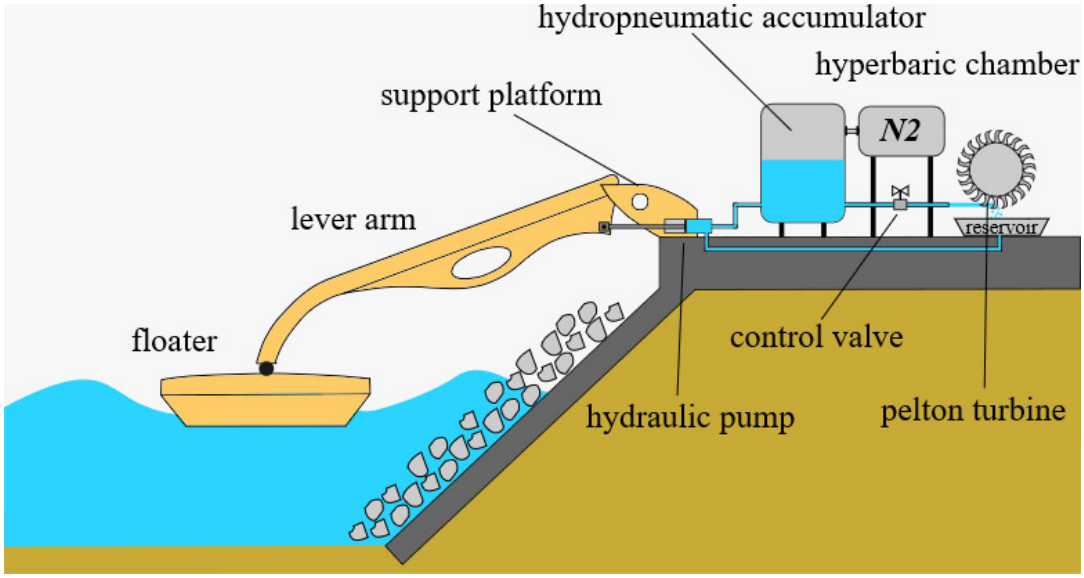

Figure 1.2: Energy conversion system scheme.

store the fluid at very high pressures. The water flow is pumped intermittently by the hydraulic pump, whereby this group enables the stabilization of the flow released to the power generation unit.

In the power generation unit, the water maintained in the hydropneumatic accumulator is expelled with a stable flow and as a high speed jet to activate a Pelton turbine. The mechanical energy in the turbine is transformed in electrical energy by an electrical generator [25].

1.2 Objectives

The main objective of the present work is to study the hydrodynamic behaviour of a WEHC. In order to achieve the main objective, this works aims to complete some specific goals, namely:

- Validation of the numerical model;
- Analysis of large amplitudes of motion effects of the device;
- Study of regular wave interaction with the WEHC device;
- Study of irregular wave interaction with the WEHC device;
- Lastly, study of the influence of the WEHC PTO damping characteristics.

1.3 Methodology

The work methodology is essentially based in numerical study. All the numerical simulation process is executed using the open-source computational fluid dynamics (CFD)

software OpenFOAM (Open Source Field Operation and Manipulation), augmenting its functionalities using olaFlow's library for the generation and propagation of waves. The computational domain mesh is generated using Workbench software. Obtained results are processed using Paraview software and Python programming language.

The adopted methodology is divided in four phases. In the first phase, relevant literature regarding the combined exploration of waves and offshore winds, several different WECs technologies, operation principle of the WEHC and about floating hybrid devices is reviewed. Different approaches to simulate fluid-structure interaction and the Reynolds-averaged Navier-Stokes (RANS) equations are also reviewed. The second phase focuses on the description of the numerical model.

The third phase contains a mesh convergence study. This phase can be divided in two stages: first, the validation of wave generation and propagation, then WEC parameters for the different meshes are compared, enabling the choice of the mesh used for the following simulations.

In the last phase, the hydrodynamic behaviour of the WEC is studied. First, a free heave and free pitch decay test is carried out, allowing the calculation of the heave and pitch natural period. Next, the velocity and pressure fields of these tests are studied.

Afterwards, the simulations of the WEC interacting with regular waves, without PTO (free moving floater) system, are analysed. The characterization of the hydrodynamic behaviour of the device, without mechanical constraints, allows to compare these results with the ones from the simulations with PTO system. The influence of the PTO system on the hydrodynamic behaviour of the WEC is, then, characterized.

Finally, the hydrodynamic behaviour of the WEC interacting with irregular waves is studied. Cases with and without PTO systems are analysed.

1.4 Thesis Outline

This thesis is divided in seven chapters. A brief description of the contents of each chapter is given bellow:

Chapter 1, Introduction, provides an overview of the research work. The objectives are defined and the methodology followed to complete this work is enunciated. Finally, the contents of this thesis are presented.

Chapter 2, Literature review, describes the combined exploration of waves and offshore winds, several different WEC technologies that can be implemented in hybrid devices, presents various concepts of floating hybrid devices and describes the main components of the WEHC and its working principle. The location where the WEHC device could be installed and the simulations maritime conditions are also presented. Next, a comparison between different approaches to simulate fluid-structure interaction and the RANS equations are reviewed. Finally, a review focuses on regular and irregular wave theories.

Chapter 3, Description of the numerical model, presents a brief introduction of OpenFOAM. The olaFlow library, the discretization method used in the simulations, the mesh generation guidelines, the boundary conditions and the motion of the WEC is described. Finally, the solving procedure and simulation parameters are presented.

Chapter 4, Validation of the numerical model, contains a mesh convergence study. First, a validation of wave generation and propagation is performed. After, WEC parameters for the different meshes are compared.

Chapter 5, Regular wave interaction with the WEC device, contains a free heave and free pitch decay test. It focuses on the analysis of the simulations, with and without PTO system, when the WEC is interacting with regular waves.

Chapter 6, Irregular wave interaction with the WEC device, focuses on studying the WEC when interacting with irregular waves.

Chapter 7, Conclusions and Future Developments, summarises the developed work in the present thesis. Main conclusions are drawn from the obtained results and new developments and themes to follow in future works are proposed.

2

Literature review

2.1 Introduction

Wave and offshore wind industries share the same hostile marine environment. Moreover, the requirement for both industries to reduce costs, together with the need of promoting a sustainable exploration of marine natural resources, provides the incentive for combining the exploration of waves and offshore winds. Wave and wind energy devices are coupled in SSPs with the objective of taking advantage of the synergetic effects.

These synergies contribute to reduce the LCOE, due to: shared electric grid infrastructure, which represents up to one third of the costs of an offshore project; shared logistics, contributing to reduce costs due to sharing of expensive specialist marine equipment and facilities; common support structures, reducing construction costs; shared operation and maintenance (O&M), allowing the shared use of specialised technicians and dedicated installations, ensuring an effective O&M and thereby maximising the working time of the equipment. In addition, these synergies also contribute to an increased quality of the delivered power to the grid, as a result of: enhanced predictability of power output, as wave energy is less variable than wind energy; smoother power output, as for the same weather system the wind peaks trail the wave climate peaks, reducing the sudden disconnections from the electric grid and consequently increasing the number of activity hours [10].

On the other hand, wave and wind devices have also been combined to improve the hydrodynamic stability of SSPs, with the WECs contributing to attenuate movements and improve stability, especially in the case of pitching motions, in addition to their main purpose of producing energy from the waves. Although platforms are designed with good hydrodynamic stability, external forces applied by wind, waves and currents can, however, cause undesired heave and pitch motion, which induces large external loads on structures and reduce the fatigue life of devices on the platforms [26]. For example, a variation of five degrees on the pitch angle will cause a 50% increase in the sectional modulus of a blade to avoid fatigue failure [15] thus, floating platforms must have reasonably small pitching motions in order to be reliable. Recently, studies found that WECs considerably contribute to the reduction of these motions [15, 27].

2.1.1 WEC technology for hybrid devices

A good understanding of WEC technologies is crucial for the development of combined wave and wind devices. Currently, there are several WECs devices and, based on their principle of energy capture, they can be classified into: oscillating water column (OWC), oscillating bodies and overtopping devices. A brief description of the different WECs types is provided bellow.

2.1.1.1 Oscillating water column

OWCs are built with a semi-submerged chamber, keeping a trapped air pocket above a column of water. Its working principle is based on the entry of waves in the structure, causing the water column to act like a piston, moving up and down and thereby forcing the air out of the chamber and back into it. This continuous movement generates a reversing stream of high-velocity air, which is channelled through a turbine-generator group to produce electricity [28]. The main advantage of these devices lies in their reliability, as these are simple and well-proven devices with no moving parts, other than the air turbine. Some examples of OWCs are: Pico Plant (Azores, Portugal), Mutriku (Spain) and OE Buoy. The Pico plant and Mutriku OWCs are shown in Figure 2.1.

Figure 2.1: Pico plant, view from the sea (left); and Mutriku breakwater-mounted OWC (right).

2.1.1.2 Oscillating bodies

Oscillating bodies devices include all of those conversion devices that collect the wave energy through a body, usually a floater or a buoy, which is forced to maintain an oscillatory movement, i.e., a heave, roll, or pitch motion. These devices are either floating or bottom fixed. The several concepts designed to transform the oscillatory movement into electricity have resulted in several different PTO systems, such as: hydraulic generators, linear electric generators or piston pumps.

The main advantage of these systems is their small size and the fact that most of them are floating devices, which makes them very versatile. Nevertheless, more research should be carried out in order to reach a clear technology and to increase the PTO's

performance. Some examples of oscillating devices are: Pelamis, PowerBuoy, Oyster and WaveStar. Pelamis and Oyster devices are shown in Figure 2.2.

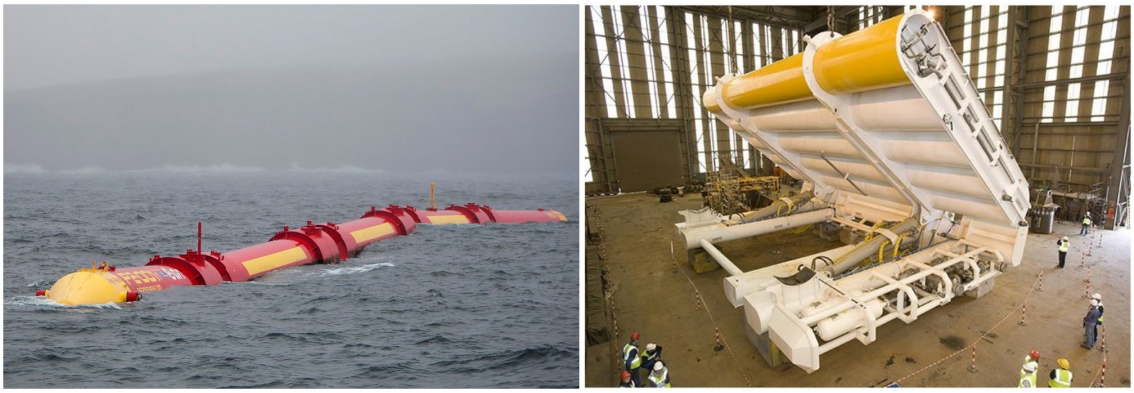

Figure 2.2: Examples of oscillating body devices: Pelamis (left) and Oyster (right).

2.1.1.3 Overtopping devices

Overtopping devices can produce electricity by transforming the potential energy, due to the height of collected water above the sea surface, into electricity using conventional low head hydro turbines [29]. As waves arrive at the device, they overtop a ramp structure and are kept in the reservoir.

The main advantage of these systems is their simplicity, i.e., they store water and, when there is enough stored, they let it pass through a turbine. On the other hand, its main disadvantages lies in their low head (1-2 m) and the large dimensions that a full-scale overtopping device would have. Some examples of this technology include devices such as: Tapchan, Wave Dragon and Seawave Slot-Cone Generator. The Tapchan and SeaWave Slot-Cone generator devices are shown in Figure 2.3.

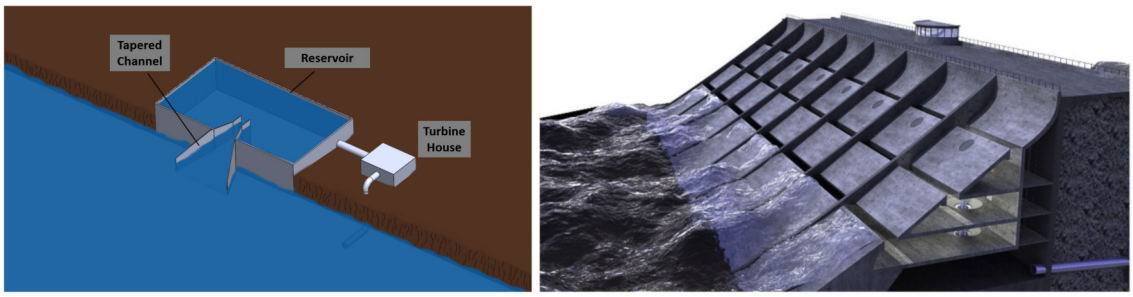

Figure 2.3: Examples of overtopping devices: Tapchan (left) and SeaWave Slot-Cone generator (right).

2.1.2 Floating hybrid devices

The most known hybrid SSP concepts are the WindWaveFloat and W2Power. A more recent concept is the three OWC multi-use floating platform.

The WindWaveFloat project is dedicated to the integration of several different WEC devices on the WindFloat (a tri-column type SSP) [30]. The first WEC device is made of a single spherical floater located at the center of the platform, being attached to it by three lines. The second one includes two OWCs in which the water moves within chambers created around two columns of the SSP, with the third column supporting the wind turbine. The third and fourth devices consist of three oscillating wave surge converters (OWSCs) and three point absorbers assembled on top of the main beams of the SSP structure, respectively. More details about the different devices are shown in Figure 2.4.

Figure 2.4: Example of the several WEC devices integrated in the WindFloat platform: (a) a single spherical floater, (b) two OWC, (c) three oscillating surge converters and (d) three point absorbers.

The W2Power concept is made of two wind turbines, each one assembled on top of one column of the SSP. Linear arrays of point absorbers are attached on each side of the platform, driving the PTO system with fluid, located at the third column of the SSP. See Figure 2.5 for more details.

In addition, other concept of an hybrid SSP platform was proposed, presenting a different layout: a square shaped arrangement, of four columns. Each of the wind turbines are attached on top of one column, while the WECs are suspended bellow and supported by the top main beams [31].

2.2 Overview of the WEHC system

The operation of a WEHC is entirely dependent on the action of waves on the floater and the pressure specified for the hyperbaric chamber. This type of WEC can be divided in

Figure 2.5: W2Power concept: (a) W2Power platform and (b) point absorbers attached on the W2Power platform.

three different sub-systems: floater, lever arm and a hydraulic PTO system. Figure 2.6 shows the main components of a WEHC.

The floater heave displacement, caused by the waves, is transferred by the lever arm into axial displacement on the hydraulic pump. The lever arm multiplies the forces applied on the floater, increasing the pumping pressure capacity considerably.

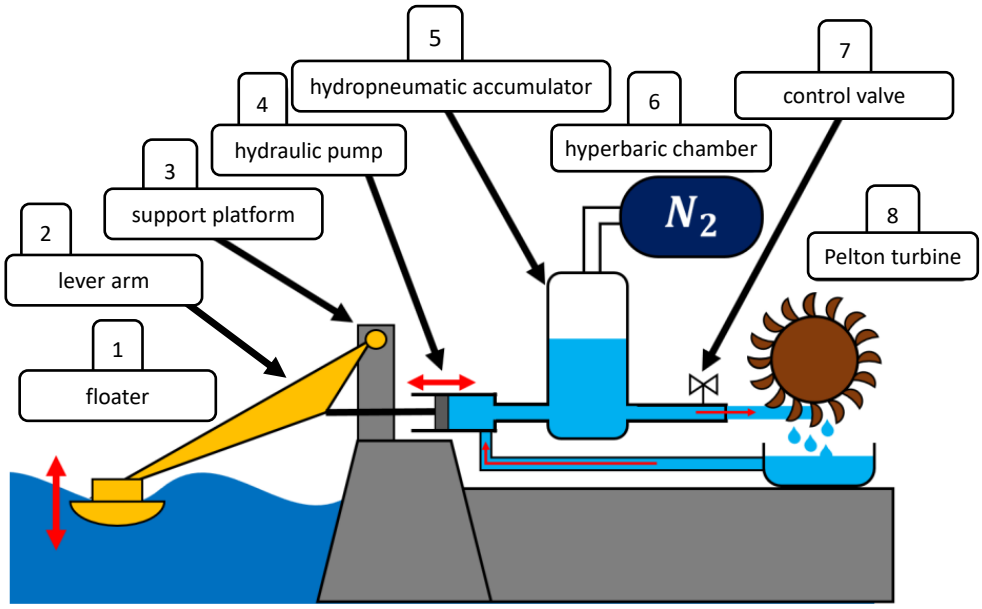

Figure 2.6: WEHC scheme, adapted from [32].

The PTO system is responsible for transforming the kinetic energy, transferred from the waves to the floater-lever arm group, into electrical energy. The oscillatory movement

of the floater-lever arm group drives the hydraulic pump. The high pressure water is pumped inside a closed-circuit to the hydropneumatic accumulator, which is also connected to a hyperbaric chamber filled with gas (N_2). This high pressure system works as a stabilizer for the intermittent feed of water from the pump. The control valve expels, with a stable flow, at high speeds and as a jet, the water maintained in the hydropneumatic accumulator, driving the Pelton turbine connected to an electrical generator [33]. The generator transforms the mechanical energy in the turbine into electrical energy.

2.2.1 Coordinate system

In order to characterize the movement of the WEC, a coordinate system needs to be defined first. Therefore, the classic model of a free floating body is first presented.

The WEC's position is defined by a cartesian coordinate system, with origin in the free surface plane. Figure 2.7 shows the six degrees of freedom (DoF) of a free floating body. It is considered that the waves are propagating along X-axis.

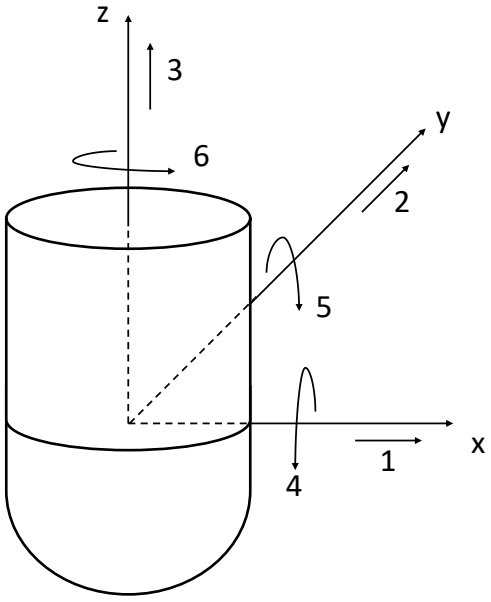

Figure 2.7: The six degrees of freedom of a free floating body.

The floating body is free to move in all six of its DoF, three translational and three rotational, as shown in Figure 2.7, where: 1 - surge, represents the horizontal movement along X-axis; 2 - sway, represents the horizontal movement along Y-axis; 3 - heave, represents the vertical movement along Z-axis; 4 - roll, represents the rotational movement about X-axis, 5 - pitch, represents the rotational movement about Y-axis, 6 - yaw, represents the rotational movement about Z-axis. As the floating body shown is symmetric, the movements of roll and pitch, and the movements of surge and sway, are identical.

2.2.2 Equations of motion

According to [25] the motion of a partially submerged oscillating body radiates a broad spectrum of free surface waves. The vertical movement of the floater is given by:

$$m_f \frac{dv_f(t)}{dt} = F_f(t) \tag{2.1}$$

where m_f is the floater mass, $v_f(t)$ is the floater velocity and $F_f(t)$ is the total force applied on the floater. The total force acting on the floater is given by:

$$F_f(t) = F_e(t) + F_p(t) \tag{2.2}$$

where $F_e(t)$ is the wave incident force and $F_p(t)$ represents the PTO force. With:

$$F_p(t) = A_p p_c(t) \tag{2.3}$$

where A_p is the cross section area of the pump piston and p_c is the pump actuator pressure.

In the WEHC, the mechanical damping is related to the mechanical constraint imposed by the pump actuator connected to the floater. The floater motion drives the pump, which injects water into the hyperbaric chamber, exclusively during the descendant motion of the floater. Thereby, during the descendant motion, the pressure inside the pump becomes equal to the chamber pressure, p_c (high-pressure stage). During the ascendant motion, the pressure inside the pump becomes negligible, close to the atmospheric pressure (low-pressure stage) [34]. Figure 2.8 shows a simplified scheme of the PTO system.

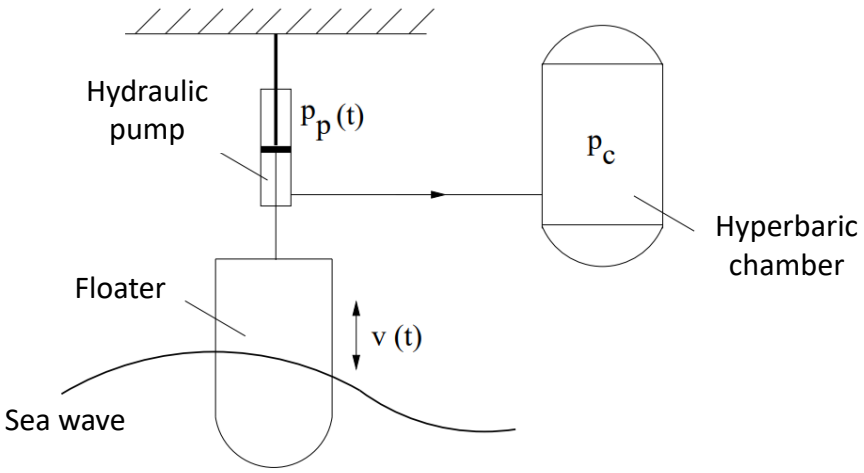

Figure 2.8: Simplified scheme of the PTO system, adapted from [34].

2.2.3 Power absorption

The energy absorbed by the floater, coupled to the lever arm, is used to pump water into the chamber, which is afterwards used to drive a turbine. The average absorbed power, P_a, through a wave period T can be calculate by:

$$P_a = \frac{1}{T}\int_T F_p(t)v_f(t)dt \tag{2.4}$$

Considering that the moment applied by the PTO on the floater-lever arm group is given by:

$$T_{PTO} = F_p b = p_c A_p b \tag{2.5}$$

the pressure applied by the pump actuator in the PTO system can be calculated by:

$$p_c = \frac{T_{PTO}}{A_p b} \tag{2.6}$$

where b is the distance between the pump piston and the lever arm rotation point.

2.2.3.1 Energy conversion efficiency

The WEC's ability to extract power from a wave is characterized by the capture width ratio (CWR), which is defined as the ratio between the absorbed power and the incident wave power:

$$CWR = \frac{P_a}{J} \tag{2.7}$$

where J is the propagated wave power per unit width of a wavefront. From the linear wave theory, the propagation power per unit of a sinusoidal wavefront is given by [35]:

$$J = \frac{\rho g^2}{32\pi} H^2 T \tag{2.8}$$

Therefore, the floater efficiency, E, can be defined as [36]:

$$E = \frac{2\pi}{\lambda} CWR \tag{2.9}$$

which has a maximum value equal to 1 for any wavelength λ.

2.3 Location and wave conditions

The Portuguese coast has privileged conditions for the development and utilization of WECs, consequently this study focuses on studying a WEC that could be installed along Portuguese coast. WindFloat Atlantic, illustrated in Figure 2.9, is operating 20 km offshore Viana do Castelo, Portugal. This installation consists in three giant wind turbines, sited on top of three WindFloat platforms, which are anchored to the seabed 100 m below

with catenary mooring lines. These platforms can be coupled with WECs, resulting in hybrid SSPs.

Figure 2.9: WindFloat Atlantic (Viana do Castelo, Portugal)

Simulations maritime conditions are decided based on literature [37]. The consulted study reports data about maritime agitation along Portuguese coast.

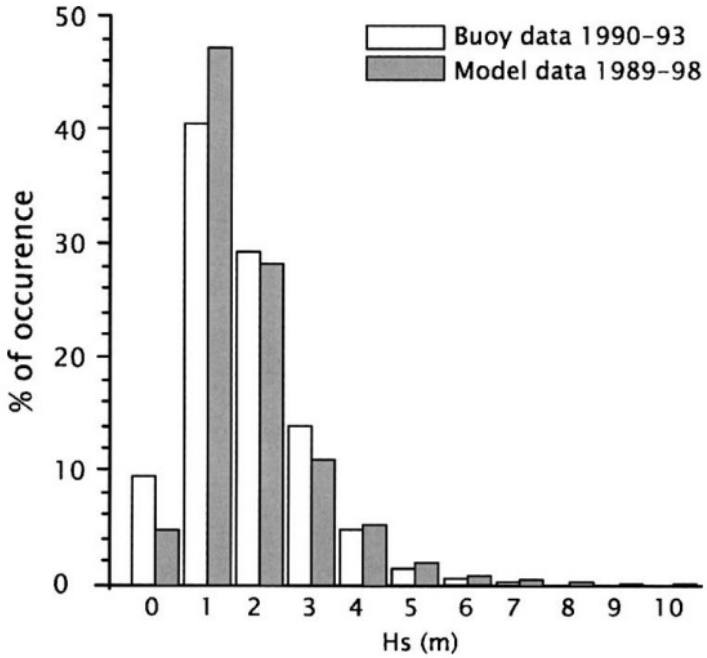

Figure 2.10: Histograms of significant wave height, adapted from [37].

Figure 2.10 and Figure 2.11 show mean parameters of incident waves on Portugal's west coast. From the analysis of these parameters, it is considered that simulations can use

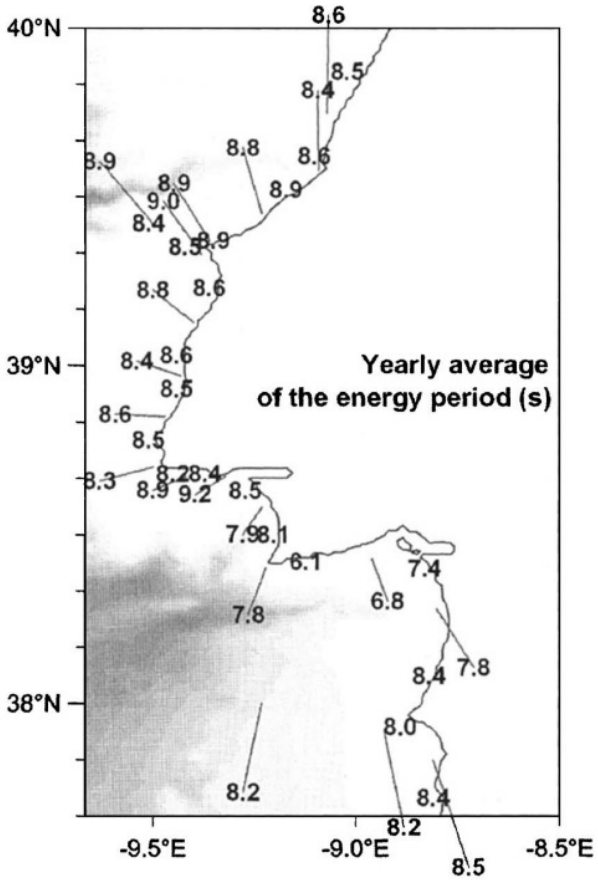

Figure 2.11: Detail of a portion of Portugal's west coast, showing the yearly average incident waves period, adapted from [37].

any wave period ranging between 3 s and 15 s. This is a wide range of periods, although too short or too long periods not being common. Considered wave heights range between 1 m and 2.5 m.

2.4 Numerical approaches for fluid-structure interaction

This section compares two modelling approaches to simulate the interaction between waves and structures. Each method is identified by certain advantages and disadvantages, adoption of which is mainly dependent on the purpose of the simulation and the influential variants affecting the phenomenon [38]. The compared models are based on the Navier-Stokes equations.

Models based on the Navier-Stokes equations are distinguished by how the flow is treated. If the fluids are considered to be continuous in space, models are called Eulerian. Otherwise, if the fluids are considered to be an ensemble of different points or particles, models are called Lagrangian.

2.4.1 Eulerian Navier-Stokes models

RANS models correspond to the first subtype of Navier-Stokes models. These equations consider the flow fields as a continuous phase, for which the Navier–Stokes equations for the flow field are solved based on methods, namely the finite volume method (FVM). Eulerian-based methods are widely known and desired for the simulation of different kind of flows. They have been applied to a wide range of engineering applications and, particularly, for studying different WECs concepts, namely: for the study of point absorbers [39], OWSCs [40] and OWCs [41].

Despite their great success, Eulerian-based methods suffer from some difficulties, in particular for those cases that present discontinuities or whose mesh needs to be modified during run time according to topological changes.

The development of 3D RANS models is allowing to accurately capture 3D wave-structure interaction processes and, when compared to Lagrangian methods, with considerable less computational cost.

2.4.2 Lagrangian Navier-Stokes models

Smooth Particle Hydrodynamics (SPH) is a Lagrangian numerical model developed by Monaghan et al. [42] to solve astrophysical problems. In SPH the flow is considered as a discrete phase of particles for which the equations of flow are to be solved. Even though SPH is not as developed as Eulerian models, it has some noticeable advantages. First of all, SPH is a meshless method, which is advantageous in locations where a moving boundary (free surface flow) or complex geometries exist. The precise computation of the water free surface could be regarded as the main advantage of Lagrangian methods for complex flows. On top of that, as SPH does not depend on a mesh, certain types of numerical errors are eliminated.

Since SPH method was first developed to solve astrophysical problems, it presents a highly compressible behaviour. This behaviour needs to be reduced to accurately simulate incompressible flows [43]. The high diffusivity is, therefore, its main disadvantage. This characteristic induces an artificial loss in the wave height, limiting the size of the simulation domains to avoid numerical wave damping. In addition, in cases with a high number of particles, the computational cost is considerably high, which is detrimental for 3D numerical simulation.

2.4.3 Conclusions

The previous literature review allows to conclude that the RANS equations are currently the most suitable method to simulate cases of wave-structure interaction. This choice is supported by three main reasons: RANS equations can account for domains large enough to be representative of most real structures, with no numerical wave damping; they are

able to simulate complex phenomenons involving WECs; and are capable of simulating real 3D domains with acceptable computational cost.

2.5 RANS modelling

The starting point of the RANS equations is the Reynolds decomposition of the flow variables into mean and fluctuating parts, where the insertion of the Reynolds-decomposed variables into the Navier-Stokes equations, followed by an averaging of the equations themselves, gives rise to the Reynolds-stress tensor, an unknown term that has to be modeled in order for the RANS equations to be solved.

2.5.1 Governing equations

RANS equations were formulated by Osborne Reynolds [44] assuming that an instantaneous quantity ψ could be decomposed into mean $\overline{\psi}$ and fluctuating parts ψ', resulting:

$$\psi = \overline{\psi} + \psi' \tag{2.10}$$

The first equation, the continuity equation, derives from applying the mass conservation law to a control volume, i.e. the change in mass inside the control volume is a result of the mass flux across the boundaries. For a 3D problem:

$$\frac{\partial \rho}{\partial t} + \frac{\partial \rho u_i}{\partial x_i} + \frac{\partial \rho u_j}{\partial x_j} + \frac{\partial \rho u_k}{\partial x_k} = 0 \tag{2.11}$$

where ρ is the fluid density and the velocity vector is defined as $\mathbf{U} = (u_i, u_j, u_k)$.

If the fluid is considered to be incompressible, Equation (2.11) can be simplified because fluid density does not change in time and space. The result, in Einstein notation, is as follows:

$$\frac{\partial u_i}{\partial x_i} = 0 \tag{2.12}$$

Applying the Reynolds decomposition ($\psi = \overline{\psi} + \psi'$) to Equation (2.12) and time-averaging it again yields the same equation, but formulated in terms of time-averaged velocity.

The second equation can be obtained by performing differential analysis to enforce the conservation of momentum law. A general analysis yields Cauchy's equation:

$$\frac{\partial \rho u_i}{\partial t} + \frac{\partial \rho u_i u_j}{x_j} = \rho g_i + \frac{\partial \sigma_{ij}}{\partial x_j} \tag{2.13}$$

where g_i is the acceleration vector due to gravity and σ_{ij} is the stress tensor.

The first step is to separate the stress tensor into the stresses induced by pressure (p) and by viscosity:

$$\sigma_{ij} = -p\delta_{ij} + \tau_{ij} \tag{2.14}$$

where τ_{ij} is the viscous stress tensor.

As the most common fluids are Newtonian, meaning that the viscous stresses, τ_{ij}, are linearly proportional to the strain, ϵ_{ij}, results in:

$$\tau_{ij} = 2\mu\epsilon_{ij} \tag{2.15}$$

where μ is the dynamic viscosity of the fluid. Since ϵ_{ij} is defined as:

$$\epsilon_{ij} = \frac{1}{2}\left(\frac{\partial u_i}{\partial x_j} + \frac{\partial u_j}{\partial x_i}\right) \tag{2.16}$$

the final expression of the stress tensor is:

$$\sigma_{ij} = -p\delta_{ij} + \mu\left(\frac{\partial u_i}{\partial x_j} + \frac{\partial u_j}{\partial x_i}\right) \tag{2.17}$$

The last term of Equation (2.17) can be simplified, under the consideration of incompressible flow, because the antisymmetric part of the deviatoric stress tensor represents the fluid rotation and cannot generate stress by itself [45]. Furthermore, if the viscosity is constant along the fluid, results in:

$$\frac{\partial \rho u_i}{\partial t} + \frac{\partial \rho u_i u_j}{\partial x_j} = -\frac{\partial p\delta_{ij}}{\partial x_j} + \rho g_i + \mu\frac{\partial}{\partial x_j}\frac{\partial u_i}{\partial x_j} \tag{2.18}$$

Applying the Reynolds decomposition is not as straightforward as for the continuity equation, as some cross pairs show up. With reference to the nonlinear term of Equation (2.18), one has:

$$\overline{u_i u_j} = \overline{\left(\overline{u_i} + u_i'\right)\left(\overline{u_j} + u_j'\right)} = \overline{\overline{u_i}\,\overline{u_j}} + \overline{\overline{u_i}u_j'} + \overline{u_i'\overline{u_j}} + \overline{u_i'u_j'} = \overline{u_i}\,\overline{u_j} + \overline{u_i'u_j'} \tag{2.19}$$

With Equation (2.19) the final form of the RANS equations can be obtained. Note that the bars over the time-averaged variable have been dropped:

$$\frac{\partial \rho u_i}{\partial t} + \frac{\partial \rho u_i u_j}{\partial x_j} + \frac{\partial \rho\overline{u_i'u_j'}}{\partial x_j} = -\frac{\partial p}{\partial x_i} + \rho g_i + \mu\frac{\partial}{\partial x_j}\frac{\partial u_i}{\partial x_j} \tag{2.20}$$

The new term, $\rho\overline{u_i'u_j'}$, generates the so called Reynolds stresses and is usually included with the viscous term:

$$\frac{\partial \rho u_i}{\partial t} + u_j\frac{\partial \rho u_i}{\partial x_j} = -\frac{\partial p}{\partial x_i} + \rho g_i + \frac{\partial}{\partial x_j}\left[\mu\frac{\partial u_i}{\partial x_j} - \rho\overline{u_i'u_j'}\right] \tag{2.21}$$

Considering that this term involves the turbulent fluctuations of velocity and only appears when time-averaging the equations, it can be thought of as a contribution from turbulence. Since the RANS equations cannot solve the turbulent fluctuations, this term

has to be modelled, using a turbulence model. As turbulence causes the dissipation of energy, the most usual output of a turbulence model is an additional viscosity:

$$\overline{u_i' u_j'} = -\nu_t \frac{\partial u_i}{\partial x_j} \tag{2.22}$$

The turbulent viscosity is then added to the dynamic viscosity, resulting in an effective viscosity: $\mu_{eff} = \mu + \rho\nu_t = \mu + \mu_t$.

The final RANS equations, taking into account a generic external force F_i, result in:

$$\frac{\partial \rho u_i}{\partial t} + u_j \frac{\partial \rho u_i}{\partial x_j} = -\frac{\partial p}{\partial x_i} + \rho g_i + \frac{\partial}{\partial x_j}\left[\mu_{eff} \frac{\partial u_i}{\partial x_j}\right] + F_i \tag{2.23}$$

The left side of Equation (2.23) represents the change in momentum of the fluid. The first term, the time derivative, takes the unsteadiness into account, while the second term corresponds to the momentum advection by the mean flow. On the right side of Equation (2.23) the pressure gradient appears first, with the body forces (e.g., gravity) appearing after. Next, the stresses account for the viscosity of the fluid and additional turbulent effects. Lastly, any other external forces can be included.

2.6 Wave theories

2.6.1 Linear wave theory

The linear wave theory, also known as the Airy wave theory, was proposed by George Airy in the 19th century and it is considered the simplest way of mathematically representing waves [46]. It can predict with reasonable accuracy the waves behaviour through space and time, however it has a very limited applicability. The main requirement to apply the linear wave theory is that the amplitudes of the waves are small, when compared with the wave length and the water depth. In linear theory the water is assumed to be incompressible, have a constant density and to be inviscid. The flow is irrotational, surface tension is excluded and the Coriolis effect, caused by the earth's rotation, is ignored.

The free surface elevation (η) in z-direction, relative to still water (z=0), as a function of time (t) and of the propagation direction (x-direction), is given by:

$$\eta(x,t) = \frac{H}{2}\cos\left(\frac{2\pi}{\lambda}x - \frac{2\pi}{T}t\right) \tag{2.24}$$

where H is the wave height, T is the wave period and λ is the wave length. The wave length equation, for a certain depth and given period, is given by:

$$\lambda = \frac{gT^2}{2\pi}\tanh\left(\frac{2\pi d}{\lambda}\right) \tag{2.25}$$

where g is the gravitational acceleration and d represents the still water depth. Usually it is more convenient to express the wave in terms of amplitude $a = \frac{H}{2}$, angular frequency $\omega = \frac{2\pi}{T}$ and wave number $k = \frac{2\pi}{\lambda}$ so that the propagating harmonic wave can be written as:

$$\eta(x,t) = a\cos(kx - \omega t) \tag{2.26}$$

Figure 2.12 illustrates some of the waves characteristics indicated above. Another important waves characteristic is the phase speed (c), which is given by:

$$c = \frac{\omega}{k} = \frac{\lambda}{T} \tag{2.27}$$

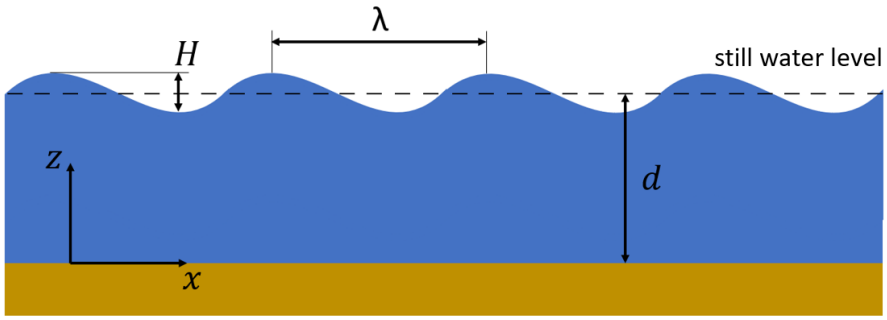

Figure 2.12: Schematic representation of waves characteristics, adapted from [32].

2.6.2 Stokes wave

When waves are too steep or the water is too shallow, linear wave theory can no longer be considered valid. Cnoidal theory should be considered for shallow waters, whereas Stokes wave theory should be considered for steeper waves. Stokes wave theory adds successive corrections to the harmonic wave profile, providing a better approximation of waves.

In Stokes theory, the basic harmonic is written with the wave steepness $\varepsilon = ak$ explicitly represented:

$$\eta(x,t) = a\cos(\omega t - kx) = \varepsilon\eta_1(x,t) \tag{2.28}$$

where $\eta_1(x,t) = k^{-1}\cos(\omega t - kx)$. The first correction in Stokes theory adds a second order term to the linear theory free surface elevation:

$$\eta(x,t) = \varepsilon\eta_1(x,t) + \varepsilon^2\eta_2(x,t) \tag{2.29}$$

which, according to literature [46], results in:

$$\eta(x,t) = a\cos(\omega t - kx) + ka^2\frac{\cosh(kd)}{4\sinh^3(kd)}[2 + \cosh(2kd)]\cos[2(\omega t - kx)] \tag{2.30}$$

where the first term on the right-hand side is the linear wave theory and the second term is the second-order Stokes correction. In practice, the second term can be seen as a wave

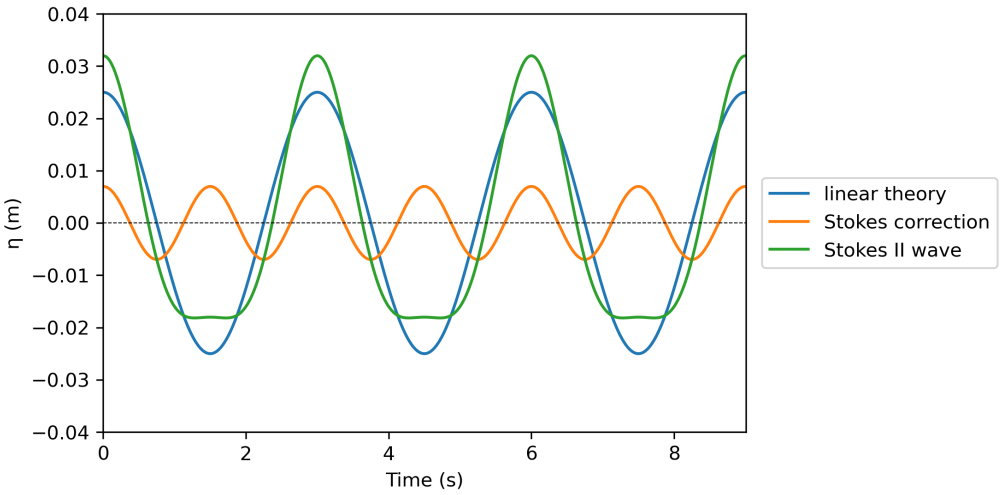

Figure 2.13: Stokes II wave theory: $H = 0.05$ m; $d = 0.4$ m; $T = 3$ s. Python code available in Appendix B.1.

that oscillates twice as fast which, when added to the linear wave, results in a steeper crest and a flatter trough wave, as illustrated in Figure 2.13.

To get higher order corrections, more harmonic waves need to be added. A third-order Stokes correction would result in:

$$\eta(x,t) = \varepsilon\eta_1(x,t) + \varepsilon^2\eta_2(x,t) + \varepsilon^3\eta_3(x,t) \tag{2.31}$$

Figure 2.14 illustrates the diagram developed by Bernard Le Méhauté [47], which relates $\frac{H}{gT^2}$ with $\frac{d}{gT^2}$. This diagram enables a correct choice of the wave theory, according to the study conditions.

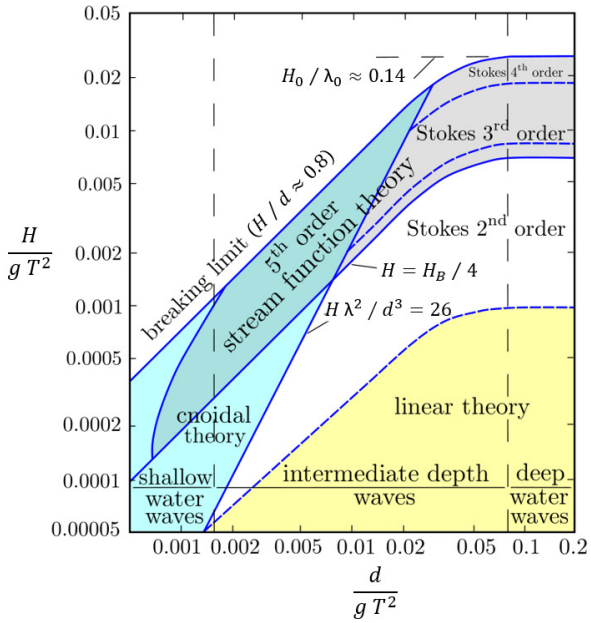

Figure 2.14: Méhauté's diagram [47].

2.6.3 Irregular waves

Oceanic free surface is not regular. Although waves may be individually identified, there is a significant variability both in wave period and height. In order to simulate real conditions, an irregular wave theory is necessary.

Effectively, oceanic free surface consists in the combination of a large number of wave components, with different periods and heights. These components are generated by the sea wind action. Figure 2.15 shows a sum of a large number of harmonic wave components with different periods, directions, amplitudes and phases, resulting in a natural sea state.

An irregular sea state is characterized by: the significant wave height, H_s, defined as the average of the highest one-third of waves that occur in a given period and the peak wave period, T_p, defined as the wave period associated with the most energetic waves in the total wave spectrum at a specific point.

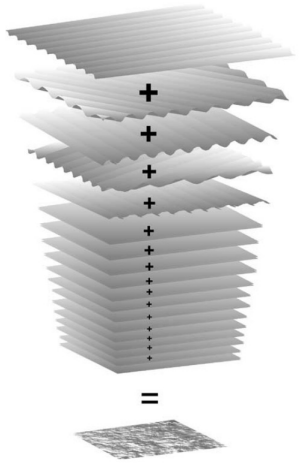

Figure 2.15: Random waves moving in time, i.e., the sum of a large number of harmonic wave components, travelling across the ocean surface with different periods, directions, amplitudes and phases. Adapted from [46].

It is common to model the natural sea state using spectral analysis. Two of the utilised models to define sea states are the Pierson–Moskowitz spectrum and the joint north sea wave project (JONSWAP) spectrum.

The fully developed spectrum, called the Pierson–Moskowitz spectrum, is obtained as [46]:

$$E_{PM}(f) = \alpha_E g^2 (2\pi)^{-4} f^{-5} \exp\left[-\frac{5}{4}\left(\frac{f}{f_{peak}}\right)^{-4}\right] \tag{2.32}$$

where f is the frequency, α_E is the energy scale and f_{peak} is the peak frequency.

Since the Pierson–Moskowitz spectrum is assumed to represent fully developed conditions in deep water, the peak frequency can only depend on the wind speed. By fitting Equation (2.32) to their observations, Pierson and Moskowitz [48] found that $\alpha_E = 0.0081$.

The spectra observed during JONSWAP appear to have a sharper peak than the Pierson–Moskowitz spectrum. To account for this in the parametrisation of the observations,

the shape of the Pierson–Moskowitz spectrum was used by the scientists of JONSWAP and enhanced with a peak-enhancement function, $G(f)$:

$$G(f) = \gamma^{\exp\left[-\frac{1}{2}\left(\frac{\frac{f}{f_{peak}}-1}{\sigma}\right)^2\right]} \tag{2.33}$$

in which γ is a peak-enhancement factor and σ is a peak-width parameter. The peak-enhancement factor and the peak-width parameter value are usually $\gamma = 3.3$ and $\sigma = 0.07$ for $f < f_{peak}$ and $\sigma = 0.09$ for $f > f_{peak}$, respectively. This peak-enhancement function sharpens the spectral peak, but has no effect on other parts of the spectrum.

This idealised spectrum is called the JONSWAP spectrum. It is mostly used for coastal zones and was developed based on data obtained in the north sea. This spectrum is used to generate waves in young sea states, where the waves are generated in zones with limited fetch. Its complete expression is given by [46]:

$$E_{JONSWAP}(f) = \alpha_E g^2 (2\pi)^{-4} f^{-5} \exp\left[-\frac{5}{4}\left(\frac{f}{f_{peak}}\right)^{-4}\right] \gamma^{\exp\left[-\frac{1}{2}\left(\frac{\frac{f}{f_{peak}}-1}{\sigma}\right)^2\right]} \tag{2.34}$$

Figure 2.16 shows the comparison between the Pierson–Moskowitz and JONSWAP spectrum.

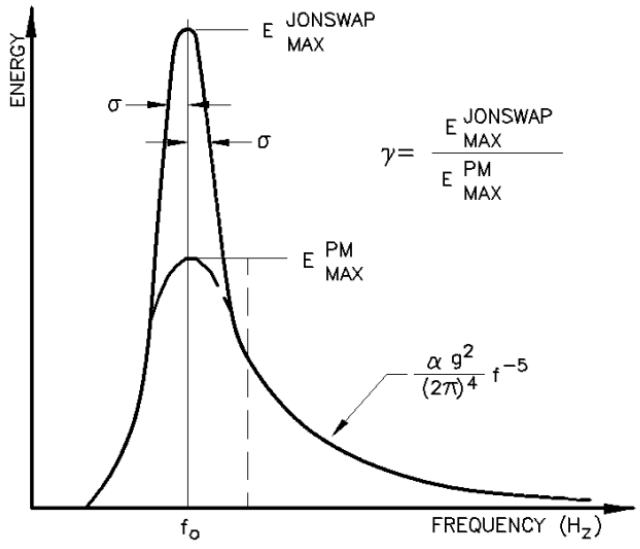

Figure 2.16: Comparison between the Pierson–Moskowitz and JONSWAP spectrum, adapted from [49].

3

Description of the numerical model

Numerical simulations of the WEC are performed using the open-source software OpenFOAM version 9.

3.1 Introduction to OpenFOAM

The free and open-source finite volume CFD toolbox OpenFOAM was originally developed by Henry Weller [50]. It consists in a library of C++ code written in text files and it is primarily used to create executables, known as applications. These applications can be either solvers or utilities. A solver is designed to solve specific problems in fluid or continuum mechanics (e.g., *interFoam*). Utilities feature functionalities to pre and post processing cases, including mesh generation tools (e.g., *blockMesh* and *snappyHexMesh*), mesh decomposition (e.g., *decomposePar*) and tools for setting and modifying field values. The overall structure of OpenFOAM is shown in Figure 3.1.

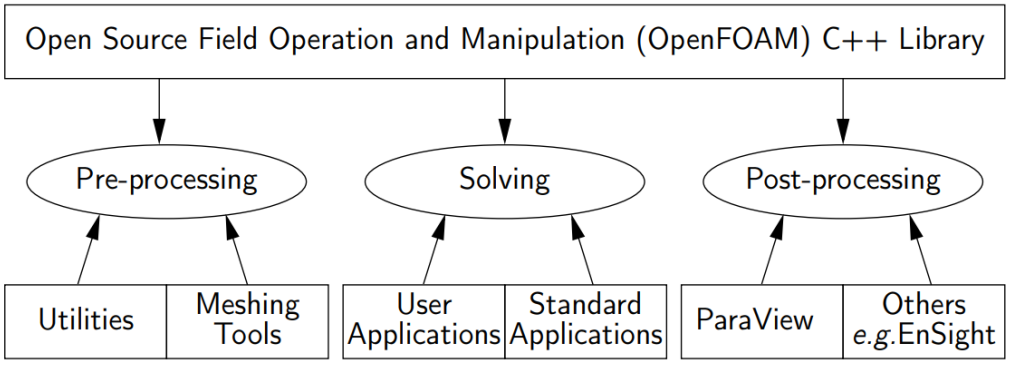

Figure 3.1: Overview of OpenFOAM structure, adapted from [51].

Working with OpenFOAM requires following a specific file structure and organisation. A basic directory structure is shown in Figure 3.2. The *constant* folder contains files which specify the physical properties of the case in study (e.g., *transportProperties* and *turbulenceProperties*) and a subfolder *polyMesh* contains a full description of the case mesh. The *system* folder must contain at least three files: *controlDict* with information of run

control parameters (e.g., start/end time, time step and data output parameters); *fvSchemes* with the discretisation schemes used in the solution; and *fvSolution* contains the equation solvers, tolerances and other algorithm controls. The time directories can be either folders with results written by OpenFOAM during the simulation or a *0* folder with initial values and boundary conditions that must be specified by the user.

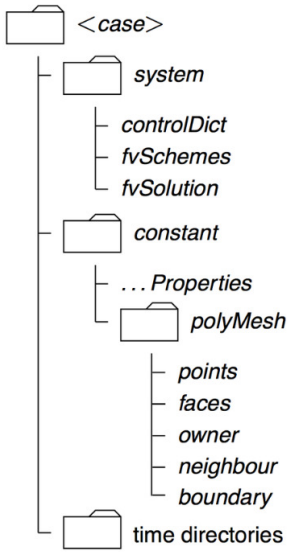

Figure 3.2: Case directory structure, adapted from [52].

OpenFOAM allows running applications in parallel using message passing interface (MPI) and domain decomposition for parallelization. It handles the decomposition of mesh and initial field data using *decomposePar* utility. The case results can be reconstructed for post-processing using *reconstructPar* utility.

Being an open-source software, OpenFOAM's source code can be modified and adapted to the user needs. This is beneficial, as it results in constant development and extension of the available solvers and utilities. Other useful tools allow mesh and data conversion from and to commercial CFD software, such as *Ansys*, *Fluent* or *CFX*.

As OpenFOAM does not have a graphical user interface (GUI), additional software is used for data visualization. The multi-platform data analysis and visualization application ParaView is the most used program for post-processing.

3.2 olaFlow library

The WEC analysis is conducted augmenting OpenFOAM's capabilities with the olaFlow [53] library for wave generation and absorption. OlaFlow is an open-source project conceived as a continuation of the work in Pablo Higuera's thesis [54].

3.2.1 olaDyMFlow solver

The olaDyMFlow solver is based on the standard OpenFOAM's solver *interFoam*. It solves the three-dimensional volume-averaged Reynolds averaged Navier-Stokes equations (VARANS) for two incompressible phases (water and air) using the finite volume discretization and the volume-of-fluid (VOF) technique to represent complex free surface configurations. olaDyMFlow distinguishes from other solvers due to its capabilities on free surface flow through porous media, wave generation and active wave absorption (for static and dynamic meshes) and an enhanced version of dynamic meshing, increasing simulations accuracy of floating structures with six DoFs.

3.2.1.1 RANS

OpenFOAM implements by default the mathematical expressions that link pressure and velocity, known as RANS equations. The form of the momentum equation differs slightly from the regular RANS equations seen in Section 2.5.1, while the continuity equation remains identical. Under the assumption of incompressible fluids, the continuity and momentum conservation equations, adapted to OpenFOAM formulation and in Einstein notation are, respectively, given by:

$$\frac{\partial u_i}{\partial x_i} = 0 \tag{3.1}$$

$$\frac{\partial \rho u_i}{\partial t} + u_j \frac{\partial \rho u_i}{\partial x_j} = -\frac{\partial p^*}{\partial x_i} - g_j X_j \frac{\partial \rho}{\partial x_i} + \frac{\partial}{\partial x_j}\left[\mu_{eff} \frac{\partial u_i}{\partial x_j}\right] + F_i^{ST} \tag{3.2}$$

where u is the velocity component, x is the position component, p^* is the pseudo-dynamic pressure, X is the position vector and F_i^{ST} is the surface tension force. More details about the deduction of these equations can be found on literature [54].

3.2.1.2 VARANS

The VARANS equations are the ones implemented in olaDyMFlow. The equation for conservation of mass is the same as before, but for volume averaged velocity, given by:

$$\frac{\partial \langle u_i \rangle}{\partial x_i} = 0 \tag{3.3}$$

The momentum conservation equation is given by:

$$\begin{aligned} \frac{1+C}{\phi}\frac{\partial \rho \langle u_i \rangle}{\partial t} + \frac{1}{\phi}\frac{\partial}{\partial x_j}\left[\frac{1}{\phi}\rho \langle u_i \rangle \left\langle u_j \right\rangle\right] = \\ -\frac{\partial \left\langle p^* \right\rangle^f}{\partial x_i} - g_j X_j \frac{\partial \rho}{\partial x_i} + \frac{1}{\phi}\frac{\partial}{\partial x_j}\left[\mu_{eff}\frac{\partial \langle u_i \rangle}{\partial x_j}\right] + F_i^{ST} \\ -\alpha_t \frac{(1-\phi)^3}{\phi^3}\frac{\mu}{D_{50}^2}\langle u_i \rangle - \beta_t \left(1 + \frac{7.5}{KC}\right)\frac{1-\phi}{\phi^3}\frac{\rho}{D_{50}}\sqrt{\left\langle u_j \right\rangle \left\langle u_j \right\rangle}\langle u_i \rangle \end{aligned} \tag{3.4}$$

where ϕ is the porosity, D_{50} is the mean nominal diameter, C, α_t, β_t are tuning factors and KC is the Keulegan–Carpenter number. More details about the deduction of these equations can be found on literature [54].

3.2.1.3 Free surface modelling

In OpenFOAM the free surface is captured using the VOF method [55]. In this method an additional transport equation must be taken into account to describe the movement of the water-air interface.

This equation is based on the *phase fraction*, denoted by α in OpenFOAM, which indicates the quantity of water per unit of volume in each cell. In particular, $\alpha = 1$ corresponds to a cell full of water and $\alpha = 0$ to a cell full of air. Cells with α values ranging between 0 and 1 belong to the free surface, as illustrated in Figure 3.3. Free surface flows should, ideally, have a discontinuous transition between the fluid phases. In order to guarantee that this transition is modelled as accurately as possible, using the VOF model, the region of the computational domain where the free surface is likely to appear should have a higher cell density.

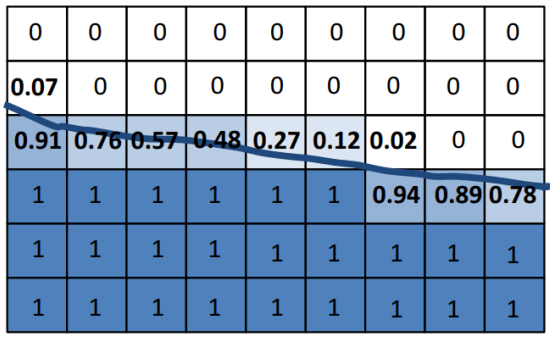

Figure 3.3: VOF method to capture the free surface interface, adapted from [56]. The line represents the actual free surface and the numbers represent the volume fraction in each cell.

Fluid properties for each cell can be calculated just by weighting the volume fraction. The density of the fluid in a cell is calculated as follows:

$$\rho = \alpha \rho_{water} + (1 - \alpha)\rho_{air} \tag{3.5}$$

In the VOF for two fluids, the transport equation for the phase fraction is given by:

$$\frac{\partial \alpha}{\partial t} + \nabla \cdot \mathbf{U}\alpha = 0 \tag{3.6}$$

Equation (3.6) can be a starting point for the expression that tracks the movement of the free surface, however, in order to obtain physical results, some corrections and considerations need to be applied. To obtain a sharp interface, OpenFOAM introduces an extra term called *artificial compression* ($\nabla \cdot \mathbf{U}_c(1 - \alpha)\alpha$) to the transport equation. Based

on the expression, the *artificial compression* only has influence on regions where the phase fraction is different from 0 and 1. The transport equation then becomes:

$$\frac{\partial \alpha}{\partial t} + \nabla \cdot \mathbf{U}\alpha + \nabla \cdot \mathbf{U}_c(1-\alpha)\alpha = 0 \tag{3.7}$$

where $\mathbf{U}_c$ is a velocity vector normal to the interface that applies the artificial compression on the interface. The compression velocity is given by $\mid \mathbf{U}_c \mid = min[c_\alpha \mid \mathbf{U} \mid, max(\mid \mathbf{U} \mid)]$, where c_α can be specified by the user. In OpenFOAM, c_α is given by cAlpha. A zero value for cAlpha eliminates the interface compression whereas higher values increase the compression of the interface.

Equation (3.7) is implemented by default in OpenFOAM. The equation implemented in olaDyMFlow solver is given by:

$$\frac{\partial \alpha}{\partial t} + \frac{1}{\phi}\frac{\partial \alpha \langle u_i \rangle}{\partial x_i} + \frac{1}{\phi}\frac{\partial \alpha (1-\alpha) \langle u_i \rangle}{\partial x_i} = 0 \tag{3.8}$$

Another important aspect is that α is bounded between 0 and 1. This boundedness is achieved by using the Multidimensional Universal Limiter for Explicit Solution (MULES) solver.

3.2.2 Modelling of waves in OpenFOAM

Currently there are several options for wave generation and absorption in OpenFOAM. The first and oldest procedure is *GroovyBC* [57], which can be used to set non-uniform boundary-conditions without programming. It accepts basic mathematical expressions and is suitable to generate simple wave theories such as Stokes I and II, but no wave absorption procedure is available. Also, this technique will lead to an increase in water level during runtime, due to an imbalance between wave crests and troughs.

Another option, *waves2Foam* [58], was specifically developed for wave generation, hence, it supports a large range of wave theories. It also has wave absorption capabilities, but applies them through internal relaxation zones. Although being one of the most used techniques for wave generation and absorption in OpenFOAM, it has the clear disadvantage of increased computational effort, with solving time increasing up to 50% [54].

olaFlow's toolbox has several features for active wave generation and absorption at the boundaries. It also supports a wide range of wave theories and has the advantage of not needing to increase the computational domain for wave absorption, leading to the decrease of computational effort and solving time.

3.2.2.1 Static boundary wave generation

olaDyMFlow wave generation boundary condition (BC) [59] has active wave absorption, allowing incident waves to flow out while still generating the target waves. It can replicate laboratory wave makers. Waves can be generated at the boundary according to different

wave theories, such as: Stokes I, II and V, cnoidal, streamfunction regular waves and Boussinesq solitary wave.

Wave conditions need to be specified by the user in a dictionary file, *waveDict* by default, located in the *constant* folder. Some of the specified properties are the wave type, wave theory, wave height and wave period. All options available are illustrated in Figure 3.4.

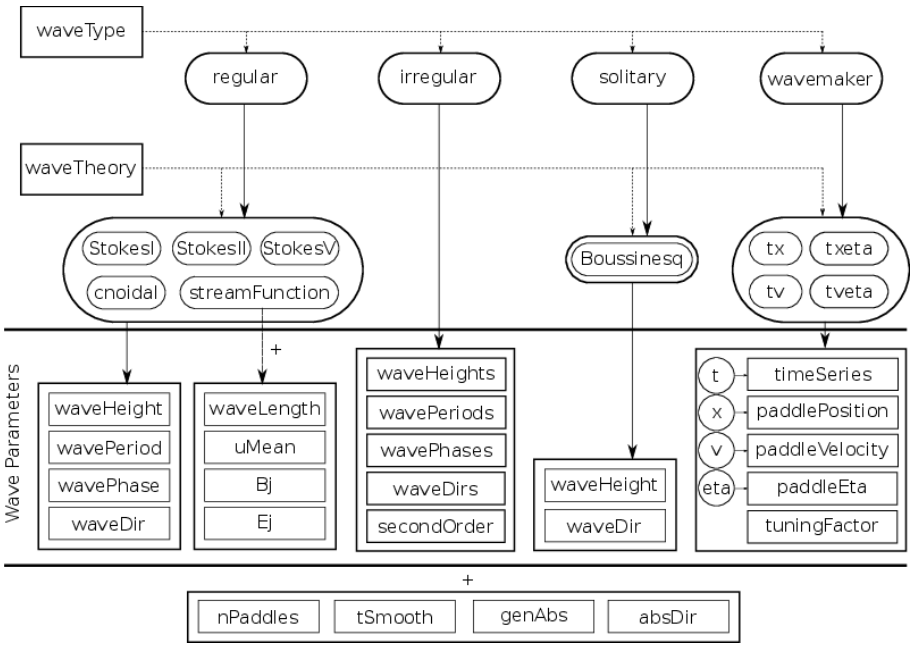

Figure 3.4: Wave generation options, adapted from [59].

3.2.2.2 Static boundary active wave absorption

Active wave absorption systems can be divided into three categories: 2D, Quasi-3D and 3D. In this thesis the Quasi-3D system is used, which is only a correction of the 2D absorption theory.

3.2.2.3 2D Absorption

To cancel out reflected waves the boundary must generate a velocity equal to the incident one, but in opposite direction. According to [54] the expression for active wave absorption is:

$$U_c = -\sqrt{\frac{g}{d}}\eta_R \tag{3.9}$$

where U_c is the correction velocity that is applied to a vector perpendicular to the boundary, pointing into the domain. The reflected wave height (η_R) is calculated by subtracting the measured elevation at the wave maker (η_M) from the target one (η_T), according to the expected reflection-free wave generation: $\eta_R = \eta_M - \eta_T$

This theory was first developed for two dimensional cases, on wave flumes, but can easily be extended to three dimensions. However, there is some drawbacks when absorbing in 3D with 2D theory, as only the wave component perpendicular to the boundary can be absorbed. The other components will continue to propagate until they reach a dissipating device.

3.2.2.4 Quasi-3D Absorption

Absorbing oblique waves can be achieved by applying a correction to the previously presented 2D absorption theory, improved by accounting for a known angle of incidence (β). According to [54], the practical application is to reduce velocity by a factor of $\cos(\Delta\beta)$, as presented in Equation (3.10).

$$U_c = -\cos(\Delta\beta)\sqrt{\frac{g}{d}}\eta_R \tag{3.10}$$

To obtain a better performance, the method applied in olaFlow was modified. Instead of reducing the correction velocity and applying it to the direction perpendicular to the boundary, the total correction velocity is still the one calculated with Equation (3.9), but applied to the desired direction. This improves the boundary performance but, some problems may persist as most of the times the direction of the incident waves cannot be anticipated, or radiation from the structure causes that direction to change either in time or along the boundary extents.

3.3 FVM

According to literature [60], the FVM is a discretization method which is well suited for the numerical simulations of various types of conservation laws, and it has been extensively used in a wide range of engineering fields, such as fluid mechanics, heat and mass transfer or petroleum engineering. FVM has some important features, which are similar to those of finite element method (FEM), such as the use on arbitrary geometries, application to structured or unstructured meshes and it leads to robust schemes. In addition, it enables the local conservativity of the numerical fluxes, i.e. the numerical flux is conserved from one discretization call to its neighbour. This particular capacity makes the FVM quite useful for the fluid mechanics field. FVM is based on a balance approach, making it locally conservative. This balance is written for each control volume, and then, using the divergence theorem an integral formulation of the fluxes over the boundary of the control volume is obtained.

This method can be either cell-centered or vertex-centered, as shown in Figure 3.5. In the cell-centered case variables' values are stored at the cell center, whereas in the vertex-centered case values are stored at the vertices. The method used along this thesis was the cell-centered FVM. The formulation can be consulted in literature [61].

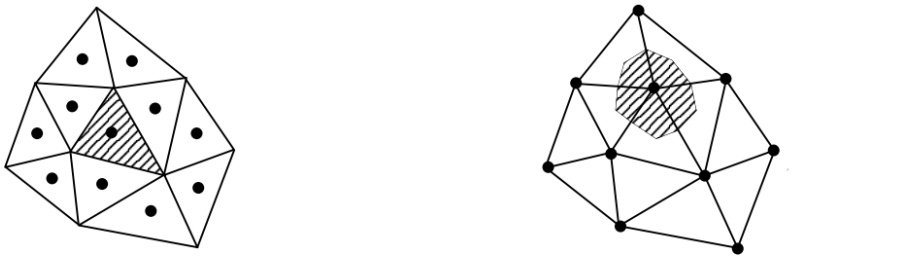

(a) Control volumes of the cell-centered FVM (b) Control volumes of the vertex-centered FVM

Figure 3.5: Meshes and control volumes associated to cell-centered and vertex-centered FVMs, adapted from [62].

3.4 Mesh generation

The quality of numerical simulations directly depends on the mesh, as CFD codes are more efficient and robust when solving structured grids. To avoid an increase in computational cost, the mesh should be generated considering the variation of flow variables, such as velocity and pressure.

Stéphane Rapuc et al. [63] proposes guidelines for wave-energy based topology, with unstructured grids, where the refinement zones are separated in three different horizontal refinement boxes. The first one, zone A, is refined from the wave crest to the wave trough with a refinement based on a number of cells per wave height, to capture the free surface. The second, zone B, is refined from the wave crest to -20% of the wave length to capture 90% of the wave kinetic energy. Finally, zone C, is refined from -20% of the wave length to -60% of the wave length in order to catch the last 9.9% of the wave kinetic energy.

Figure 3.6 shows the refinement boxes. These boxes extend across the domain, from the *inlet BC* to *outlet BC*. Refinement of each adjacent box decreases as wave energy decreases. To keep the discontinuous transition between the fluid phases, as seen in Section 3.2.1.3, zone A has the highest cell density in the vertical direction.

In this thesis the same grid topology principle is adopted, but adapted to cartesian structured grids. The computational domain mesh was generated with *Workbench*, using the *CutCell* method and the *body of influence* tool to refine the free surface zone. Figure 3.7 shows an example of the mesh used in this thesis, where the refinement boxes can be seen.

3.5 Boundary conditions

In order to correctly simulate the behaviour of waves in numerical modelling, appropriate boundary conditions must be applied. A numerical wave tank (NWT) has six boundaries which are the *inlet*, *outlet*, *bottom*, *atmosphere*, *front* and *back*. In this study the *bottom*, *front* and *back* boundaries were aggregated in a single boundary, named *stationaryWalls*.

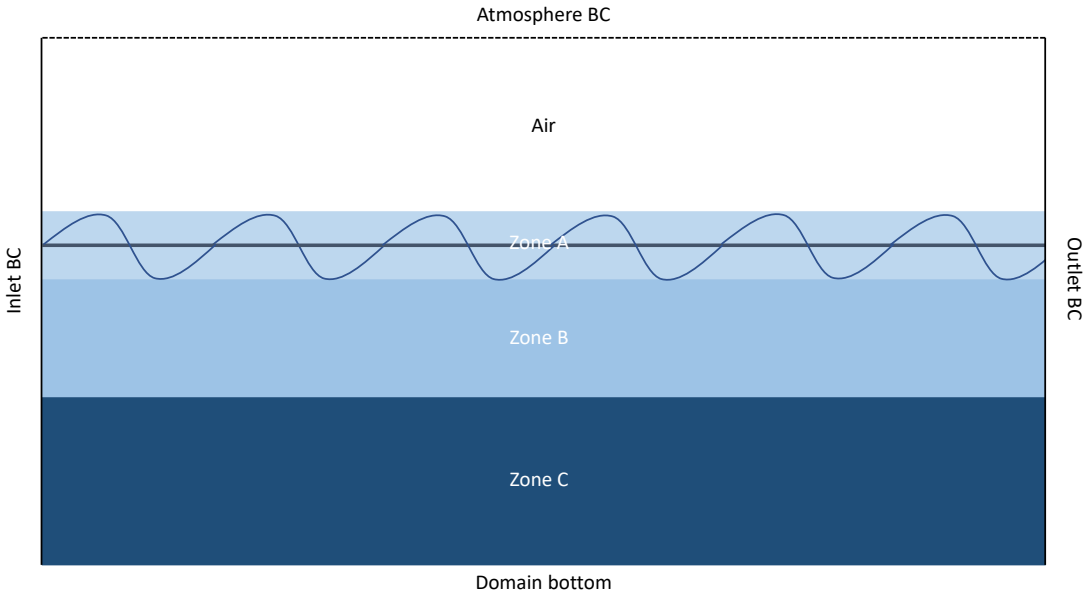

Figure 3.6: Schematic of the mesh refinement boxes described in [63].

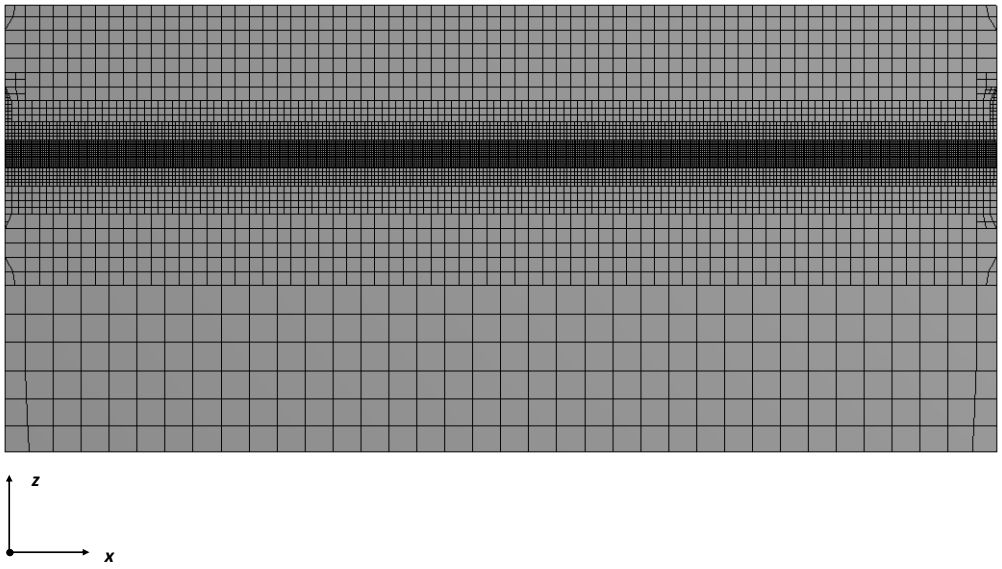

Figure 3.7: Example of the mesh used in this thesis.

Also, as there is a WEC in study an additional boundary condition is necessary, which is named *floatingObject*. The boundary conditions used in this thesis are briefly described bellow, according to the definition in [64]:

- *zeroGradient* applies a zero-gradient condition from the patch internal field onto the patch faces;
- *inletOutlet* provides a generic outflow condition, with specified inflow for the case of return flow;

- *fixedFluxPressure* sets the pressure gradient to the provided value such that the flux on the boundary is that specified by the velocity boundary condition;
- *totalPressure* provides a total pressure condition;
- *fixedValue* supplies a fixed value constraint;
- *calculated* is not designed to be evaluated, it is assumed that the value is assigned via field assignment;
- *noSlip* fixes the velocity to zero at walls;
- *pressureInletOutletVelocity* is applied to pressure boundaries where the pressure is specified. A zero-gradient condition is applied for outflow. For inflow, the velocity is obtained from the patch-face normal component of the internal-cell value;
- *movingWallVelocity* provides a velocity condition for cases with moving walls;

Besides these BCs, others are used. *waveAlpha* is designed for the VOF-fraction in a multiphase solver and used for wave boundary conditions. *waveVelocity* is used for the velocity field in a multiphase solver and also used for wave boundary conditions. Both of these belong to the *waves2foam* toolbox. *waveAbsorption2DVelocity* is a wave absorption BC which works in both 2D and 3D and belongs to olaFlow's toolbox.

The BCs need to be set in the according files, inside the *0* folder. Table 3.1 provides an overview of all BCs used.

Table 3.1: Overview of used boundary conditions: waveAlpha (wA), zeroGradient (zG), inletOutlet (iO), fixedFluxPressure (fFP), totalPressure (tP), fixedValue (fV), calculated (c), waveVelocity (wV), waveAbsorption2DVelocity (wA2DV), noSlip (nS), pressureInletOutletVelocity (pIOV), movingWallVelocity (mWV).

boundary	inlet	outlet	stationaryWalls	atmosphere	floatingObject
alpha.water	wA	zG	zG	iO	zG
p_{rgh}	fFP	fFP	fFP	tP	fFP
pointDispalcement	fV	fV	fV	fV	c
U	wV	wA2DV	nS	pIOV	mWV

3.6 Motion of the WEC

The motion of the WEC is treated by OpenFOAM as a FSI problem. The process used to solve this FSI problem is illustrated in Figure 3.8. Initially, the Navier-Stokes equations are solved for the fluid pressure and velocity throughout the domain, then the fluid pressure is integrated over the wetted body's surface to calculate the hydrodynamic force on the body. Finally, the body's motion, due to the hydrodynamic force, is calculated using Newton's law.

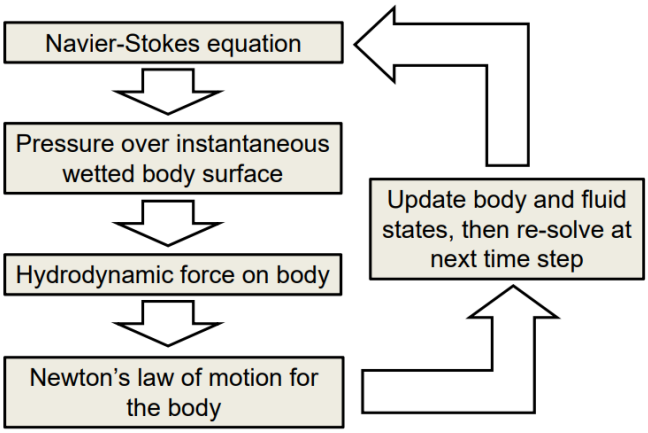

Figure 3.8: Schematic of CFD process for FSI resolution, adapted from [56].

3.6.1 Deformation of the mesh

The case in this thesis depends on the motion of the WEC in study, consequently mesh deformation needs to be available.

Deformation and morphing of the mesh is controlled by the *dynamicMeshDict*, available in Appendix C.1. Mesh motion was applied with the *dynamicMotionSolverFvMesh* motion solver, however this dictionary allows the specification of other types of mesh motion.

Using this mesh motion solver the topology of the mesh does not change. The solver only morphs the mesh around a specified set of boundaries, with the mesh motion being calculated based on the pressure on those boundaries. There are many options and parameters available in this dictionary, namely: morphing control, solver control, body definition, force and motion definitions. These parameters can be consulted at [65].

3.6.2 Modelling of the PTO system

The moment applied on the PTO system can be modelled through an angular damping coefficient, C_{PTO}, and an angular spring coefficient, K_{PTO}:

$$T_{PTO} = K_{PTO} \cdot \theta + C_{PTO} \cdot \dot{\theta} \tag{3.11}$$

where θ is the rotation angle of the floater and $\dot{\theta}$ is its angular velocity.

The simplest model for a PTO system is the linear damper, where $K_{PTO} = 0$. Resulting in:

$$T_{PTO} = C_{PTO} \cdot \dot{\theta} \tag{3.12}$$

As shown in Figure 4.6 the geometry of the WEHC used in the simulations was simplified only to the floater. Consequently, the PTO is simulated as a direct mechanical driven system. The PTO force can be calculated as:

$$F_p = c_{PTO} \cdot v_f \tag{3.13}$$

where c_{PTO} is the PTO's linear damping coefficient.

In OpenFOAM the PTO force can be simulated through an entry in the *restraints* sub-dictionary of the *dynamicMeshDict*. In this thesis, to simulate the PTO system, the *linearDamper* parameter was set. It provides a reactionary force that is proportional to the body velocity, only reacting to linear motions. The damping force is always applied in the opposite direction of the body's linear velocity vector.

The power absorbed by the WEHC can calculated by:

$$P = \left| F_p \cdot v_f \right| \tag{3.14}$$

Also defined in the *restraints* sub-dictionary is the *sphericalAngularDamper* parameter but, in this case, to restrain the WEC's rotational motion. It provides a reactionary moment that is proportional to the body angular velocity, only reacting to angular motions.

3.7 Solving procedure

The pressure-velocity equations are solved by a two step method called PIMPLE, suitable for transient simulations. PIMPLE merges the controls of pressure-implicit with splitting of operators (PISO) and semi-implicit method for pressure-linked equations (SIMPLE). Its main structure is inherited from PISO, but it allows under-relaxation, as in SIMPLE, to ensure the convergence of all equations at each time step. The main difference to PISO is that PIMPLE enables looping through the entire system of equations within one time step, which represents the total number of times the system is solved. When convergence is reached, the solver moves on to the next time step. PIMPLE solves a pressure equation, enforcing mass conservation, with an explicit correction in velocity to satisfy the momentum conservation.

The VOF function sub-cycle is solved with an independent method called MULES. This solver uses a limiter factor on the fluxes of the discretized divergence term to ensure a final value of α between 0 and 1 [54].

To apply this methods some variable need to be defined in the source code (e.g. *nAlphaSubCycles*, *nCorrectors*, *nOuterCorrectors*), more specifically in the *system* directory. This definition influences the performance of the model's solving procedures. The full procedure for solving each time step can be seen in Figure 3.9.

3.8 Simulation parameters

3.8.1 Numerical schemes

Numerical schemes are used to calculate the values of different terms like derivatives, gradients, divergence and interpolations. They are set in the *fvSchemes* file, inside the

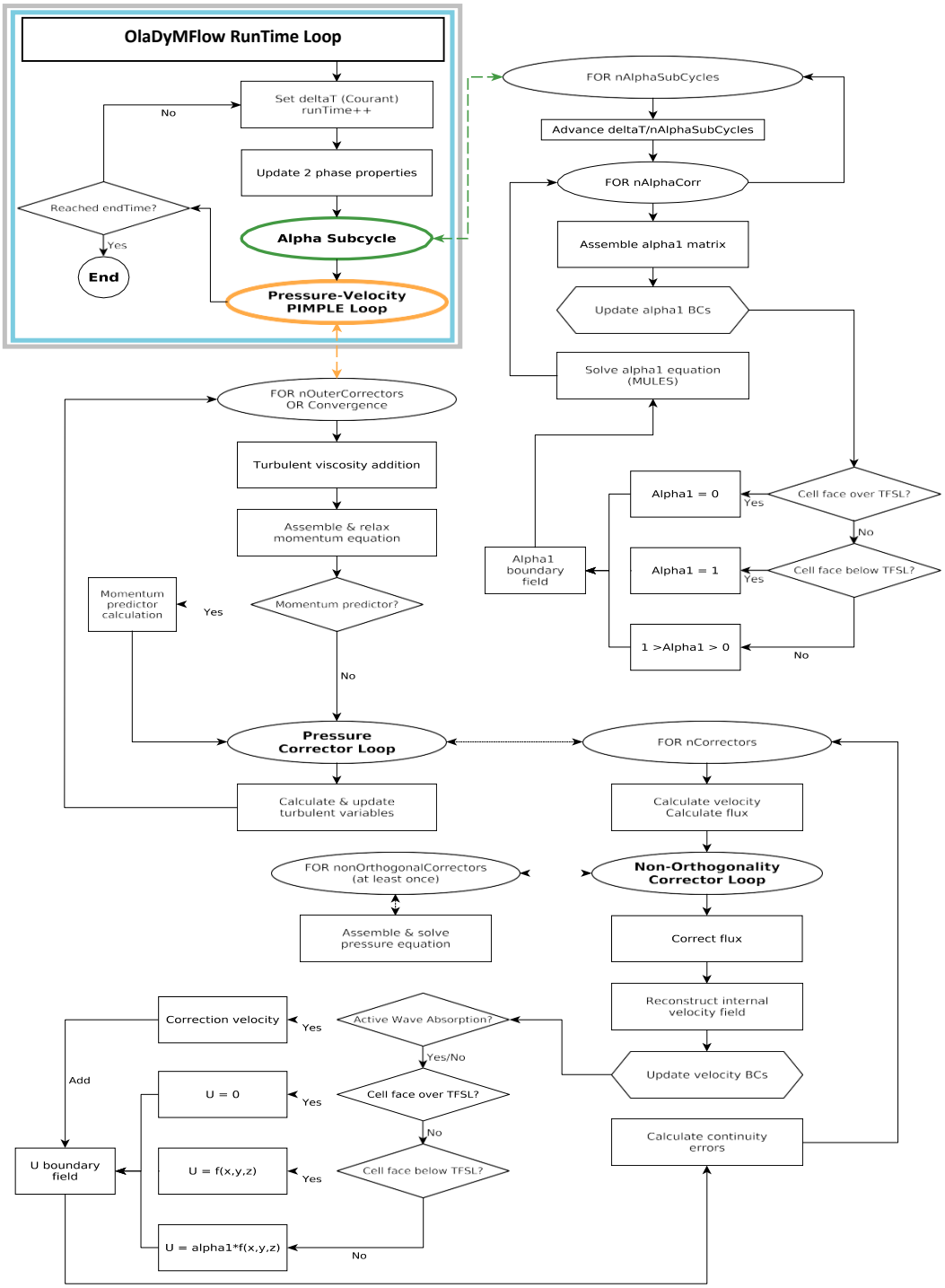

Figure 3.9: olaDyMFlow solving flow chart, adapted from [54].

system folder. Appendix C.2 shows the used parameters in this thesis.

3.8.1.1 Time schemes

To solve first time derivative terms was used the *CrankNicholson* ψ scheme, with $\psi = 0.5$. A ψ value of 1 corresponds to pure *CrankNicholson* whereas $\psi = 0$ corresponds to pure *Euler*. The scheme is of second order, bounded, implicit and defined as follows:

$$\frac{\partial}{\partial t}(\phi_a) = \frac{\phi_a - \phi_a^{00}}{2\Delta t} \tag{3.15}$$

where ϕ_a represents any variable and ϕ_a^{00} represents the variable's values at previous time steps.

3.8.1.2 Gradient schemes

Gradients were solved using the *Gauss linear* scheme. The *Gauss* entry implies the use of the standard finite volume discretization of Gaussian integration. This scheme requires the interpolation of values from cell centres to face centres, with the interpolation scheme being given by *linear*, meaning linear interpolation. The gradient is calculated using Gauss's theorem, given by [61]:

$$\int_{CV} (\nabla \cdot \mathbf{a}) dV = \int_A \mathbf{n} \cdot \mathbf{a} dA \tag{3.16}$$

where the integral of the divergence of a vector **a** over a volume is equal to the component of **a** in the direction normal to the surface which bounds the volume integrated over the entire bounding surface A.

3.8.1.3 Divergence schemes

The ∇ terms are solved using the *Gauss* scheme, which is the only form of discretization available in OpenFOAM. This scheme also requires a selection of an interpolation scheme, which varied according to the different terms.

Chosen schemes are: *Gauss linear*, second order and unbounded, *Gauss upwind*, first order and bounded, *Gauss vanLeer*, second order and unbounded, *Gauss vanLeerV*, an improved version of *vanLeer* to take into account the direction of the field, and *Gauss limitedLinearV 1*, which also takes into account de field direction.

3.8.1.4 Laplacian schemes

The ∇^2 terms are solved using the *Gauss* scheme. This scheme requires a selection of both an interpolation scheme for the diffusion coefficient and a surface normal gradient scheme. *Gauss linear corrected* is the resulting Laplacian scheme chosen, with values being interpolated from cell centres to face centres.

3.8.2 Solver settings

The equations solvers, tolerances and algorithms need to be specified in the *fvSolution* file, inside the *system* folder. This file contains specific sub-dictionaries necessary to run the solver. Used parameters in this thesis can be consulted in Appendix C.3.

The *solvers* sub-dictionary specifies the solver that is used for each discretised equation. The used solvers are *smoothSolver* (solver using a smoother), preconditioned conjugate gradient (PCG) and generalised geometric-algebraic multi-grid (GAMG). Parameters like *smoother*, *relTol*, *tolerance* and *preconditioner* are set for each solver.

SmoothSolver was used for *alpha.water*, *U* and U_{Final}. The used *smoothers* were *symGaussSeidel* and *GaussSeidel*, both appropriate for symmetric or asymmetric matrices.

PCG was used for *pcorr* and $p_{rghFinal}$. *DICGaussSeidel* and *GAMG* were the *smoother* and *preconditioner*, respectively, used.

For p_{rgh} the used solver was GAMG. It is appropriate for symmetric or asymmetric matrices and has an efficient transport of information across the solution domain. GAMG solver first generates a quick solution on a mesh with a smaller number of elements and then, using this solution as an initial guess, maps it onto a finer mesh. In practice, this method starts by using the mesh provided by the user and coarsens/refines the mesh in stages. This method is faster than other available in OpenFOAM. The used *smoother* was diagonal incomplete-Cholesky (DIC), appropriate for symmetric matrices.

Equations solvers are iterative and so, are based on reducing the equation residual over a succession of solutions. The residual is a measure of the error in the solution so, the smaller it is, the more accurate the solution is. Specifically, the residual is evaluated by substituting the current solution into the equation and taking the magnitude of the difference between the left and right hand sides.

First, the initial residual is evaluated based on the current values of the field. Residual is then re-evaluated after each solver iteration. The solver will iterate until one of these conditions occur:

- residuals fall bellow the solver tolerance, *tolerance*;
- the ratio between the current and the initial residual falls below the solver relative tolerance, *relTol*;
- the number of maximum iterations is reached, *maxIter*.

For transient problems, the case of this thesis, *relTol* is usually set to 0. This will force the solution to converge to the solver tolerance in each time step.

In the PIMPLE sub-dictionary the number of *nOuterCorrectors*, *nCorrectors* and *nNonOrthogonalCorrectors* are specified.

The third sub-dictionary, *relaxationFactors*, controls under-relaxation, a technique used for improving stability of a computation. Under-relaxation works by limiting the amount of which a variable changes from one iteration to the next.

3.8.3 Run control parameters

Run control parameters are set in the *controlDict* file, inside the *system* folder. Parameters like *startTime*, *endTime*, *writeInterval* and *deltaT* (time step) are set in this file. In this thesis, an adjustable time step was used, being modified according to the max Courant number set. The Courant number, C_o, is the fraction of the cell that the fluid moves across in a time step and has a big influence in the stability of a simulation. Max Courant number varies for different application but, most often, it should be kept bellow 1. It is defined as follows:

$$C_o = \frac{u \cdot \Delta t}{\Delta x} \tag{3.17}$$

ControlDict file also includes used *functions* like *forces* and *interfaceHeight*. This functions generate forces and moments applied on a body and the height of the free surface above a set of locations, respectively.

4

Validation of the numerical model

Convergence studies are conducted using, at least, three multiple solutions. One parameter (e.g., element size) is systematically refined while all other parameters are kept constant. According to literature [66], changes between medium-fine $\varepsilon_{i,21} = \hat{S}_{i,2} - \hat{S}_{i,1}$ and coarse-medium $\varepsilon_{i,32} = \hat{S}_{i,3} - \hat{S}_{i,2}$ are used to define the convergence ratio:

$$R_i = \frac{\varepsilon_{i,21}}{\varepsilon_{i,32}} \tag{4.1}$$

and to determine the convergence condition where $\hat{S}_{i,1}$, $\hat{S}_{i,2}$, $\hat{S}_{i,3}$ correspond to solutions with fine, medium and coarse input parameters, respectively. From the convergence ratio, R_i, three different convergence conditions are possible:

- Monotonic convergence: $0 < R_i < 1$
- Oscillatory convergence: $R_i < 0$
- Divergence: $R_i > 1$

The first step on the validation of the numerical model consists in the validation of wave generation and propagation, using only an empty NWT. The validation is carried out using a mesh convergence study, where wave parameters of simulated regular waves are compared with analytical second order Stokes waves. After, the WEC is introduced in the numerical domain and its motion, as a response to waves, is studied in detail.

4.1 Validation of wave generation and propagation

The wave generation and propagation validation study is executed in an empty NWT, using the guidelines provided in Section 3.4. The chosen NWT is 100 m long, has 40 m of depth and 45 m of height (30 m of water plus 15 m to accommodate the air phase). Figure 4.1 illustrates the NWT geometry.

For the validation study, wave parameters of simulated regular waves are compared with analytical second order Stokes waves. Tested wave conditions are summarized in Table 4.1.

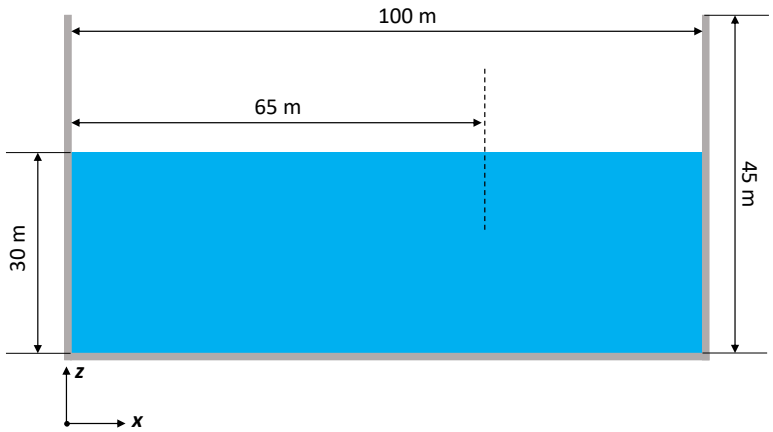

Figure 4.1: NWT geometry, plane $y = 0$.

Table 4.1: Second order Stokes wave conditions considered for the wave generation and propagation validation study.

d (m)	T (s)	H (m)	λ (m)
30	7.5	2.5	85.69

Tests are carried out for seven meshes, with different refinements (i.e. different number of cells/H) used to obtain the free surface elevation (η), designated as A, B, C, D, E, F and G, as shown in Table 4.2. Results are evaluated in the form of a plot of the free surface elevation over the simulation time at $x = 65$ meters (from the wave maker), where later the WEC will be positioned. Results are compared with an analytical free surface elevation of a second order Stokes wave. From the analysis of Figure 4.2 no conclusions can be taken about which mesh is fine enough, as there is no clear convergence behaviour on the wave quality.

Table 4.2: Number of cells/H for the different meshes.

mesh	A	B	C	D	E	F	G
cells/H	4	6	8	10	12	14	20

In order to draw considerable conclusions the agreement between numerical and analytical results is quantified considering two statistical parameters: normalized amplitude error, A_χ, and normalized phase error, φ_χ, respectively given by:

$$A_\chi = \sqrt{\frac{\sum_{i=1}^{N}\left(\chi_i^{num}\right)^2}{\sum_{i=1}^{N}\left(\chi_i^{exp}\right)^2}} \tag{4.2}$$

and

$$\varphi_\chi = \sqrt{\frac{\sum_{i=1}^{N}\left(\chi_i^{num}-\chi_i^{exp}\right)^2}{\sum_{i=1}^{N}\left(\chi_i^{exp}\right)^2}} \tag{4.3}$$

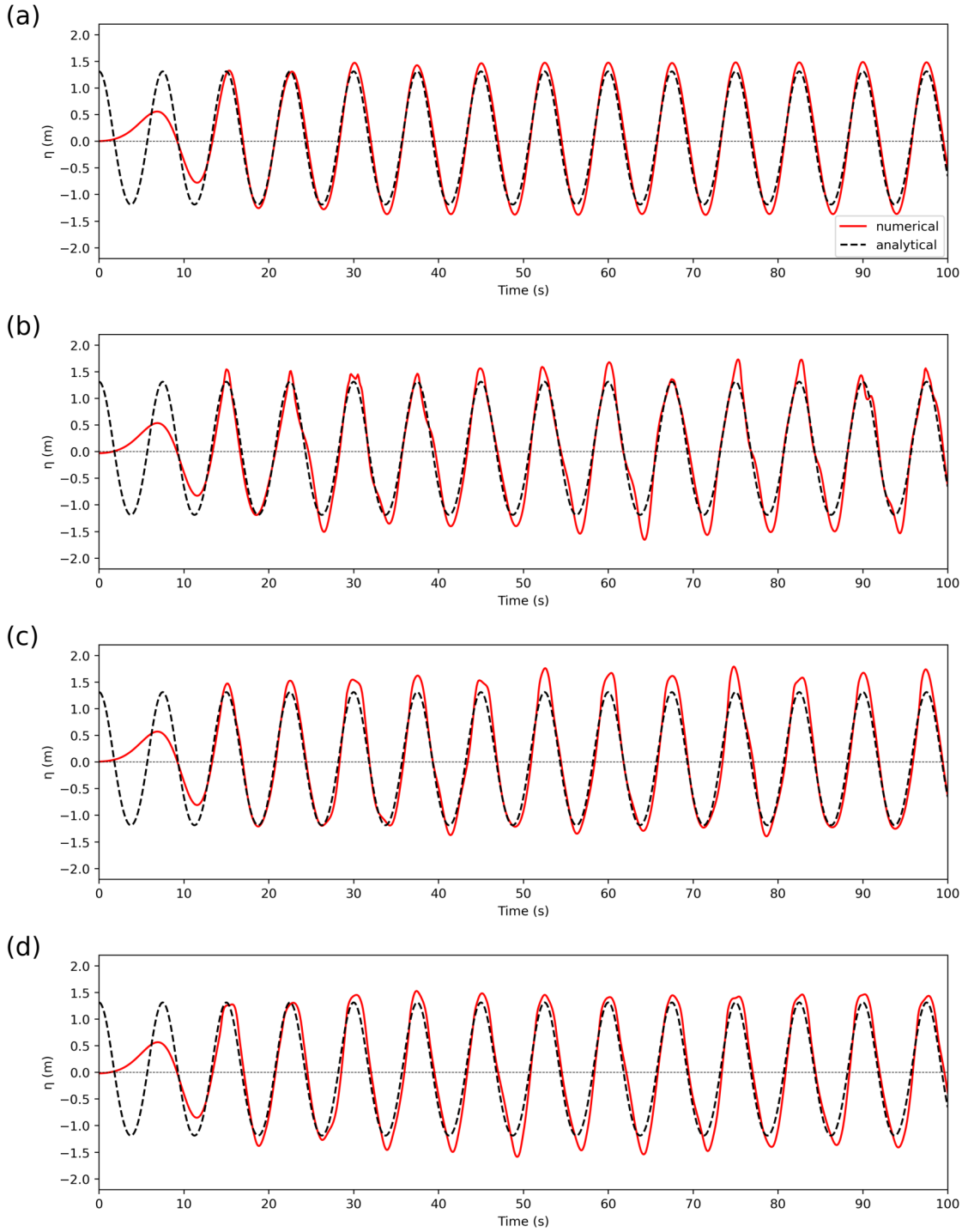

Figure 4.2: Free surface elevation comparison of the different meshes: (a) mesh A; (b) mesh B; (c) mesh C; (d) mesh D; (e) mesh E; (f) mesh F; (g) mesh G. Continues in the next page.

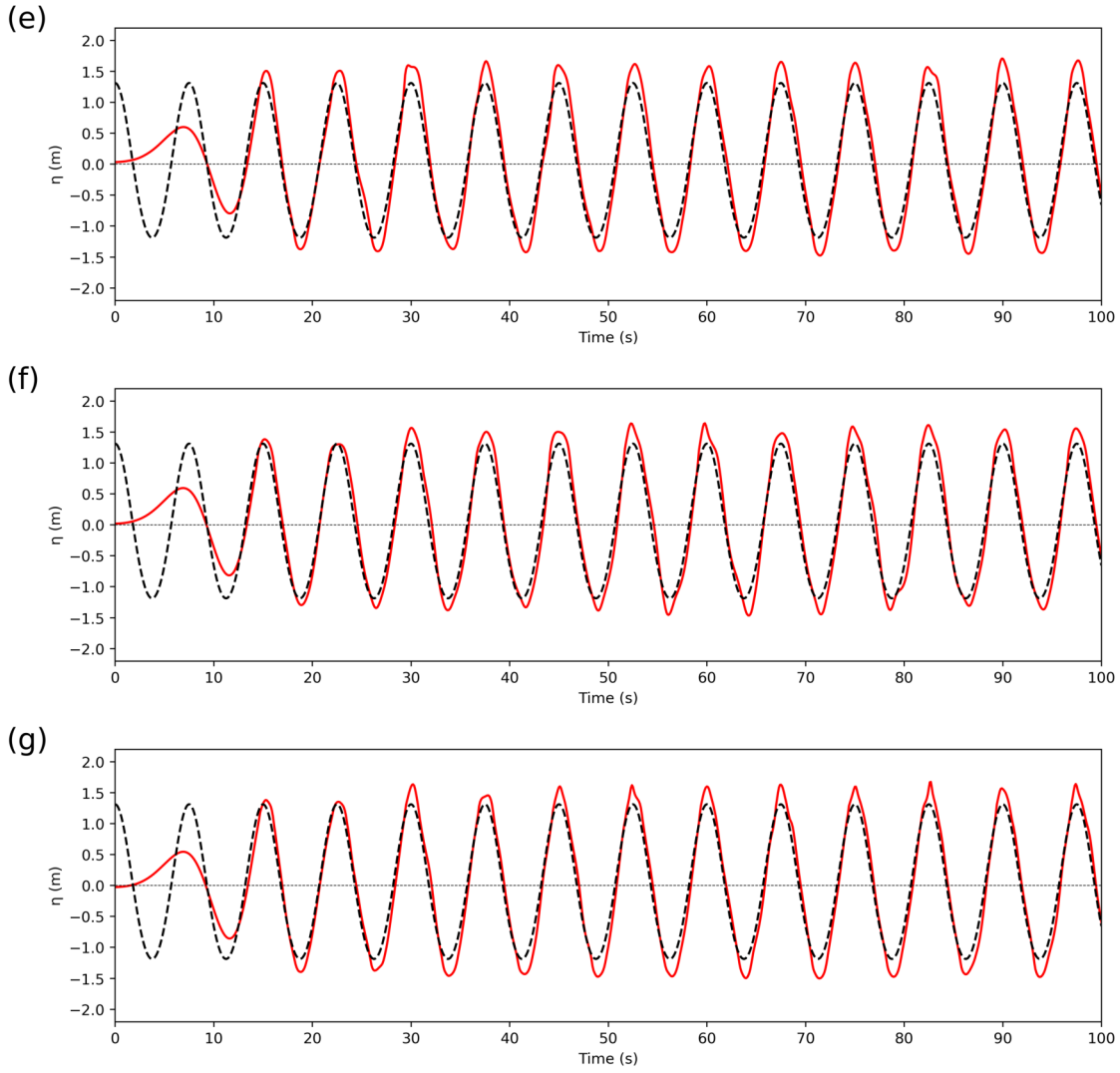

(a) Free surface elevation comparison of the different meshes: (a) mesh A; (b) mesh B; (c) mesh C; (d) mesh D; (e) mesh E; (f) mesh F; (g) mesh G.

where χ_i is the magnitude of the analysed signal, N is the number of samples, and superscripts num and exp refer to numerical and experimental values, respectively. Note that a perfect agreement between signals would result in $A_\chi \to 1$ and $\varphi_\chi \to 0$.

Table 4.3 characterizes the different meshes used for the validation study, where the total number of elements, cells per wave height, simulation run time, A_χ and φ_χ is given.

Figure 4.3 and Figure 4.4 show a graphical representation of the statistical parameters for the different meshes. From the analysis of these Figures and Table 4.3 it is observed that for cells/H ≥ 8, A_χ reaches an oscillatory convergence, with $A_\chi \approx 1.18$ obtained. As for φ_χ, as cells/H increases lower values are achieved, i.e. reaches a monotonic convergence. However, cells/H = 8 was shown to be accurate enough to simulate η with relative low computational cost, about 176 min for 100s of physical time. Simulations have been executed in an Intel(R) Xeon(R) Gold 6242R CPU @ 3.10GHz processor and NVIDIA Quadro RTX 4000 graphics card.

Table 4.3: Used meshes for wave generation and propagation study.

mesh	elements	cells/H	runTime (min)	A_χ	φ_χ
A	120,000	4	70	1.13	0.187
B	266,500	6	74	1.13	0.251
C	501,000	8	176	1.18	0.247
D	680,500	10	266	1.17	0.29
E	1,165,500	12	620	1.19	0.264
F	1,958,000	14	1328	1.17	0.242
G	5,494,500	20	4439	1.18	0.239

These convergence conditions are confirmed in Table 4.4, using the guidelines of [66]. The analysis of A_χ values allows to conclude that the wave maker is overestimating the wave analytical height, as $A_\chi > 1$.

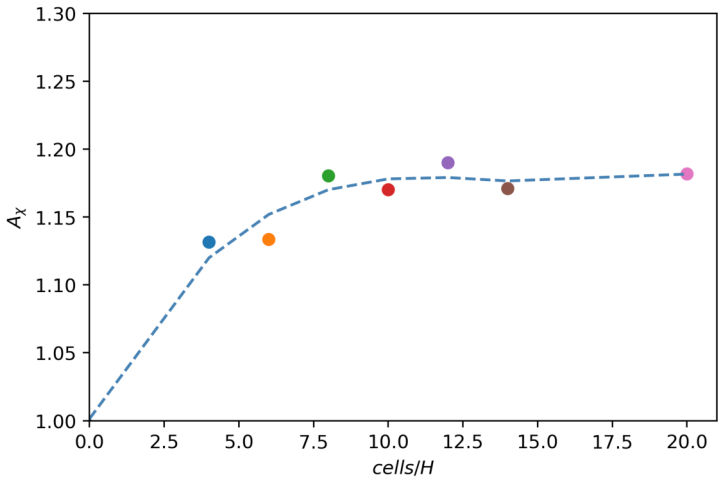

Figure 4.3: Normalized amplitude error comparison for different meshes.

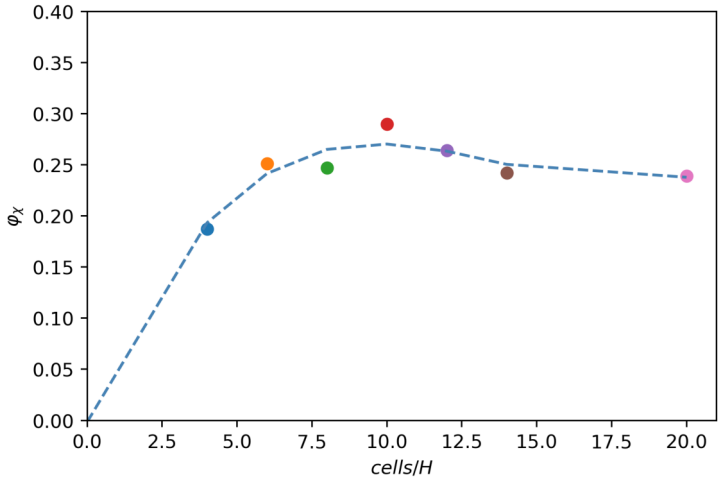

Figure 4.4: Normalized phase error comparison for different meshes.

Table 4.4: Convergence conditions for meshes E, F and G.

parameter	$\hat{S}_{i,1}$	$\hat{S}_{i,2}$	$\hat{S}_{i,3}$	$\varepsilon_{i,21}$	$\varepsilon_{i,32}$	R_i	convergence condition
A_χ	1.18	1.17	1.19	- 0.01	0.02	- 0.5	oscillatory
φ_χ	0.239	0.242	0.264	0.003	0.022	0.136	monotonic

4.2 Evaluation of WEC parameters

The next step in order to validate the numerical model is to introduce the WEC in the computational domain. NWT dimensions are the same as Section 4.1, but with the WEC being located at x = 65m (see Figure 4.5).

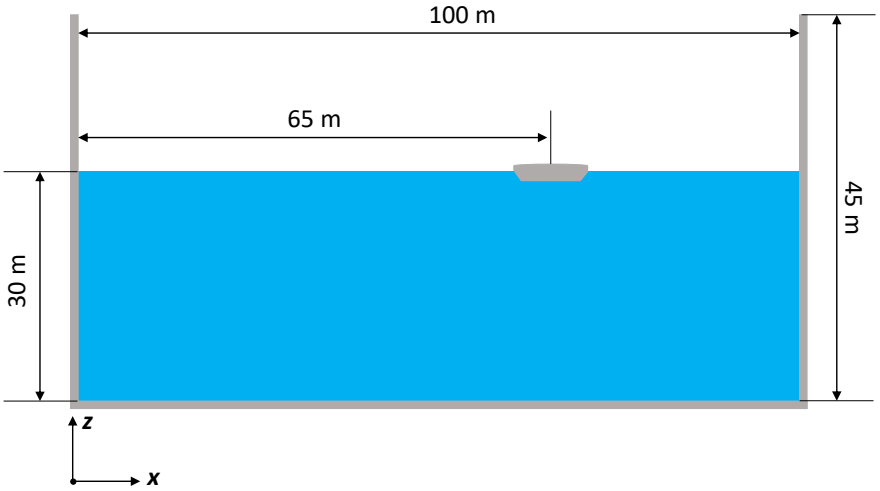

Figure 4.5: WEC position in the NWT, plane $y = 0$.

Figure 4.6 shows the geometry of the WEC used in this thesis. It is easily noticeable that the considered geometry is a simplification of a WEHC, as the lever arm was not considered in the simulations, only the floater. One important aspect to refer is the WEC's draft. As can be seen in Figure 4.6 the draft was designed to be of 1.2 m. This was achieved by setting a density of 638 kg/m^3 for the WEC during the simulations.

Table 4.5 shows the characteristics of the used meshes. As in Section 4.1, 100s of physical time were simulated, with the same hardware being used.

Table 4.5: Used meshes for the evaluation of WEC parameters.

mesh	elements	cells/H	runTime (min)
1	113,500	4	94
2	481,000	8	326
3	681,000	10	559
4	1,155,000	12	1815
5	2,426,000	14	2930

WEC's heave amplitude and angular momentum are the chosen parameters to study the mesh refinement influence, with results being evaluated in the form of a plot over

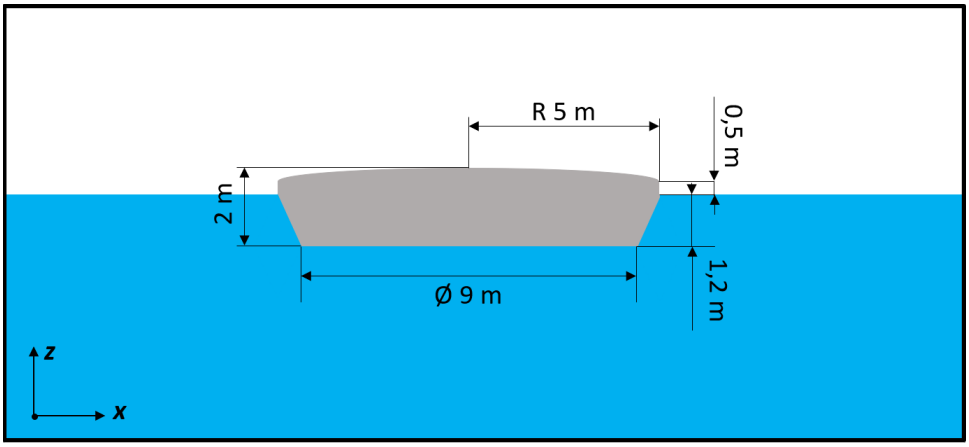

Figure 4.6: WEC geometry.

simulation time. From the analysis of Figure 4.7 and Figure 4.8 no major qualitative differences are observed for the different refinements. Taking into account the conclusions drawn from the previous Section, convergence ratios (R_i) of meshes B, C and D are evaluated in order to conclude about which convergence condition is present. Table 4.6 shows the obtained convergence condition for each parameter. It is observed that for the mean max angular momentum parameter an oscillatory convergence condition is achieved. Whereas, for the mean max heave amplitude parameter a monotonic converge condition, characterized by a convergence ratio (R_i) very close to one (i.e minimal variations between meshes results), is achieved.

Considering the results obtained from this Section and from Section 4.1 it can be concluded that a mesh with height cells per wave height (8 cells/H) is refined enough to numerically study the WEC.

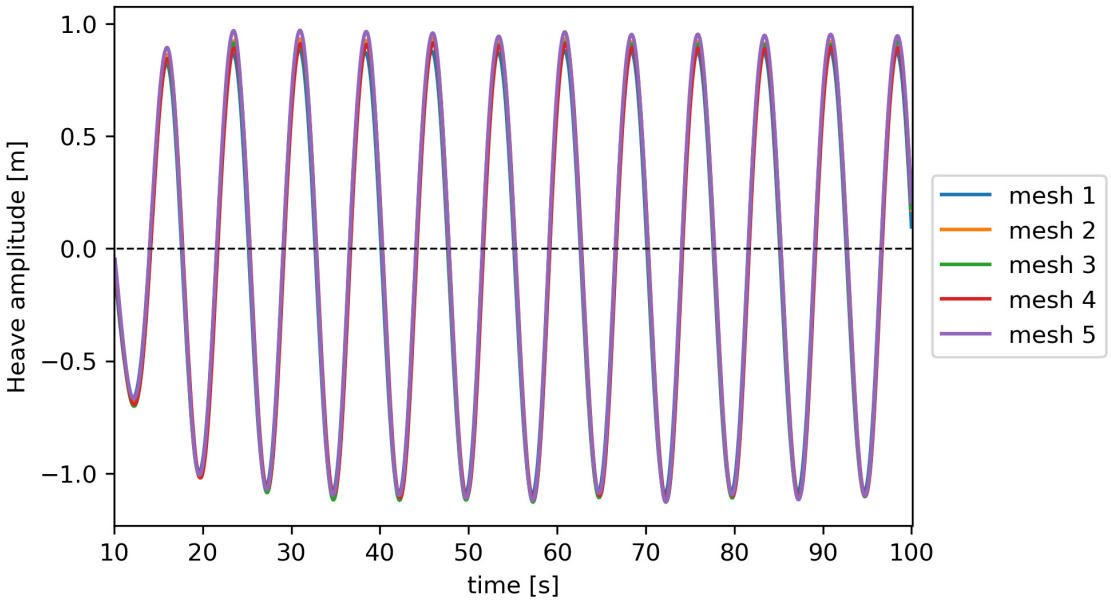

Figure 4.7: Heave amplitude comparison for the different meshes.

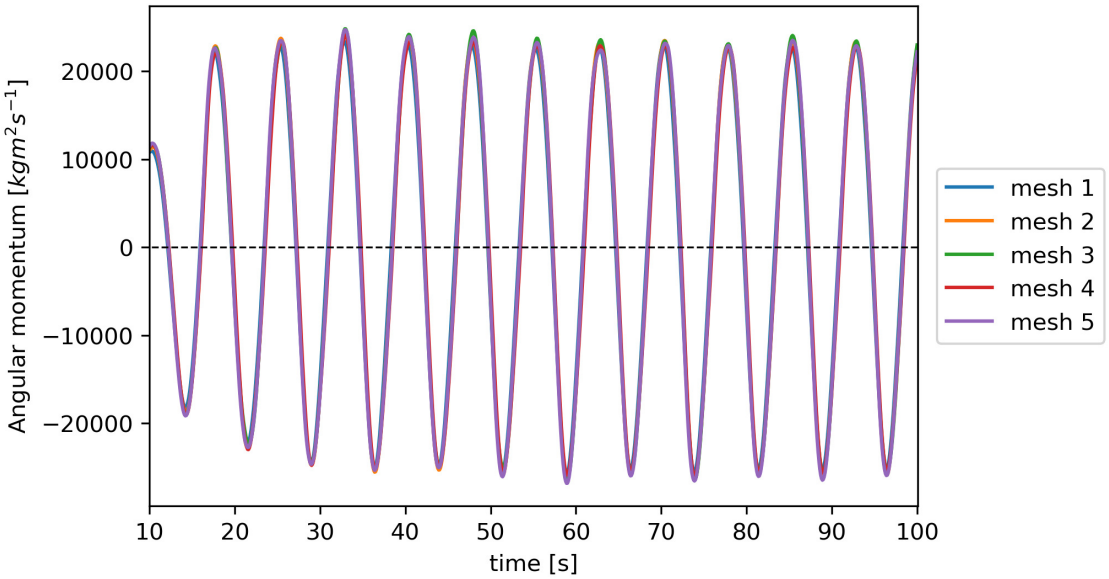

Figure 4.8: Angular momentum comparison for the different meshes.

Table 4.6: Convergence conditions for meshes 2, 3 and 4.

parameter	mean max heave amplitude	mean max angular momentum
$\hat{S}_{i,1}$	0.9008	23061.72
$\hat{S}_{i,2}$	0.9119	23891.95
$\hat{S}_{i,3}$	0.9234	23441.58
$\varepsilon_{i,21}$	0.0111	830.23
$\varepsilon_{i,32}$	0.0115	-450.37
R_i	0.97	-1.84
convergence condition	monotonic	oscillatory

5

Decay test and regular wave interaction with the WEC device

In order to study the WEC interaction with regular waves a free heave and pitch decay test are first carried out to calculate the WEC's natural period. Afterwards, tests to improve the understanding of the behaviour of the WEC around its heave and pitch natural period are performed. Next, the period and wave height influence on the dynamic behaviour of the WEC is studied. Finally, tests with the PTO system are performed.

5.1 Decay test

The logarithmic decrement (δ) represents the rate at which the amplitude of a free-damped vibration decreases. It is defined as [67]:

$$\delta = \frac{1}{m} \ln\left(\frac{x_i}{x_{i+1}}\right) \tag{5.1}$$

where m is the number of consecutive considered cycles and x_i, x_{i+1} correspond to the first and last amplitude (displacement) considered, respectively.

The logarithmic decrement is dimensionless and is actually another form of the dimensionless damping factor ξ. Once δ is known, ξ can be calculated by:

$$\xi = \frac{\delta}{\sqrt{(2\pi)^2 + \delta^2}} \tag{5.2}$$

The damped period T_d can be obtained from the decay test results and is given by:

$$T_d = \frac{n\ cycles\ time}{n^\circ\ cycles} \tag{5.3}$$

After calculating T_d the damped frequency, ω_d, can be calculated by:

$$\omega_d = \frac{2\pi}{T_d} \tag{5.4}$$

Finally, after ω_d is known, the natural frequency (ω_n) can be calculated with:

$$\omega_n = \frac{\omega_d}{\sqrt{1-\xi^2}} \tag{5.5}$$

5.1.1 Free heave decay test

For the free heave decay test the WEC is only allowed to heave, being restrained from any other movement (1 DoF). The WEC is initially fully submerged, being displaced 0.8 m from its equilibrium position, and then released.

5.1.1.1 Device motion

Figure 5.1 shows the initial WEC position for the free heave decay test of the WEC and Figure 5.2 shows the results obtained from the first 10s of the test.

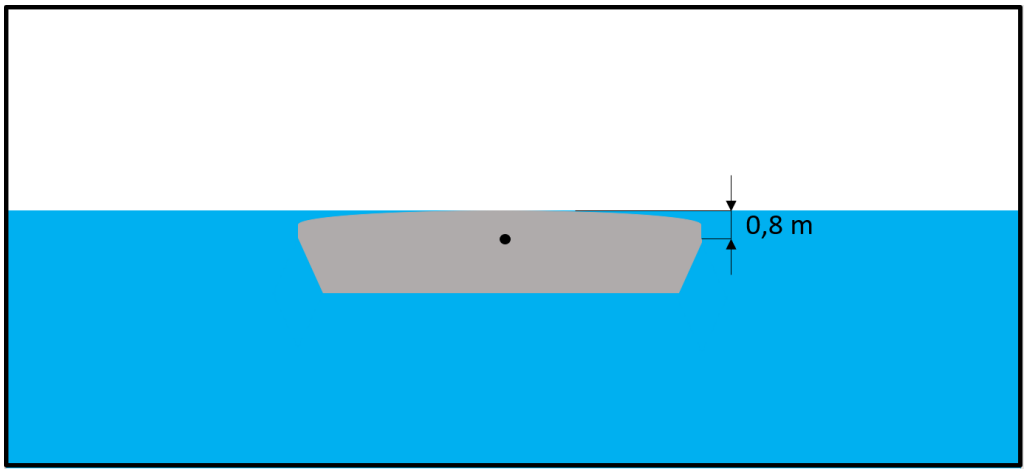

Figure 5.1: Initial WEC position for the free heave decay test.

Table 5.1 shows the extracted values from Figure 5.2, which are used to calculate the free heave natural period.

Table 5.1: Free heave decay test characteristics.

	time (s)	heave amplitude (m)
peak 1	2.2	0.502
peak 2	6.2	0.154

The heave damped period is given by:

$$T_d = \frac{6.2-2.2}{1} = 4s \tag{5.6}$$

The heave logarithmic decrement is obtained as:

$$\delta = \frac{1}{1}\ln\left(\frac{0.502}{0.154}\right) = 1.182 \tag{5.7}$$

After δ is known, the damping factor is calculated:

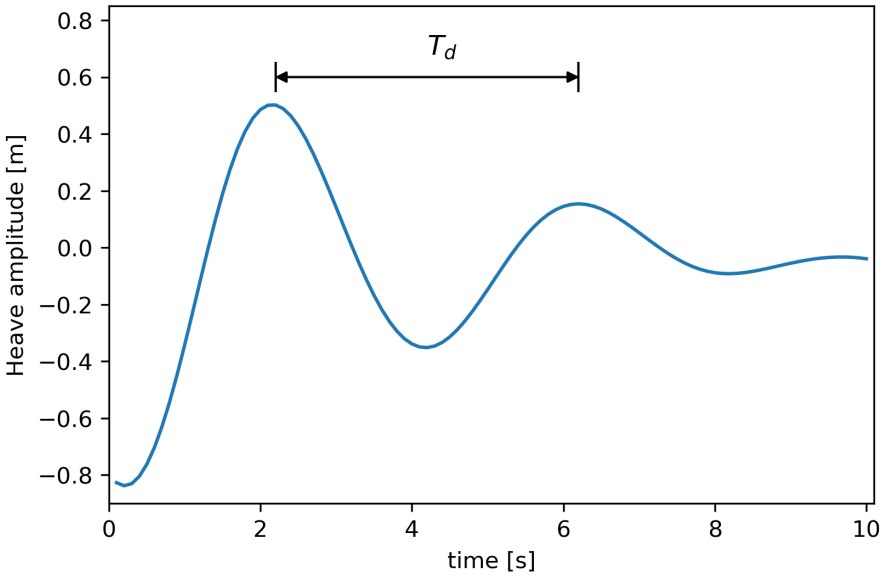

Figure 5.2: Free heave decay test.

$$\xi = \frac{1.182}{\sqrt{(2\pi)^2 + 1.182^2}} = 0.1849 \tag{5.8}$$

The damped frequency is given by:

$$\omega_d = \frac{2\pi}{4} = 1.5708 \frac{rad}{s} = 0.25Hz \tag{5.9}$$

Finally, the heave natural frequency and heave natural period T_n are calculated in Equation (5.10) and Equation (5.11), respectively:

$$\omega_n = \frac{1.5708}{\sqrt{1 - 0.1849^2}} = 1.5984 \frac{rad}{s} = 0.2544Hz \tag{5.10}$$

$$T_n = \frac{1}{\omega_n} = \frac{1}{0.2544} \approx 4s \tag{5.11}$$

5.1.1.2 Velocity and pressure fields

Figure 5.3 shows the velocity and pressure fields around the WEC from 0.1 to 10 seconds. At 0.1 and 0.5 seconds, the WEC is still fully submerged and the magnitude of the velocity field is minimal; at 1.0 seconds, the pressure bellow the WEC increased and the magnitude of the velocity field around it also increased, as it was starting to ascend; at 2.2 seconds, which is the first crest point of the heave motion of the WEC, it is clearly seen that the increase of pressure bellow the WEC caused it to ascend and that the velocity field magnitude in its vicinity also increased; from 3.0 to 4.0 seconds, the pressure bellow the WEC decreases, making it descend and reach the first trough point of the heave motion; vortices can also be observed above the WEC, which dissipated the WEC's kinetic energy; from 5.0 to 6.2 seconds the pressure bellow the WEC increased, causing it to

ascend and reach the second crest point; from 8.0 to 10.0 seconds the WEC reaches its neutral position.

The vortices observed around the WEC are not in its vicinity. In addition, the vortices only appeared in the air phase, not in the water phase. As for the WEC's study the water phase is of greater importance, due to the hydrodynamic forces, the results obtained in this Section confirm that considering a laminar flow is a valid assumption.

5.1.2 Free pitch decay test

For the free pitch decay test the WEC is only allowed to pitch, being restrained from any other movement (1 DoF). The WEC was initially inclined and released with an angle of 15°.

5.1.2.1 Device motion

Figure 5.4 shows the initial WEC position for the free pitch decay test of the WEC. Figure 5.5 shows the results obtained from the first 10s of the test.

Table 5.2 shows the extracted values from Figure 5.5 which are used to calculate the free pitch natural period.

Table 5.2: Free pitch decay test characteristics.

	time (s)	pitch angle (°)
peak 1	0.4	17.587
peak 3	3.9	14.414
peak 3	7.5	12.596

Following the same procedure as in Section 5.1.1 the pitch natural period is calculated in Equation (5.17).

$$T_d = \frac{7.5 - 0.4}{2} = 3.55s \tag{5.12}$$

$$\delta = \frac{1}{2}\ln\left(\frac{17.587}{12.596}\right) = 0.167 \tag{5.13}$$

$$\xi = \frac{0.167}{\sqrt{(2\pi)^2 + 0.167^2}} = 0.0266 \tag{5.14}$$

$$\omega_d = \frac{2\pi}{3.55} = 1.77\frac{rad}{s} = 0.2817Hz \tag{5.15}$$

$$\omega_n = \frac{1.77}{\sqrt{1 - 0.027^2}} = 1.7706\frac{rad}{s} = 0.2818Hz \tag{5.16}$$

$$T_n = \frac{1}{\omega_n} = \frac{1}{0.2818} \approx 3.55s \tag{5.17}$$

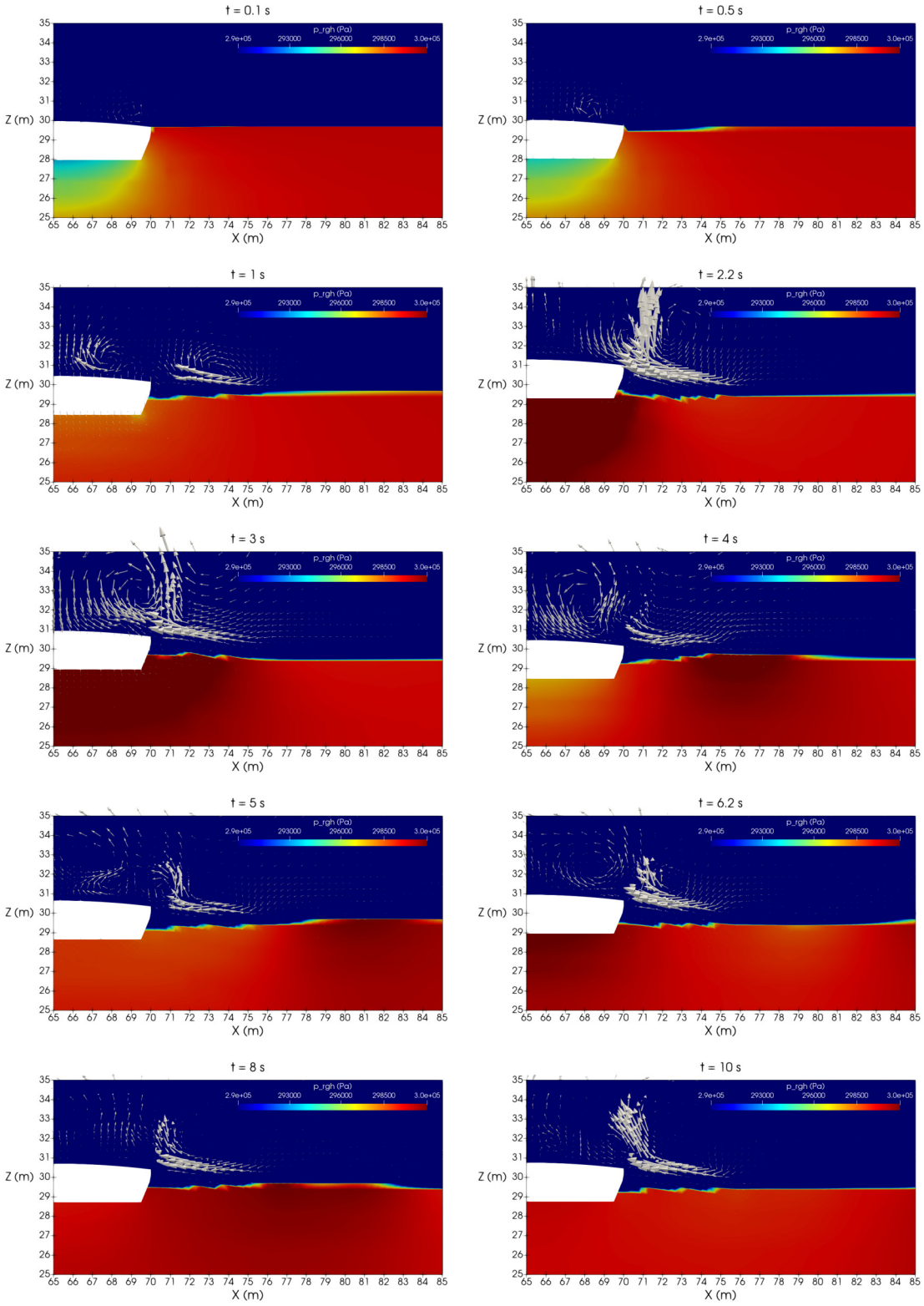

Figure 5.3: Velocity and pressure fields in the vicinity of the WEC at different times along the free heave decay test. The length and direction of the arrows represent the magnitude and the direction of velocity, respectively. The pressure field is shown by the color gradient. Plane $y = 0$.

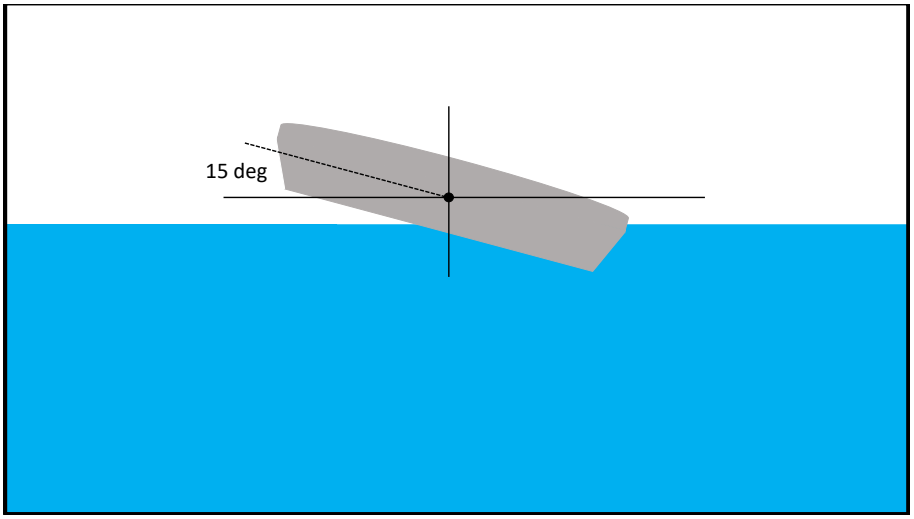

Figure 5.4: Initial WEC position for the free pitch decay test.

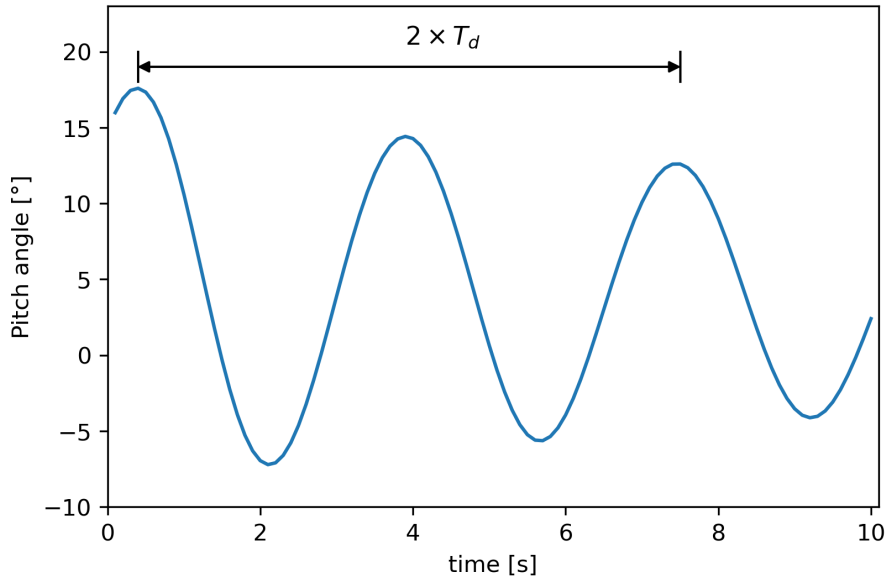

Figure 5.5: Free pitch decay test.

5.1.2.2 Velocity and pressure fields

Figure 5.6 shows the velocity and pressure fields around the WEC from 0.1 to 7.5 seconds. The initial rotation was due to the pressure difference between the two sides of the WEC. The motion of the WEC generated a few vortices around it (in the air phase), which dissipated its kinetic energy. Fluid viscosity and the shift from the pressure gradient in the flow field due to inertial force were the main factors affecting the WEC's motion, reducing its kinetic energy and the amplitude of motion (did not reach its neutral position in the simulation time).

As also seen in Section 5.1.1.2, the vortices observed around the WEC are not in its vicinity and only appeared in the air phase. Following the results obtained in Section

5.1.1.2 and in this Section, it is confirmed that considering a laminar flow is a valid assumption, which considerably reduces simulations computational cost.

5.2 Wave-Structure interaction

OpenFOAM's laminar flow model is used in all simulation of this Section. The study is carried out in a NWT with the dimensions presented in Figure 4.5. WEC's dimensions are presented in Figure 4.6.

5.2.1 Simulations without PTO system

The study of the WEC, without PTO system, is carried out in order to characterize its behaviour for the different maritime conditions considered. This study allows to compare these results with the ones from the simulations with PTO system.

5.2.1.1 Heave and pitch motion around WEC's heave natural period

Figure 5.7 and Figure 5.8 show the time histories of the heave amplitude of the WEC for different wave periods of T = 3 s, 4 s and 5 s from 50 s to 100 s of simulation time, when the wave has been fully developed and has reached its stable state. Due to the resonance effect, it is expected that the heave amplitude of the WEC is largest for the case with T = 4 s, which corresponds to the heave natural period of the WEC. Nevertheless, as the heave natural period is calculated with only 1 DoF (heave only) and in this case the WEC is allowed to heave and pitch, the expected results are not verified. These results allow to conclude that the pitch movement modified the heave natural period of the WEC.

Results in Figure 5.7 and Figure 5.8 show that the heave amplitude systematically increases with the increase of the wave period, for the considered wave heights. When analysing Figure 5.9 and Figure 5.10 it is verified that when T = 4 s (heave natural period) the pitch angle amplitude is the largest. The cases with T = 3 s and T = 5 s show similar pitch motion.

In order to better understand how the heave amplitude of the WEC changes when interacting with regular waves some more tests are carried out, which can be seen in Section 5.2.1.3.

5.2.1.2 Heave and pitch motion around WEC's pitch natural period

Figure 5.11 and Figure 5.12 show the time histories of the pitch amplitude of the WEC for different wave periods of T = 3 s, 3.55 s and 4 s from 50 s to 100 s of simulation time, when the wave has been fully developed and has reached its stable state. As in Section 5.2.1.1, it is expected that the pitch amplitude of the WEC is largest for the case correspondent to the pitch natural period, T = 3.55 s, but this is not verified by the results.

Results in Figure 5.12 show that the pitch amplitude systematically increases with the increase of the wave period, whereas in Figure 5.11 the results are not linear. In Figure

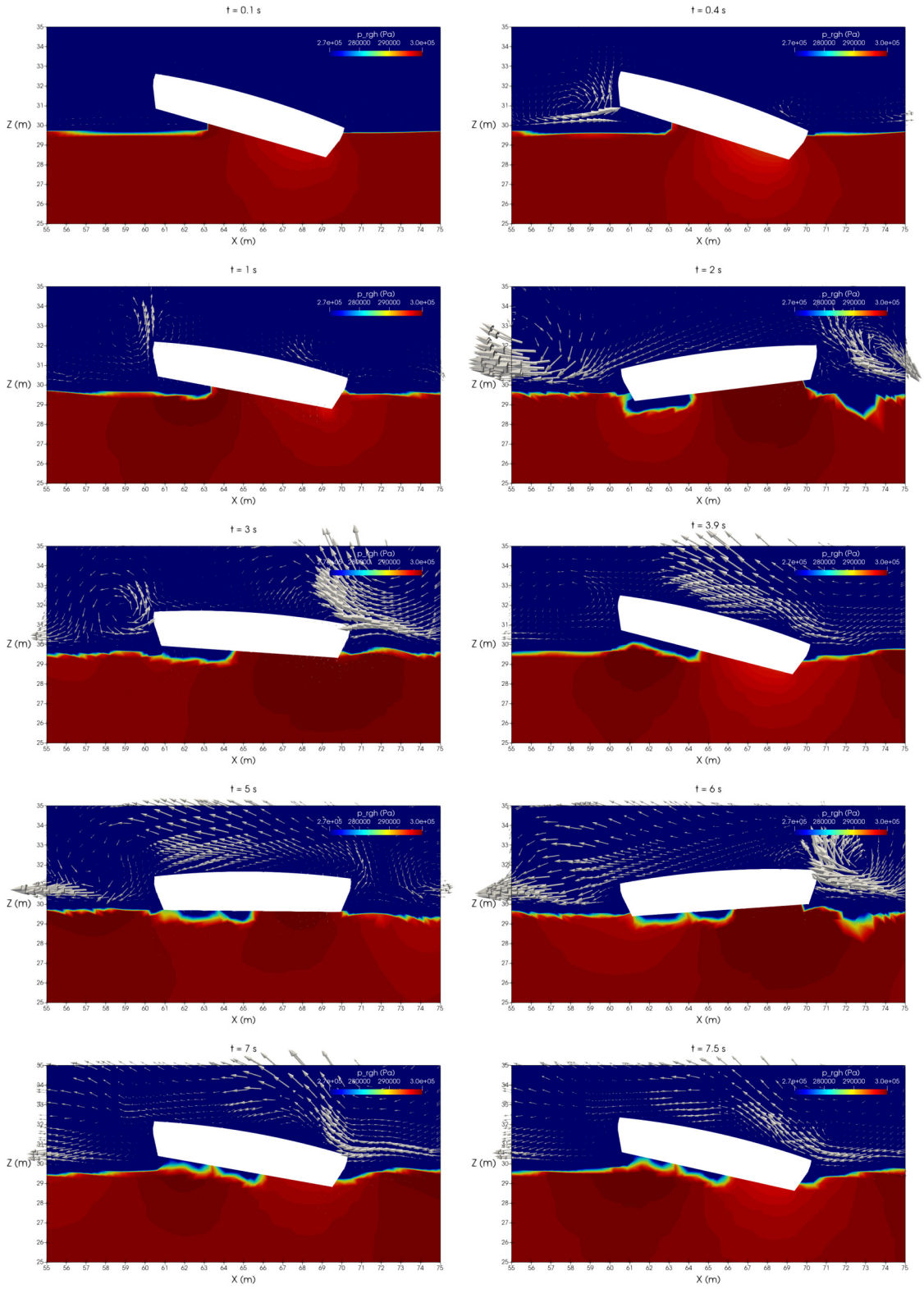

Figure 5.6: Velocity and pressure fields in the vicinity of the WEC at different times along the free pitch decay test. The length and direction of the arrows represent the magnitude and the direction of velocity, respectively. The pressure field is shown by the color gradient. Plane $y = 0$.

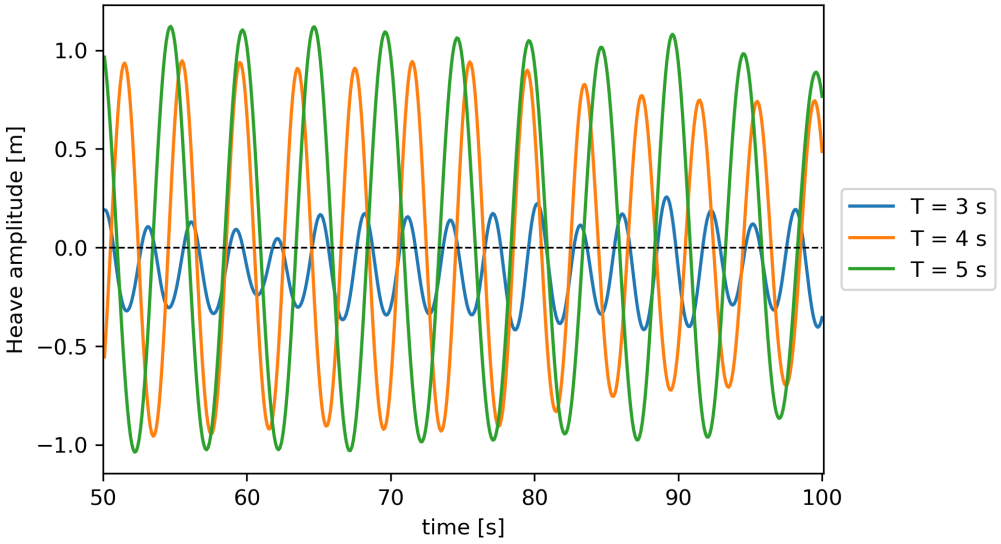

Figure 5.7: Time histories of the heave amplitude of the WEC at wave periods around heave natural period, for H = 1.5 m.

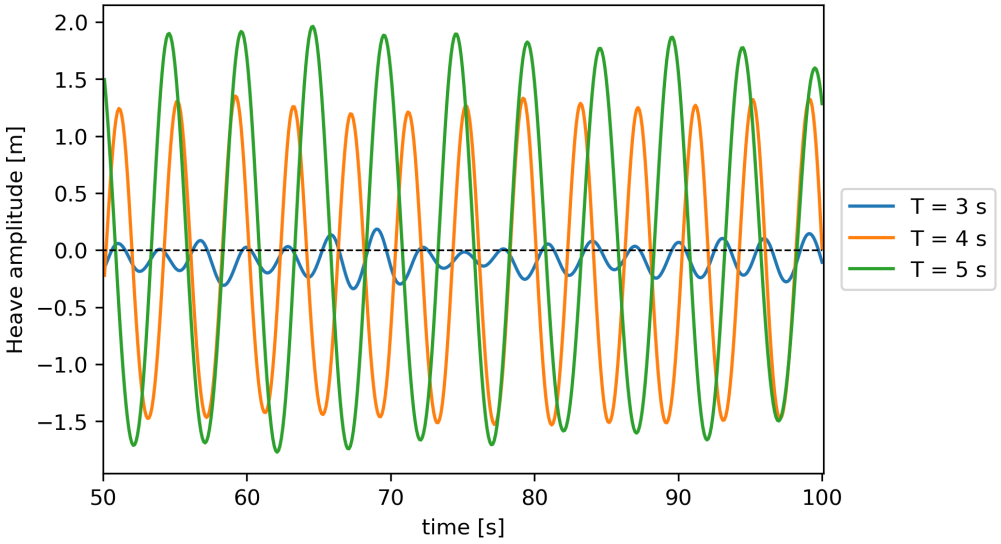

Figure 5.8: Time histories of the heave amplitude of the WEC at wave periods around heave natural period, for H = 2.5 m.

5.14 it is seen that the heave amplitude increases with the increase of the wave period, for the considered wave height, and is maximum for T = 4 s. Results in Figure 5.13 also show that the heave amplitude is maximum for T = 4 s, but the heave amplitude for T = 3 s and T = 3.55 s are similar.

In order to better understand how the pitch amplitude of the WEC changes when interacting with regular waves some more tests are carried out, which can be seen in Section 5.2.1.3.

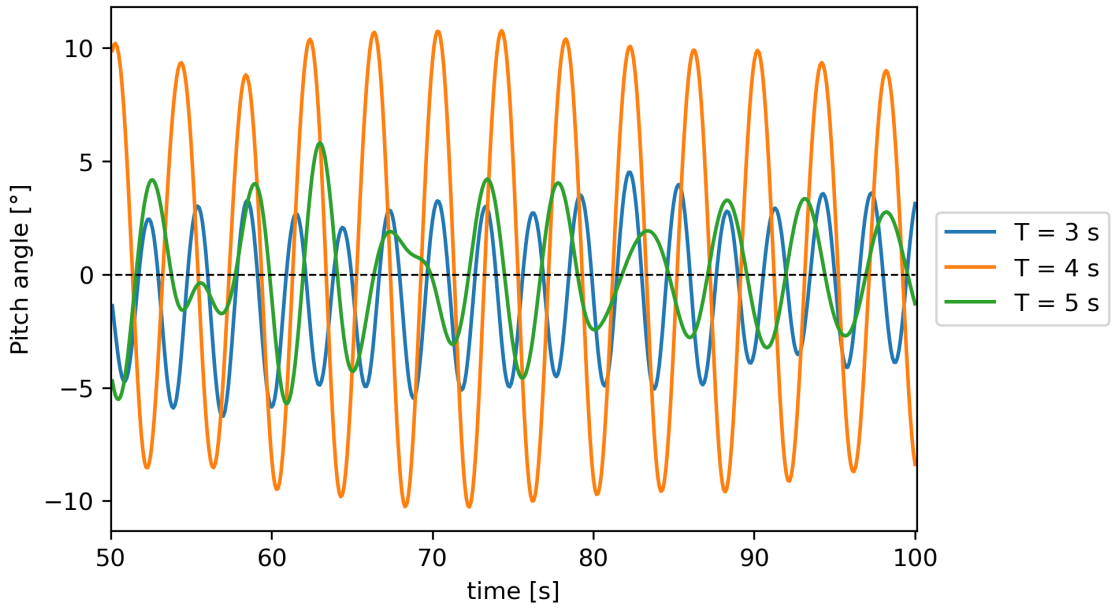

Figure 5.9: Time histories of the pitch angle of the WEC at wave periods around heave natural period, for $H = 1.5$ m.

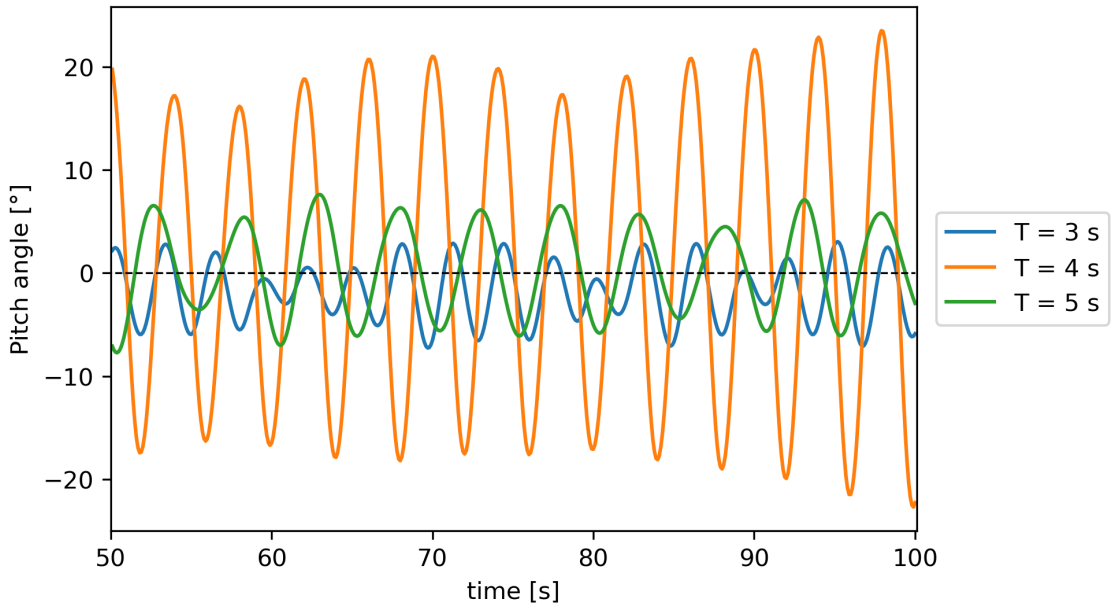

Figure 5.10: Time histories of the pitch angle of the WEC at wave periods around heave natural period, for $H = 2.5$ m.

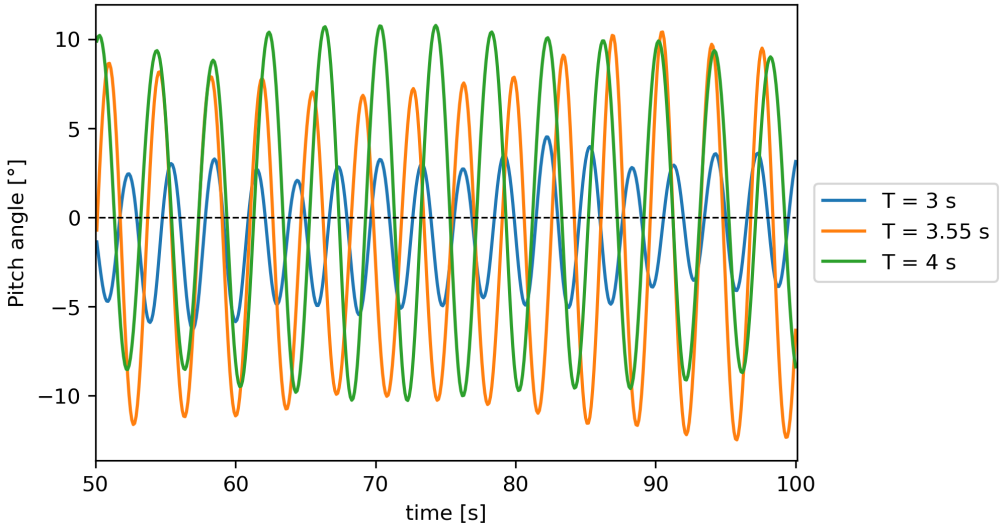

Figure 5.11: Time histories of the pitch angle of the WEC at wave periods around pitch natural period, for $H = 1.5$ m.

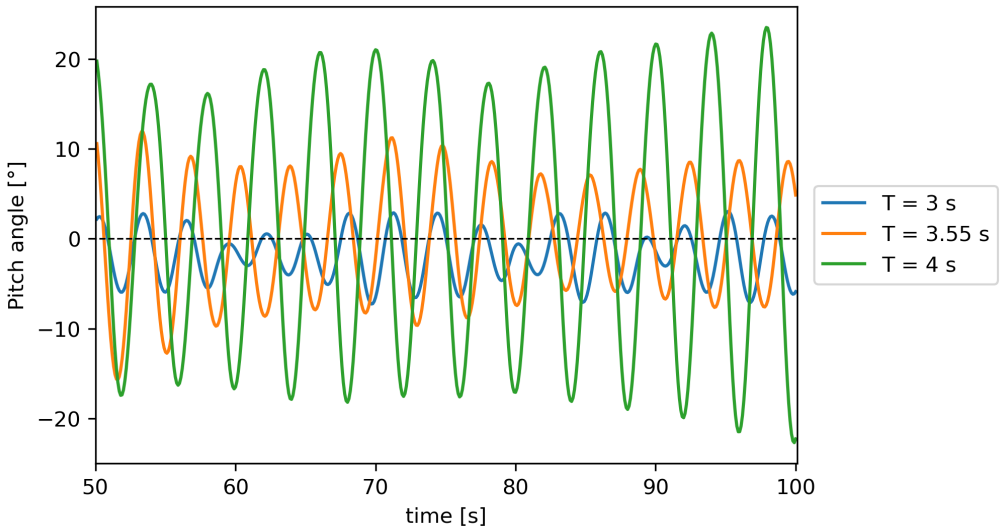

Figure 5.12: Time histories of the pitch angle of the WEC at wave periods around pitch natural period, for $H = 2.5$ m.

5.2.1.3 Period and wave height influence

In order to better represent the dynamic behaviour of the WEC under regular waves the response amplitude operator (RAO) parameter is used, given by:

$$\text{RAO} = \frac{|\theta_{max} - \theta_{min}|}{H} \tag{5.18}$$

where θ_{max} and θ_{min} are the maximum and minimum values of the WEC's heave amplitude, respectively.

Figure 5.15 and Figure 5.16 show the heave amplitude and the RAO of the WEC for $H = 1.5$ m, respectively. It is observed that for frequencies between 0.18 Hz and

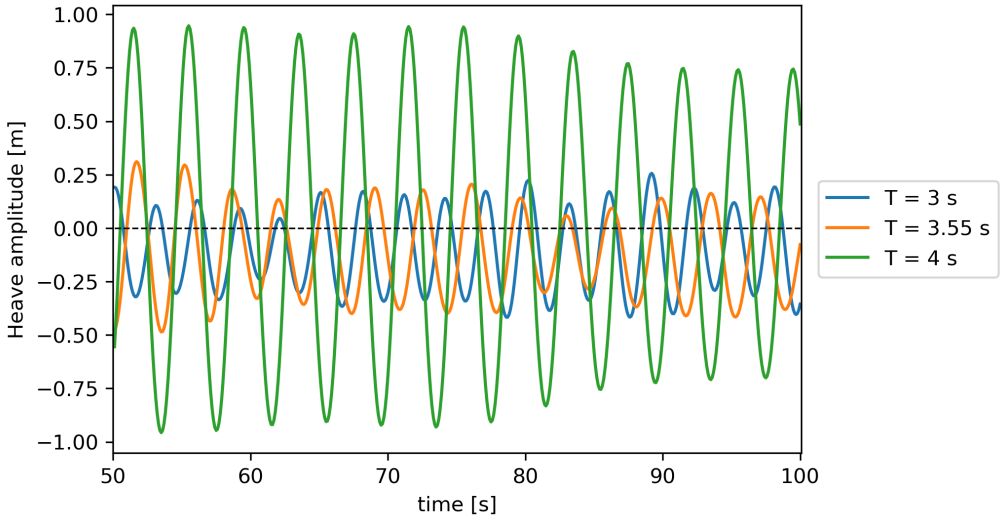

Figure 5.13: Time histories of the heave amplitude of the WEC at wave periods around pitch natural period, for H = 1.5 m.

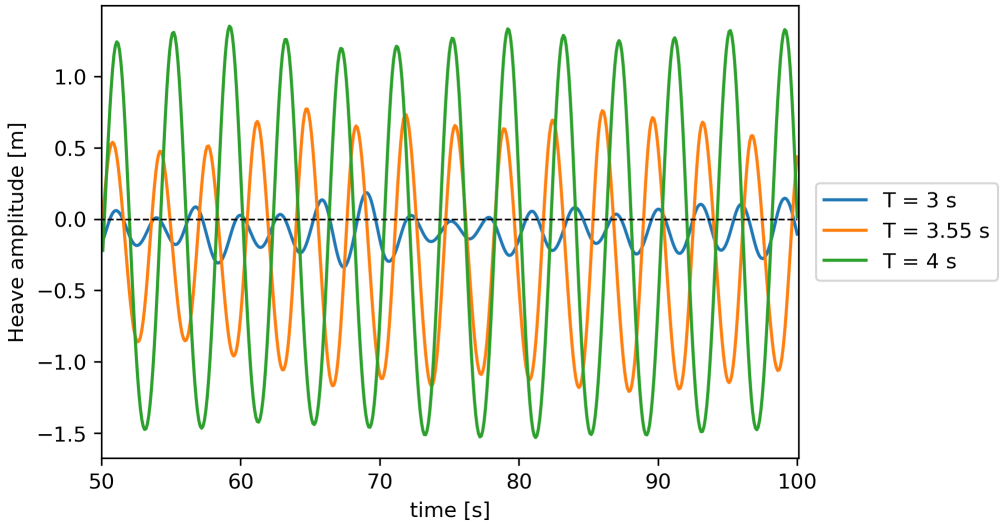

Figure 5.14: Time histories of the heave amplitude of the WEC at wave periods around pitch natural period, for H = 2.5 m.

0.20 Hz the WEC is in resonance with the waves, showing a higher heave amplitude. These Figures also show an amplitude peak for lower frequencies. This behaviour can be explained taking into account that for longer period waves (lower frequencies), the WEC moves linearly with the free surface motion, following the waves movement. For higher frequencies (shorter waves) the WEC cannot follow the free surface motion, as the waves' length is smaller than the WEC's diameter. Consequently, the WEC is in contact with multiple wave crests simultaneously, which maintains it in a stable position, decreasing its amplitude motion.

Figure 5.17 and Figure 5.18 show the heave amplitude and the RAO of the WEC for H = 2.5 m, respectively. Figure 5.17 appears to be similar to Figure 5.15, however, it shows

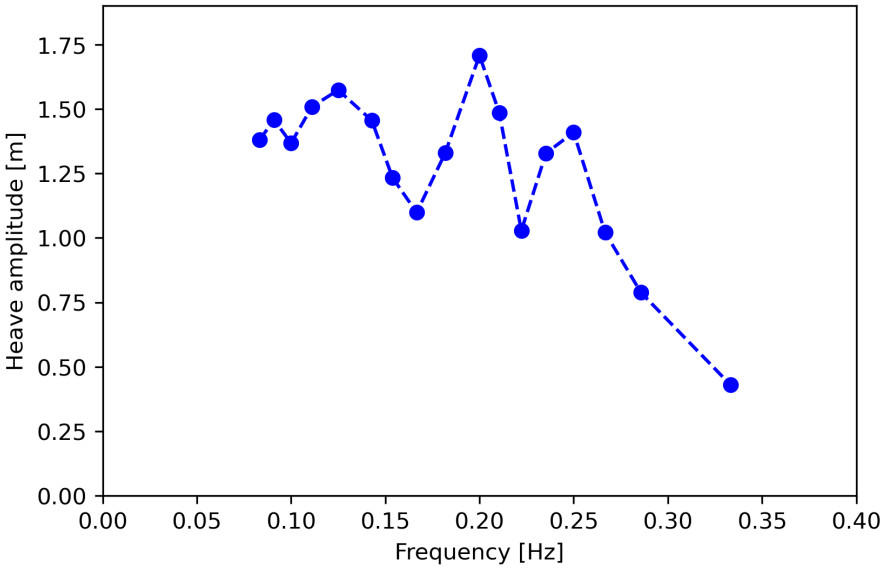

Figure 5.15: WEC's heave amplitude, for $H = 1.5$ m.

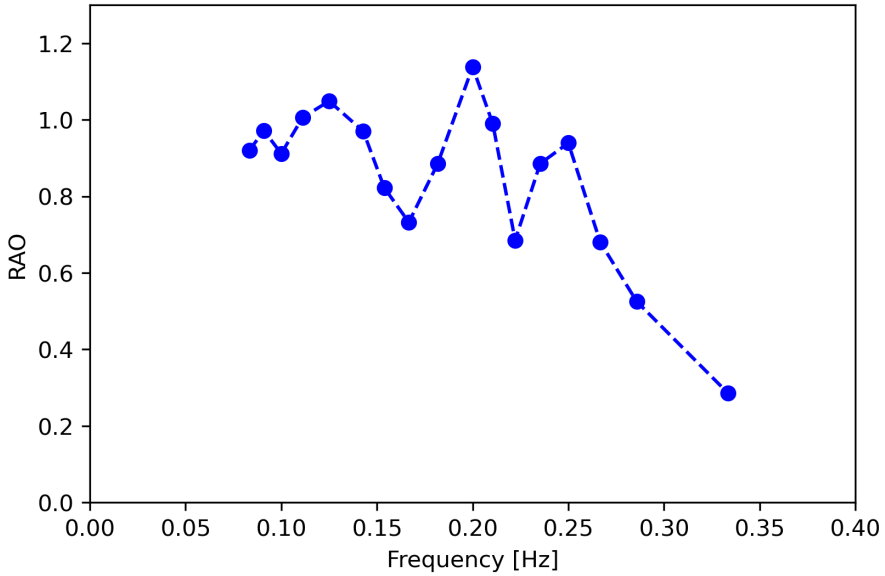

Figure 5.16: WEC's RAO, for $H = 1.5$ m.

higher heave amplitudes, as the wave height considered is also higher. Similarly to the waves with $H = 1.5$ m, it is observed that the WEC is in resonance with the waves for frequencies between 0.18 Hz and 0.20 Hz.

Figure 5.19 shows a comparison of the WEC's heave amplitude between the two wave heights simulated. The analysis of this Figure allows to conclude that for higher wave heights, the WEC device also responds with higher amplitudes of motion. However, for higher frequencies (around 0.34 Hz), the two cases overlap. Both cases show an amplitude peak for frequencies around 0.20 Hz ($T = 5$ s) and an amplitude low for frequencies around 0.16 Hz ($T = 6.25$ s). These results lead to the conclusion that, for the cases

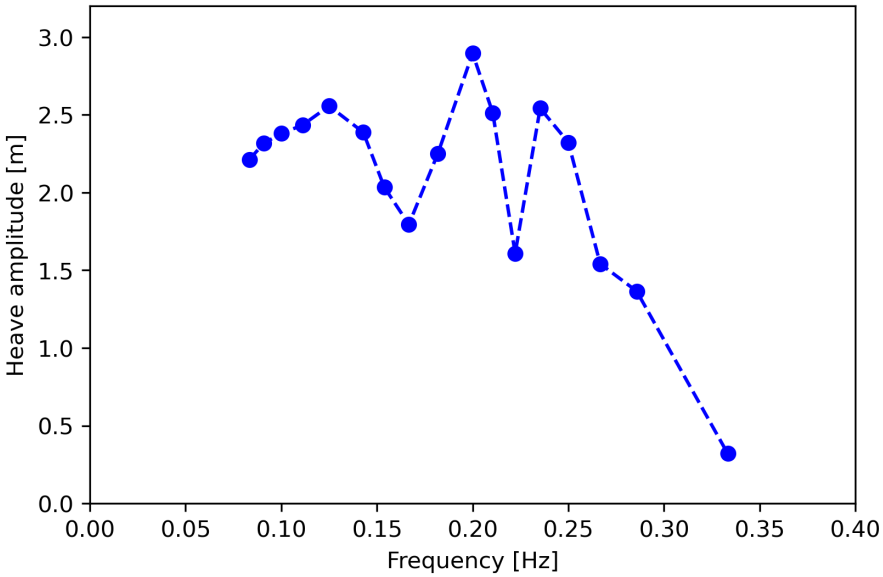

Figure 5.17: WEC's heave amplitude, for $H = 2.5$ m.

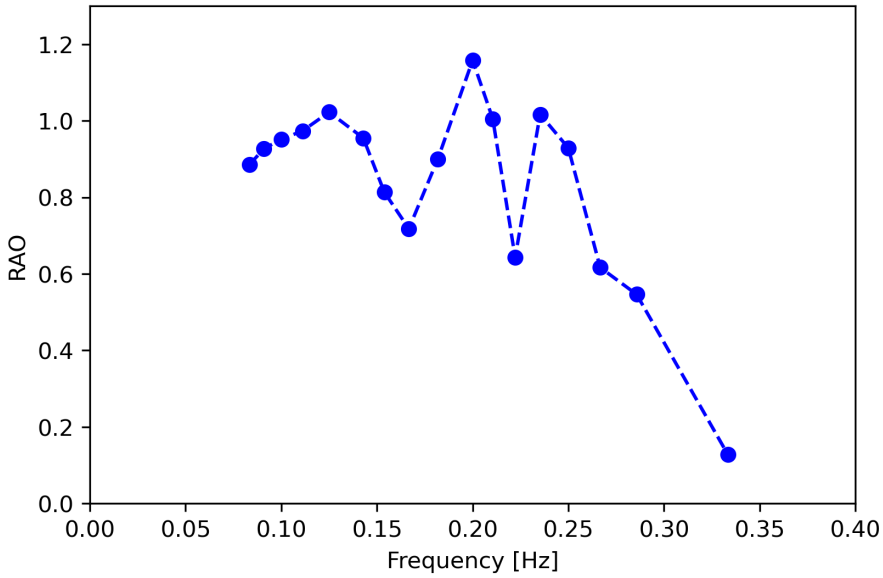

Figure 5.18: WEC's RAO, for $H = 2.5$ m.

considered, wave frequencies around 0.20 Hz correspond to the WEC's resonance zone and frequencies around 0.16 Hz lead to lower heave amplitudes.

Figure 5.20 shows the WEC's RAO for the different wave heights simulated. RAO is considered a better parameter to compare the WEC's behaviour for different wave heights, as it is a dimensionless parameter. Figure 5.20 shows that the differences between the two cases are minimal, which allows to conclude that the wave height does not have a significant influence in RAO, meaning that the increase in the WEC's heave amplitude is linearly proportional to the increase in the wave height.

As the wave height value introduced in OpenFOAM can slightly differ from the wave

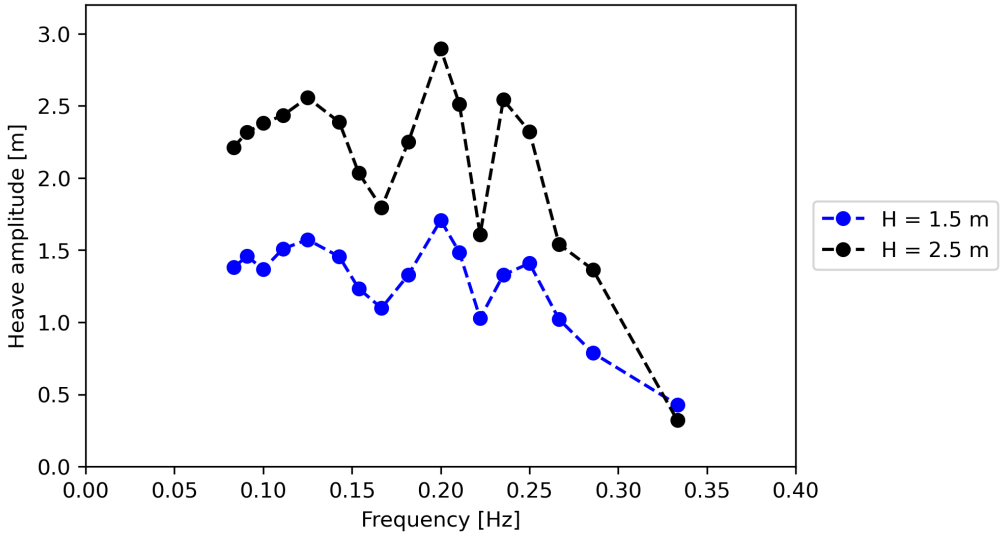

Figure 5.19: Comparison between the WEC's heave amplitude for the wave heights simulated.

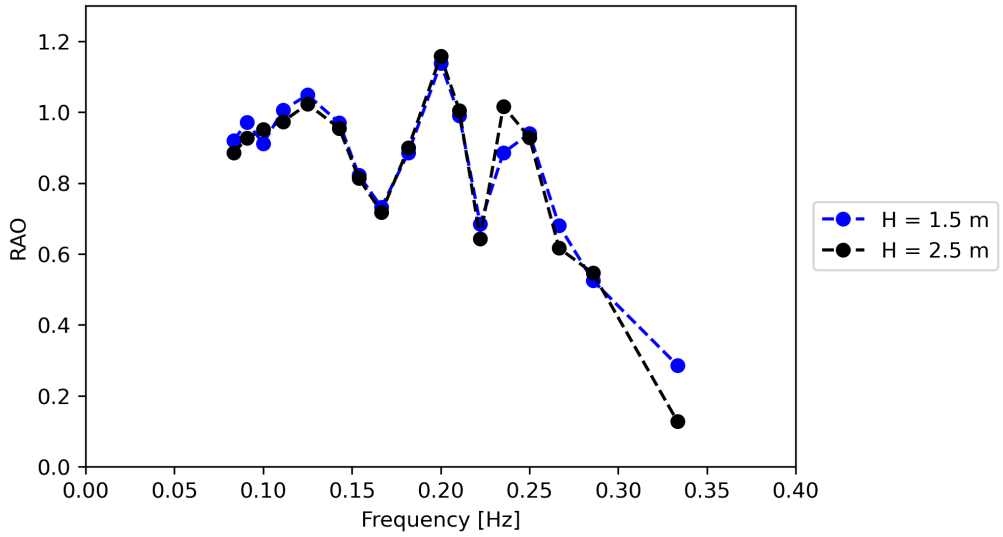

Figure 5.20: Comparison between the WEC's RAO for the wave heights simulated.

height actually generated, some modifications are performed to better represent the RAO parameter. The RAO parameter is considered to be the ratio between the WEC's heave amplitude and the measured wave height, instead of the wave height value introduced in OpenFOAM. The new RAO parameter is given by:

$$\text{RAO} = \frac{|\theta_{max} - \theta_{min}|}{H_{measured}} \tag{5.19}$$

To obtain the most accurate results, three points along the NWT are considered to measure the free surface elevation. These points are located at 35 m, 45 m and 55 m from the wave maker, with the last point being 5 m from the WEC. All points are upstream of the WEC. Figure 5.21 shows the RAO parameter for the chosen locations. In addition,

the RAO parameter is also calculated using the mean value of the free surface elevation for the three different chosen locations.

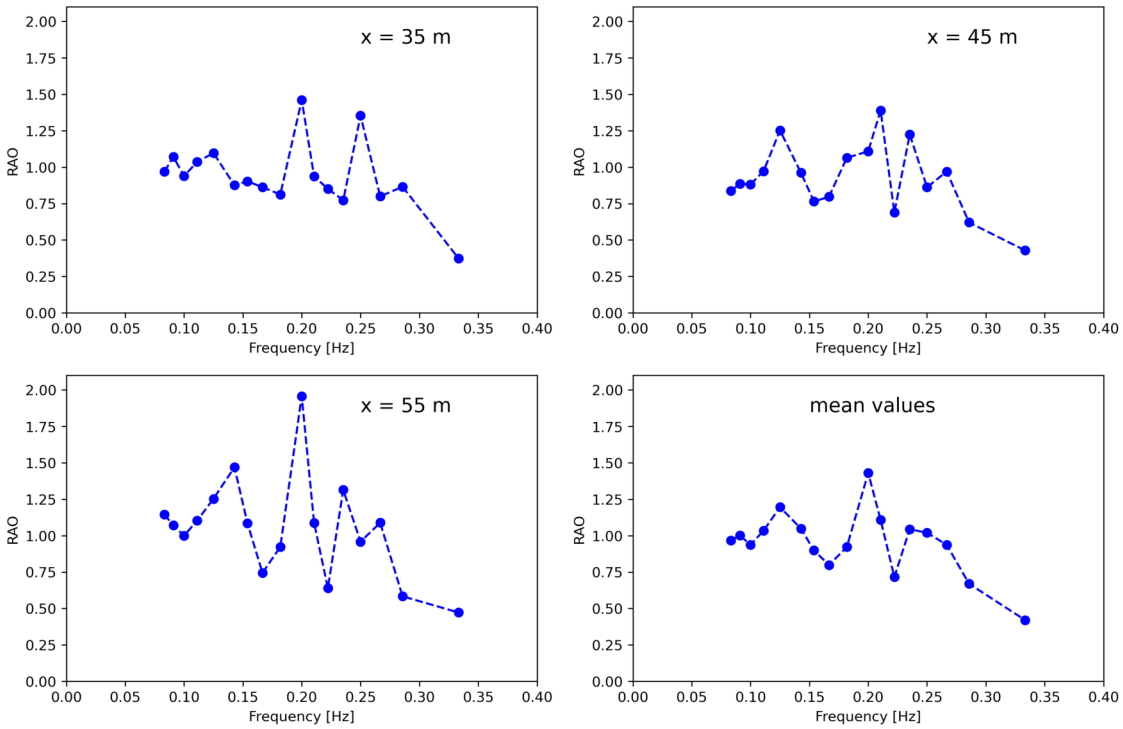

Figure 5.21: RAO comparison, for $H = 1.5$ m.

Figure 5.21 shows that the RAO parameter is very irregular and quite distinct for the different locations. These results can be explained by the reflection of waves on the device, which leads to the propagation of waves in the opposite direction of the generated waves, forming some highly oscillating points in the free surface. Consequently, the obtained results allow to conclude that there is a large variation of the free surface elevation along the NWT, due to the reflection of waves on the device.

Figure 5.21 also shows that the calculated RAO parameters present higher values than the RAO parameter. In Section 4.1 was concluded that OpenFOAM overestimates the waves height, with an empty NWT. These results allow to conclude that the WEC's motion dissipates energy, leading to a decrease in the waves height along the NWT. Figure 5.21 leads to the conclusion that frequencies around 0.20 Hz are the most suitable to extract energy from the waves, for the case in study, as all cases show an amplitude peak around this frequency value.

The RAO parameter was not studied for more wave heights due to the reduced time available and because no major conclusions about the hydrodynamic behaviour of the WEC are taken, when compared to the regular RAO.

The pitch angle variation is also studied to improve the understanding of the dynamic behaviour of the WEC. Figure 5.22 shows a comparison of the WEC's pitch angle between the different wave heights simulated. With the exception of frequencies between 0.10

Hz and 0.15 Hz, where the pitch angle shows similar values, both cases shown in this Figure seem similar, however, for higher wave heights, the WEC device also responds with higher pitch angles. A pitch angle peak for frequencies around 0.28 Hz is observed for both cases.

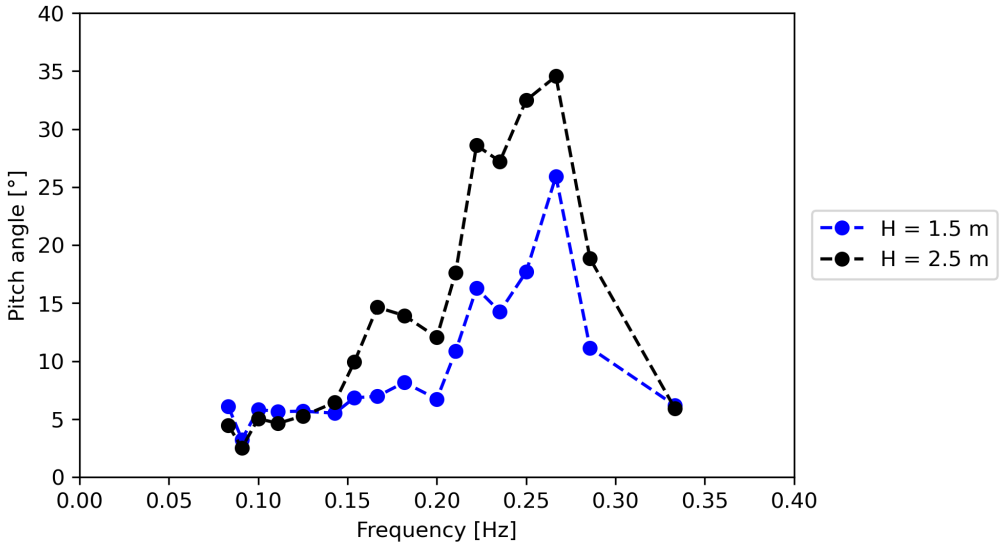

Figure 5.22: Comparison between the WEC's pitch angle for the wave heights simulated.

The pitch angle shows minor variations for both lower frequencies (longer waves) and higher frequencies (shorter waves). This behaviour can be explained taking into account that for longer period waves (lower frequencies) the wave steepness is small, allowing the WEC to follow the free surface motion, only having small variations in the pitch angle. For shorter period waves (higher frequencies), as the wave length is smaller than the WEC's diameter, the WEC has multiple wave crests under it, which restrains its rotation, leading to small variations in the pitch angle.

For a better understanding of how the pitch angle variation influences the WEC's heave amplitude, a comparison between the WEC's RAO and pitch angle is performed, which can be seen in Figure 5.23. It shows that the WEC's RAO peak, around 0.14 Hz, corresponds to a zone where the pitch angle presents small variations. As an amplitude low is reached, around 0.16 Hz, the pitch angle shows its first peak. For frequencies around 0.20 Hz, which correspond to the heave resonance zone, the pitch angle displays a slight decrease and, as another amplitude low is reached, the pitch angle increases again. The pitch angle peak, around 0.28 Hz, is located in a frequency zone where the WEC starts to show some of the lowest amplitude values. For higher frequencies, both the RAO and pitch angle show minor variations.

The obtained results lead to the conclusion that the pitch angle has a direct influence in the WEC's heave amplitude. Results suggest that a decrease in the pitch angle can lead to an increase in the heave amplitude. Improving the knowledge about the relation between the heave amplitude and pitch angle can enhance the WEC's power output.

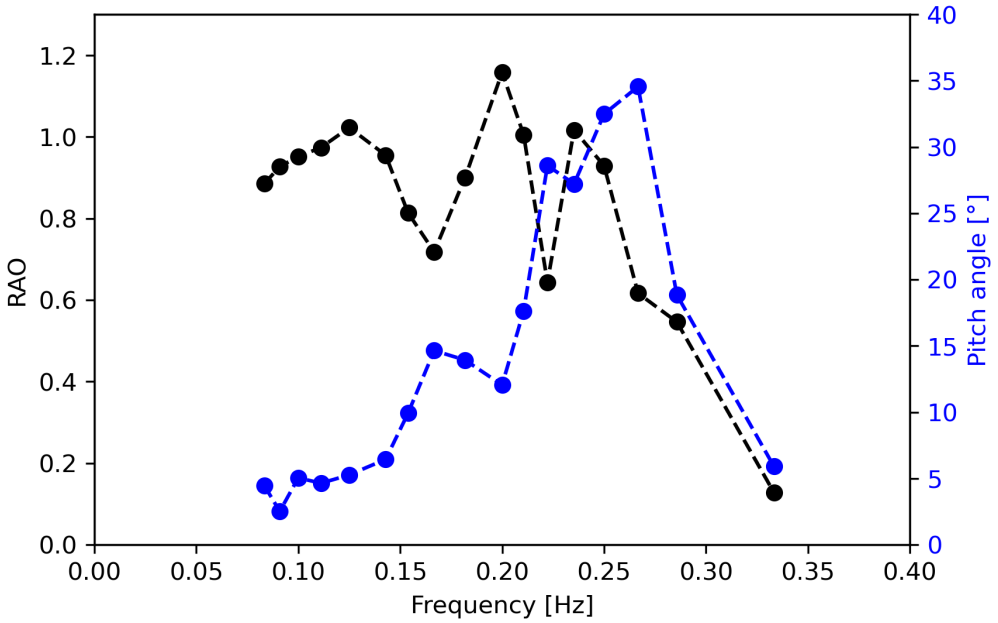

Figure 5.23: Comparison between the WEC's RAO and pitch angle.

5.2.2 Simulations with PTO system

As seen in Section 3.6.2, the PTO system considered in this study applies a damping force in the opposite direction of the body's linear velocity vector. Consequently, this study is carried out considering a double-acting PTO system, i.e., the PTO applies the damping force in both directions. Figure 5.24 shows a comparison of the WEC's heave amplitude between a case without PTO system and other cases with PTO system, with different c_{PTO} values. All cases are run with a mechanical constraint in the WEC's rotational motion, with C_{PTO} = 1000 MNms/rad. The waves generated have H = 2.5 m and T = 5 s.

As expected, the cases that have a PTO system show smaller amplitudes of motion, as a reactionary force is applied in the opposite direction of the WEC's motion. In addition, the bigger the c_{PTO} value is, the smaller the amplitude of motion. However, it is observed that with the PTO influence, the WEC's heave amplitude decreases more in the ascending movement than in the descending movement.

To study how the pitch angle influences the power extracted from the WEC device some tests are carried out. The waves generated also have H = 2.5 m and T = 5 s. First, a power curve for a case with C_{PTO} = 1000 MNms/rad is shown in Figure 5.25. Simulations are carried out for cases with linear damping coefficients close to zero, with minimal influence on the WEC's heave amplitude, and for cases with high values of the linear damping coefficient, completely restraining the WEC's heave amplitude. The extracted power from the device is calculated, for each case, as seen in Section 3.6.2. A Python code for the power calculation is available in Appendix B.2.

Figure 5.25 shows two different situations where the power extracted is zero. One situation corresponds to the case where the linear damping coefficient is so low that no

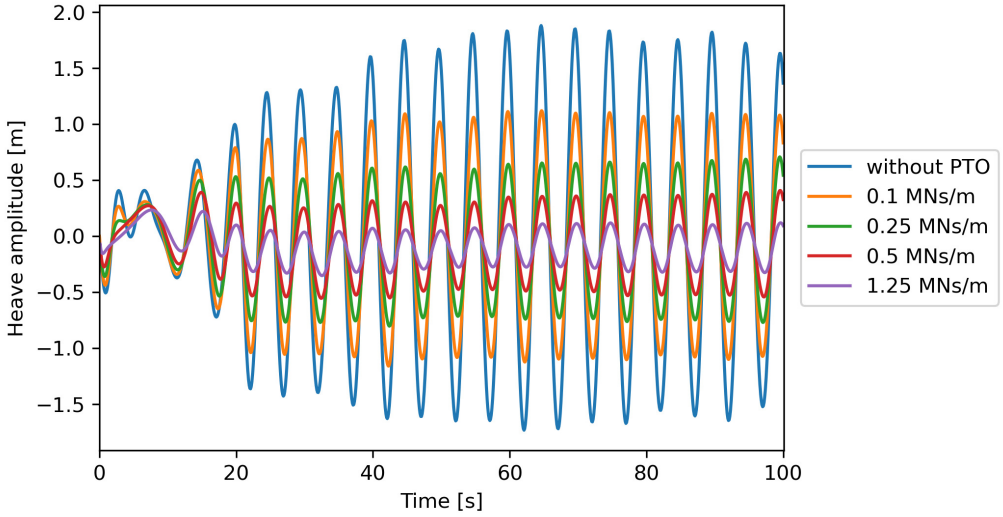

Figure 5.24: Influence of the PTO system in the WEC's heave amplitude.

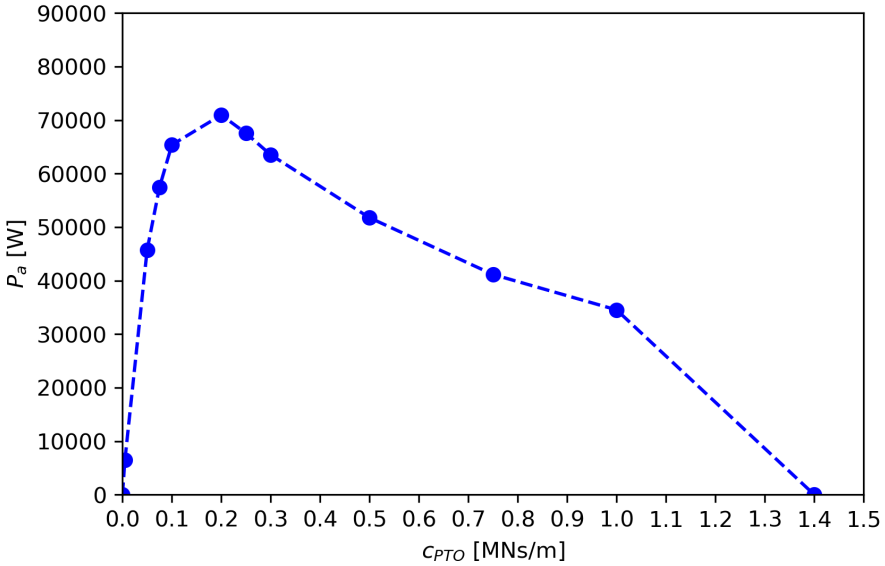

Figure 5.25: Power curve for $C_{PTO} = 1000$ MNms/rad.

power is extracted from the waves, the other situation corresponds to the case where the linear damping coefficient is so high that the WEC is restrained from heaving, and no power is extracted. It is observed that a power peak is achieved for $c_{PTO} = 0.2$ MNms/rad.

After obtaining the first power curve, more tests are carried out. Figure 5.26 shows a comparison between cases with different rotational mechanical constraints. It shows that every case considered presents the same power curve behaviour, but with different values, and a power peak for $c_{PTO} = 0.2$ MNs/m. Although, for lower values of c_{PTO} it is observed that all cases considered show similar power output values. As the objective of the power curve is to obtain the maximum power output, the new curves do not have as many values as Figure 5.25.

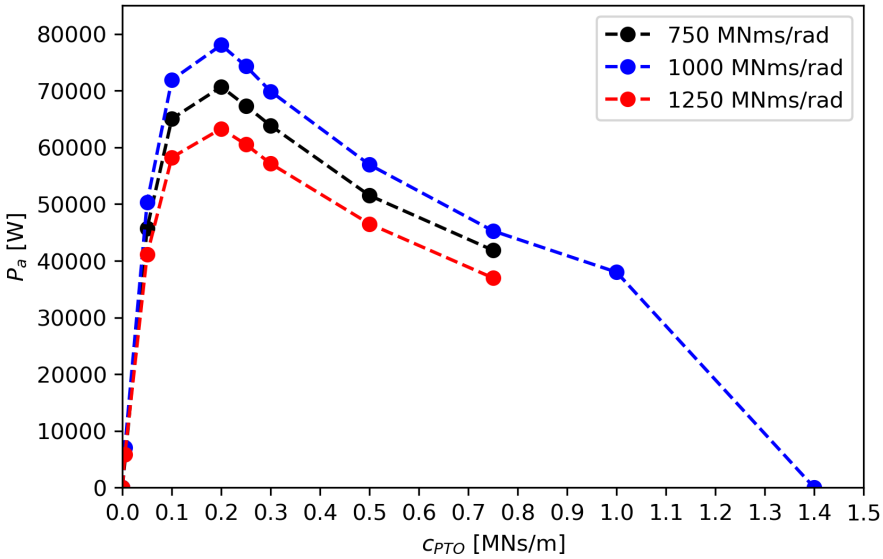

Figure 5.26: Comparison between the power curves, with different C_{PTO} values.

The analysis of Figure 5.26 does not show a linear behaviour for the relation between the extracted power and the rotational mechanical constraint. The results obtained only allow to conclude that, for the cases considered, the optimal value of the rotational mechanical constraint corresponds to C_{PTO} = 1000 MNms/rad, with a maximum extracted power of 78000 W and a linear damping coefficient of c_{PTO} = 0.2 MNs/m.

6

Irregular wave interaction with the WEC device

A real sea state is characterized by waves with different heights, periods and directions. Therefore, in order to simulate real conditions, it is necessary to study the interaction of the WEC device with irregular waves.

The irregular waves were generated considering the Pierson–Moskowitz spectrum, with the parameters shown in Table 6.1. Two different simulations are carried out: the first case is run without PTO system and with no mechanical constraints in the WEC's rotational motion, in the second case the PTO's linear damping coefficient value was c_{PTO} = 0.5 MNs/m and a mechanical constraint for the rotational motion was also set, with C_{PTO} = 1000 MNms/rad.

Figure 6.1 shows a plot of the free surface elevation over the simulation time at x = 35 meters (from the wave maker). Figure 6.2 and Figure 6.3 show the heave amplitude and the pitch angle of the WEC for the different cases, respectively.

The analysis of Figure 6.1 allows to conclude that neither the PTO system nor the rotational motion mechanical constraint have a significant influence in the free surface elevation of a location upstream of the WEC. However, some differences can be seen. This can be explained by the fact that in the second case there is power extraction, and consequently, the device motion is slightly different of the first case. This difference in the device motion will change the way waves are reflected on the device, which has a slight influence in the free surface elevation on the chosen location.

Figure 6.2 shows that the PTO system has a significant influence in the heave amplitude of the device, decreasing the amplitude of motion, as seen in Section 5.2.2. Analogously, Figure 6.3 shows that the mechanical constraint on the rotational motion decreases

Table 6.1: Irregular waves parameters used on the Pierson–Moskowitz spectrum.

H_s (m)	2.5
T_p (s)	7.5
h (m)	30

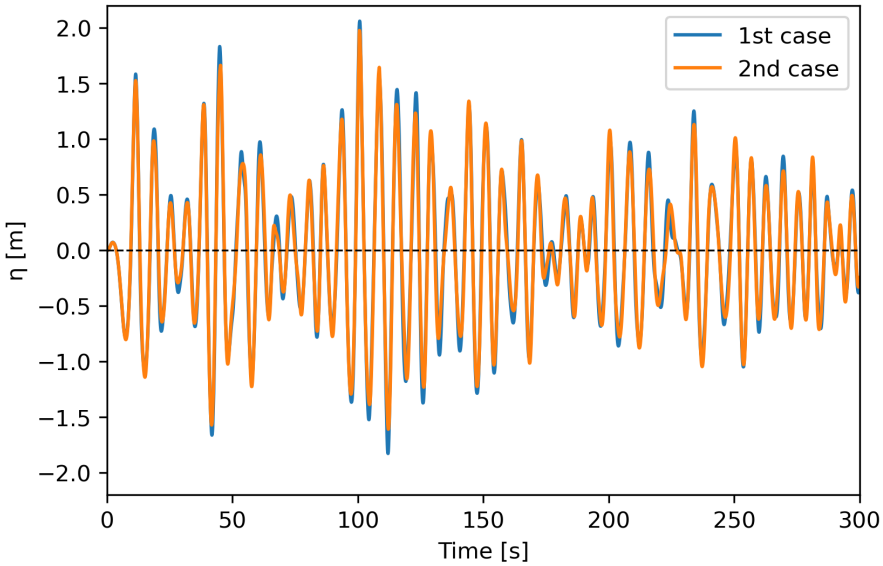

Figure 6.1: Free surface elevation comparison.

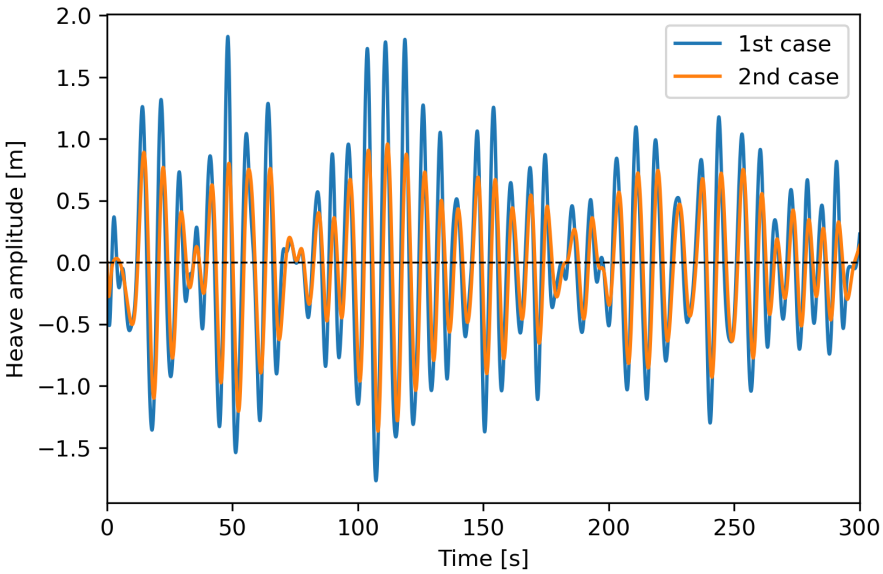

Figure 6.2: Heave amplitude comparison.

the pitch angle of the device significantly.

Figure 6.4, Figure 6.5 and Figure 6.6 show the free surface elevation $S_\eta(f)$, heave amplitude $S_y(f)$ and pitch angle $S_\theta(f)$ power spectrum, respectively.

The analysis of these Figures allows to conclude that the power spectrums are influenced by the PTO and the mechanical constraint on the rotational motion. The peaks of the power spectrums decrease for the second case, which can be explained by the power absorbed by the PTO and the power dissipated by the mechanical constraint. A second peak of frequency is also observed, with frequency values of $f \approx 0.06$ Hz, visible in the first case of Figure 6.6. This second peak can be partially explained by the non-linear

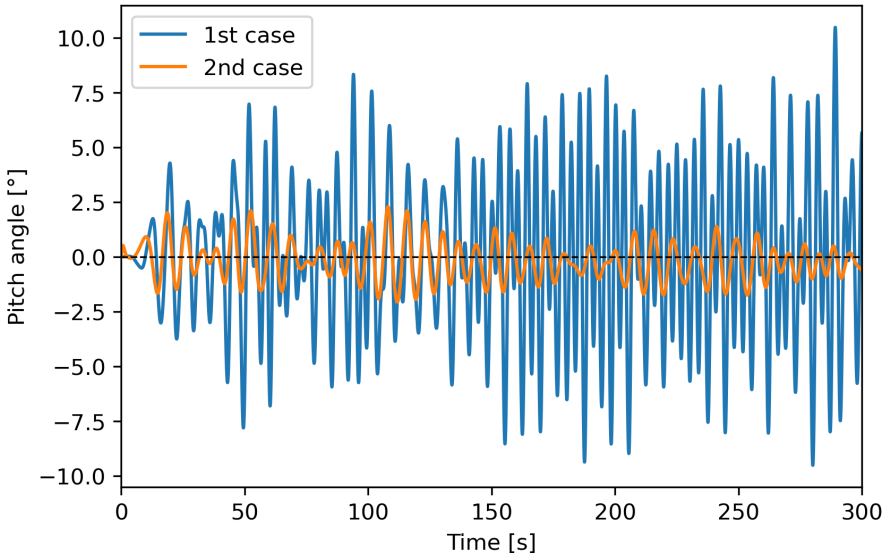

Figure 6.3: Pitch angle comparison.

behaviour of the fluid-floater interaction, which causes the formation of little vortices in the fluid. A deviation about the peak frequency is also observed between the cases in Figure 6.5, which supports the non-linearity of the device motion.

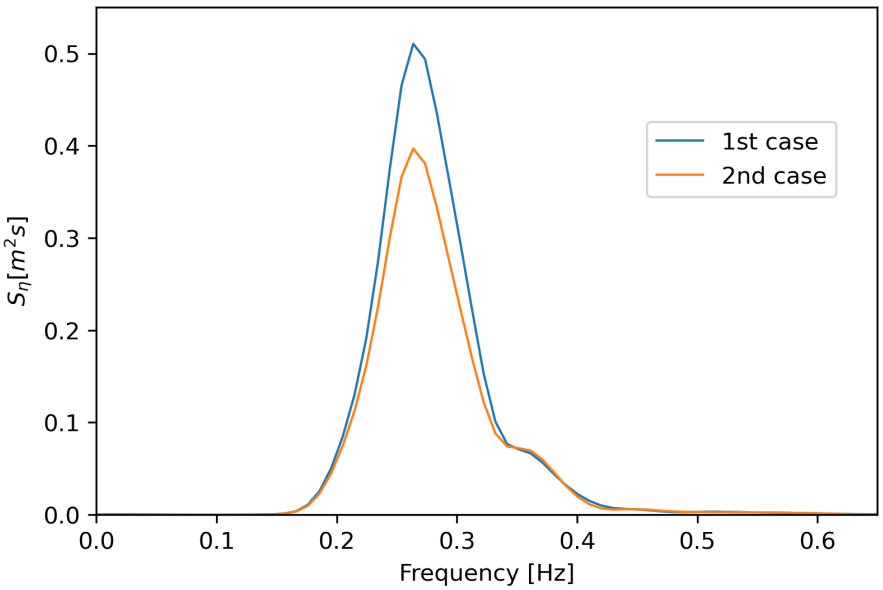

Figure 6.4: Free surface elevation power spectrum.

In order to analyse the dynamic behaviour of the WEC under irregular waves the RAO parameter is also used, given by:

$$RAO(f) = \sqrt{\frac{S_y(f)}{S_\eta(f)}} \tag{6.1}$$

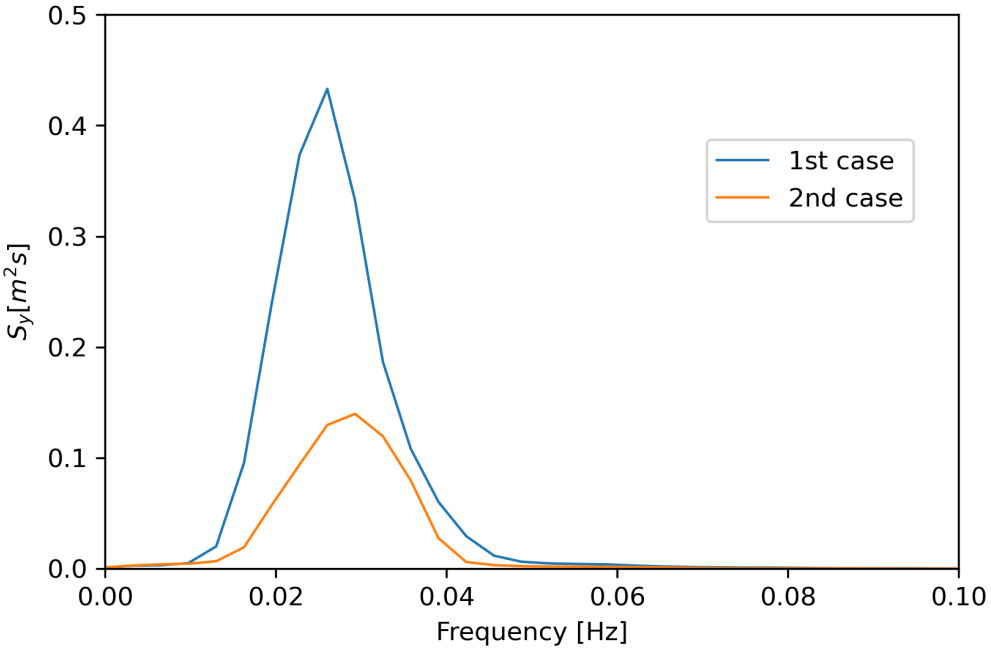

Figure 6.5: Heave amplitude power spectrum.

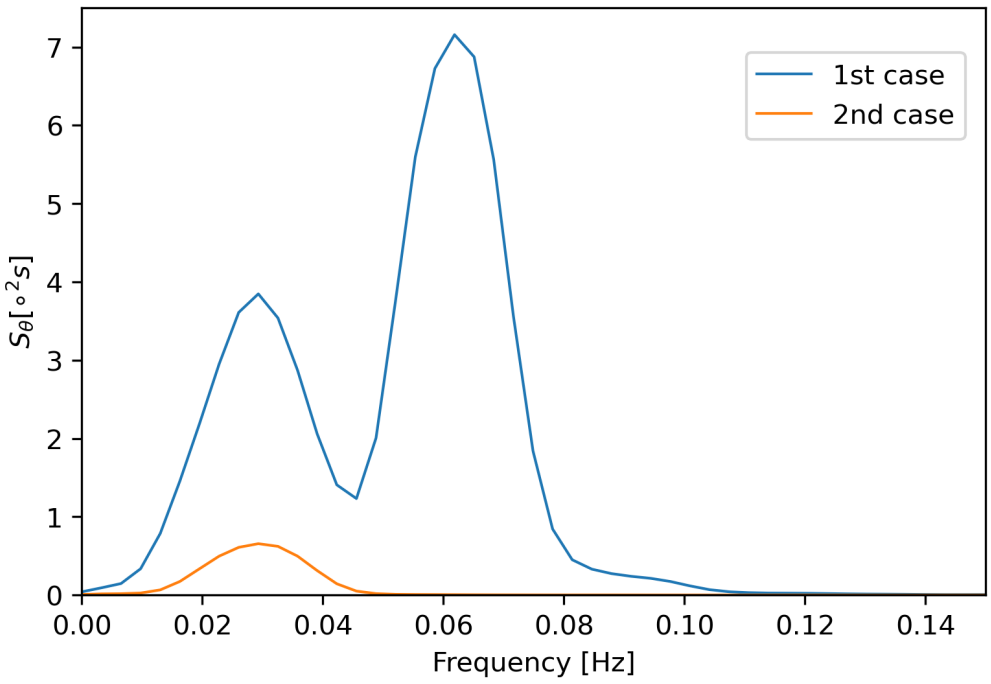

Figure 6.6: Pitch angle power spectrum.

From the analysis of Figure 6.7 it is observed that the RAO parameter is also influenced by the PTO system, as the second case has a lower peak than the first. A deviation between peak frequencies is also observed, confirming the non-linearity of the device motion.

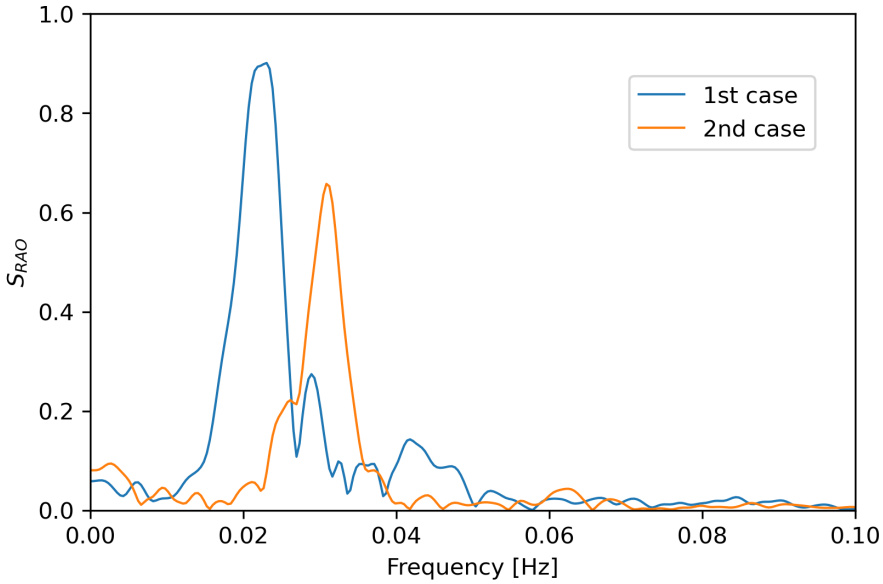

Figure 6.7: RAO power spectrum.

The power absorbed by the WEC over the simulation time, for the second case considered, is illustrated in Figure 6.8. The calculated value of the mean power absorbed by the WEC, for the simulation time, is $\overline{P}_a = 71.6$ kW.

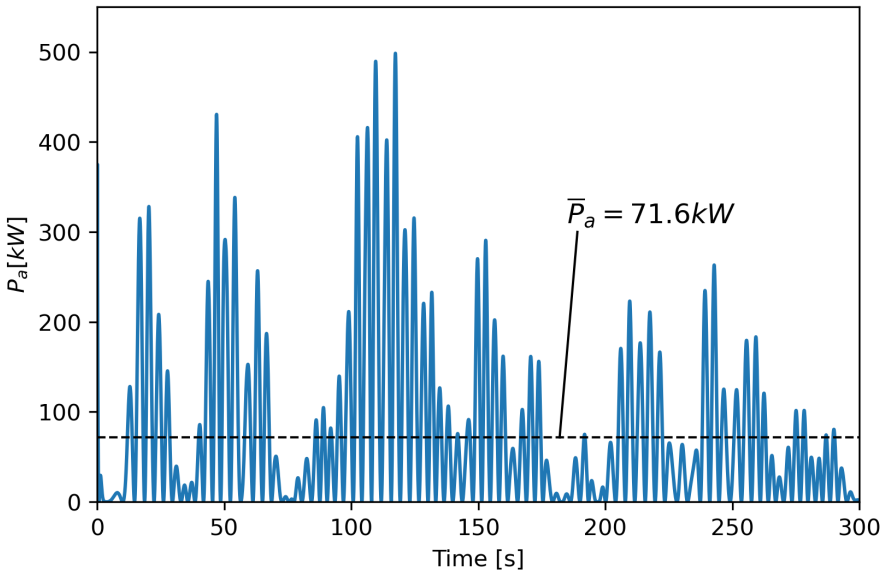

Figure 6.8: Power absorbed by the WEC under irregular waves.

7

Conclusions and Future Developments

The main objective of this work was to study the hydrodynamic behaviour of a WEHC. The study focused on characterising the WEHC's behaviour under regular and irregular waves, considering cases with and without the PTO system. All the numerical simulation process was executed using the open-source CFD software OpenFOAM, augmenting its functionalities using olaFlow's library for the generation and propagation of waves.

The considered WEC geometry is a simplification of a WEHC, as the lever arm was not considered, only the floater. Initially, the validation of wave generation and propagation is performed and then, a mesh convergence study is carried out.

Afterwards, the regular wave interaction with the WEC device contains a free heave and pitch decay test. Then, the period and wave height influence on the dynamic behaviour of the WEC is studied. After, simulations with the PTO system are performed, with the power extracted and the optimal linear damping coefficient being presented.

Finally, the influence of the PTO system when the WEC is under irregular waves is characterized.

7.1 Main conclusions

The main conclusions drawn from the obtained results of the studies performed are presented bellow.

7.1.1 Regular wave interaction with the WEC device

This study focused in analysing the WEC's behaviour under regular waves.

7.1.1.1 Simulations without the PTO system

Initially, a free heave and pitch decay test are carried out to calculate the WEC's natural period. The velocity and pressure fields of these tests are studied and, as no vortices are observed in the WEC's vicinity for both cases, it leads to the conclusion that considering a

laminar flow is a valid assumption. Next, the heave and pitch motion around the WEC's heave and pitch natural period is studied. Results show that, for the cases considered, the heave amplitude systematically increases with the increase of the wave period, around the WEC's heave natural period. It was expected that, due to the resonance effect, the heave and pitch amplitude would be largest for the cases which correspond to the heave and pitch natural periods, respectively. Nonetheless, as the heave and pitch natural periods are calculated with only 1 DoF, and in this study the WEC is allowed to heave and pitch, the expected results are not verified. These results allow to conclude that the pitch movement modified the heave natural period and the heave movement modified the pitch natural period of the WEC.

Next, the period and wave height influence on the WEC's heave and pitch amplitude is analysed. Results show that both cases considered are in resonance with the waves, showing a higher heave amplitude, for frequencies around 0.20 Hz (T = 5 s). An amplitude peak is also observed for lower frequencies, which can be explained taking into account that for longer period waves (lower frequencies), the WEC moves linearly with the free surface motion, following the waves movement. On the contrary, for higher frequencies (shorter waves) the WEC cannot follow the free surface motion, as the waves' length is smaller than the WEC's diameter, decreasing its amplitude motion. The obtained results show that for higher wave heights, the WEC device also responds with higher amplitudes of motion however, for higher frequencies (around 0.34 Hz), the two cases overlap.

The RAO parameter is used to better represent the dynamic behaviour of the WEC. The comparison between the RAO parameter for the considered cases allows to conclude that the wave height does not have a significant influence in RAO, meaning that an increase in the WEC's heave amplitude is linearly proportional to the increase in the wave height.

As the wave height value introduced in OpenFOAM can slightly differ from the wave height actually generated, some modifications are performed and the RAO is considered to be the ratio between the WEC's heave amplitude and the measured wave height. The modified RAO parameter is calculated for three different locations and for the mean value of the free surface elevation for the three locations. Results show that the RAO parameter is very distinct, according to the location. Consequently, it is concluded that there is a large variation of the free surface elevation along the NWT, due to the reflection of waves on the device. All cases show an amplitude peak for frequencies around 0.20 Hz.

The pitch angle variation is also studied to improve the understanding of the dynamic behaviour of the WEC. A pitch angle peak for frequencies around 0.28 Hz is observed for both cases considered. The pitch angle shows minor variations for both lower frequencies (longer waves) and higher frequencies (shorter waves). This behaviour can be explained taking into account that for longer period waves (lower frequencies) the wave steepness is small, allowing the WEC to follow the free surface motion, only having small variations in the pitch angle. For shorter period waves (higher frequencies), as the wave length is smaller than the WEC's diameter, the WEC has multiple wave crests under it, which

restrains its rotation, leading to small variations in the pitch angle.

A comparison between the WEC's RAO and pitch angle is also performed. The obtained results suggest that a decrease in the pitch angle can lead to an increase in the heave amplitude.

7.1.1.2 Simulations with the PTO system

This study is carried out considering a double-acting PTO system, i.e., the PTO applies the damping force in both directions. First, the influence of the linear damping coefficient is studied. A case without PTO system is compared to cases with PTO system, but with different c_{PTO} values. Obtained results show that cases with a PTO system have smaller amplitudes of motion and, in addition, the bigger the c_{PTO} value is, the smaller the amplitude of motion. It is also observed that the WEC's heave amplitude shows a bigger decrease in the ascending movement than in the descending movement.

The power extracted from the WEC device is also studied. First, a power curve with a rotational mechanical constraint, with C_{PTO} = 1000 MNms/rad, is obtained. It shows two different situations where the power extracted is zero: the first corresponds to the case with a linear damping coefficient close to zero and the second to the case with high values of the linear damping coefficient, restraining the WEC's heave amplitude.

To study how the rotational mechanical constraint influences the power extracted, a comparison between power curves with different C_{PTO} values is performed, with three different cases being considered. Results show that all curves present the same behaviour, with a power peak for c_{PTO} = 0.2 MNs/m.

For the cases considered, no linear relation between the rotational mechanical constraint and the power extracted is observed. Results show that, for the considered cases, the optimal rotational mechanical constraint corresponds to C_{PTO} = 1000 MNms/rad, with a maximum power extracted of 78000 W and a linear damping coefficient of c_{PTO} = 0.2 MNs/m.

7.1.2 Irregular wave interaction with the WEC device

This study focused in analysing the WEC's behaviour under irregular waves. Two different simulations are carried out: the first case is run without PTO system and with no mechanical constraints in the WEC's rotational motion, whereas the second case has a PTO system and a rotational mechanical constraint.

Results show that neither the PTO system nor the rotational mechanical constraint have a significant influence in the free surface elevation of a location upstream of the WEC (x = 35 meters, from the wave maker). It is also seen that the PTO system has a significant influence in the heave amplitude of the device, decreasing its amplitude of motion. In addition, the rotational mechanical constraint also decreases the pitch angle of the device considerably.

The obtained results show that the power spectrums are influenced by the PTO and the rotational mechanical constraint, as the power spectrums peak decrease for the second case considered. The non-linearity of the fluid-floater interaction is also observed, as there is a deviation about the peak frequency in the heave amplitude and RAO power spectrums.

Finally, the mean power absorbed by the WEC device, for the simulation time, is $\overline{P}_a = 71.6$ kW.

7.2 Future work

This study focused on developing a NWT to study the hydrodynamic behaviour of a WEHC that can be coupled with a floating SSP. Some possible future developments of this work are presented bellow:

- This work had the objective to study both the heave and pitch movement of a WEHC. Initially, the floater and the lever arm were introduced in the computational domain, but as it was not possible to simulate an articulation between both, the geometry was simplified only to the floater. However, to study the hydrodynamic behaviour of a WEHC it is of utmost importance to introduce both the floater and the lever arm, integrated with the articulation, in the computational domain.
- The interaction between devices influences their hydrodynamic behaviour so, a study that could introduce multiple WEHCs in the computational domain, to study their interaction, is highly recommended.
- Finally, to study a full hybrid device, a WEHC coupled with a SSP, it should be tried to introduce both in the computational domain and study their hydrodynamic behaviour. In a more advanced study, multiple WEHCs could be coupled with a SSP.

Bibliography

[1] J. M. Lourenço. *The NOVAthesis LaTeX Template User's Manual*. NOVA University Lisbon. 2021. URL: https://github.com/joaomlourenco/novathesis/raw/master/template.pdf (cit. on p. iii).

[2] EIA. "International Energy Outlook 2021". In: *U.S. Energy Information Administration IEO2021 (2021)* (), p. 8. URL: https://www.eia.gov/outlooks/ieo/pdf/IEO2021_ReleasePresentation.pdf (cit. on p. 1).

[3] "UNFCCC (1997) Kyoto Protocol to the United Nations Framework Convention on Climate Change adopted at COP3 in Kyoto, Japan". In: (). URL: https://unfccc.int/resource/docs/convkp/kpeng.pdf (cit. on p. 1).

[4] "Paris Agreement to the United Nations Framework Convention on Climate Change". In: (2015-12-12). T.I.A.S. No. 16-1104. URL: https://unfccc.int/sites/default/files/english_paris_agreement.pdf (cit. on p. 1).

[5] S. Shafiei and R. A. Salim. "Non-renewable and renewable energy consumption and CO2 emissions in OECD countries: A comparative analysis". In: *Energy Policy* 66 (2014), pp. 547–556. ISSN: 0301-4215. DOI: https://doi.org/10.1016/j.enpol.2013.10.064 (cit. on p. 1).

[6] A. S. Bahaj. "Generating electricity from the oceans". In: *Renewable and Sustainable Energy Reviews* 15.7 (2011), pp. 3399–3416. ISSN: 1364-0321. DOI: https://doi.org/10.1016/j.rser.2011.04.032 (cit. on p. 2).

[7] A. F. de O. Falcão. "Wave energy utilization: A review of the technologies". In: *Renewable and Sustainable Energy Reviews* 14.3 (2010), pp. 899–918. ISSN: 1364-0321. DOI: https://doi.org/10.1016/j.rser.2009.11.003 (cit. on p. 2).

[8] *The European Marine Energy Centre Ltd, Wave devices. 2022*. URL: https://www.emec.org.uk/marine-energy/wave-devices/ (visited on 2022-04-14) (cit. on p. 2).

[9] "Wind energy in Europe - 2020 Statistics and the outlook for 2021-2025". In: (2021), p. 14. URL: https://s1.eestatic.com/2021/02/24/actualidad/210224_windeurope_combined_2020_stats.pdf (cit. on p. 2).

[10] C. Pérez-Collazo, D. Greaves, and G. Iglesias. "A review of combined wave and offshore wind energy". In: *Renewable and Sustainable Energy Reviews* 42 (2015), pp. 141–153. ISSN: 1364-0321. DOI: https://doi.org/10.1016/j.rser.2014.09.032 (cit. on pp. 2, 7).

[11] C. M. Wang et al. "Research on floating wind turbines: a literature survey". In: *The IES Journal Part A: Civil & Structural Engineering* 3.4 (2010), pp. 267–277. DOI: 10.1080/19373260.2010.517395. eprint: https://doi.org/10.1080/19373260.2010.517395 (cit. on p. 2).

[12] A. J. Goupee et al. "Experimental comparison of three floating wind turbine concepts". In: *Journal of Offshore Mechanics and Arctic Engineering* 136.2 (2014). URL: https://citeseerx.ist.psu.edu/viewdoc/download?doi=10.1.1.658.1336&rep=rep1&type=pdf (cit. on p. 2).

[13] M. Kamarlouei et al. "Experimental analysis of wave energy converters concentrically attached on a floating offshore platform". In: *Renewable Energy* 152 (2020), pp. 1171–1185. ISSN: 0960-1481. DOI: https://doi.org/10.1016/j.renene.2020.01.078 (cit. on pp. 2, 3).

[14] C. Perez-Collazo, D. Greaves, and G. Iglesias. "Hydrodynamic response of the WEC sub-system of a novel hybrid wind-wave energy converter". In: *Energy Conversion and Management* 171 (2018), pp. 307–325. ISSN: 0196-8904. DOI: https://doi.org/10.1016/j.enconman.2018.05.090 (cit. on p. 2).

[15] H. Zhu and C. Hu. "A Study on Control of Wave Energy Converter for Motion Suppression of Semisubmersible". In: *IFAC-PapersOnLine* 49.23 (2016). 10th IFAC Conference on Control Applications in Marine SystemsCAMS 2016, pp. 380–385. ISSN: 2405-8963. DOI: https://doi.org/10.1016/j.ifacol.2016.10.434 (cit. on pp. 2, 7).

[16] A. Lamei and M. Hayatdavoodi. "On motion analysis and elastic response of floating offshore wind turbines". In: *Journal of Ocean Engineering and Marine Energy* 6 (2020-02). DOI: 10.1007/s40722-019-00159-2 (cit. on p. 3).

[17] G. Hou, J. Wang, and A. Layton. "Numerical Methods for Fluid-Structure Interaction — A Review". In: *Communications in Computational Physics* 12.2 (2012), pp. 337–377. DOI: 10.4208/cicp.291210.290411s (cit. on p. 3).

[18] N. Desmars et al. "Interaction of surface waves with an actuated submerged flexible plate: Optimization for wave energy extraction". In: *Journal of Fluids and Structures* 81 (2018), pp. 673–692. ISSN: 0889-9746. DOI: https://doi.org/10.1016/j.jfluidstructs.2018.05.016 (cit. on p. 3).

[19] I. Collins et al. "Flexible membrane structures for wave energy harvesting: A review of the developments, materials and computational modelling approaches". In: *Renewable and Sustainable Energy Reviews* 151 (2021), p. 111478. ISSN: 1364-0321. DOI: https://doi.org/10.1016/j.rser.2021.111478 (cit. on p. 3).

[20] A. Babarit et al. "A linear numerical model for analysing the hydroelastic response of a flexible electroactive wave energy converter". In: *Journal of Fluids and Structures* 74 (2017), pp. 356–384. ISSN: 0889-9746. DOI: https://doi.org/10.1016/j.jfluidstructs.2017.06.003 (cit. on p. 3).

[21] C. Windt, J. Davidson, and J. V. Ringwood. "High-fidelity numerical modelling of ocean wave energy systems: A review of computational fluid dynamics-based numerical wave tanks". In: *Renewable and Sustainable Energy Reviews* 93 (2018), pp. 610–630. ISSN: 1364-0321. DOI: https://doi.org/10.1016/j.rser.2018.05.020 (cit. on p. 3).

[22] L. Chen et al. "Numerical investigation of wave–structure interaction using OpenFOAM". In: *Ocean Engineering* 88 (2014), pp. 91–109. ISSN: 0029-8018. DOI: https://doi.org/10.1016/j.oceaneng.2014.06.003 (cit. on p. 3).

[23] P. Balitsky, G. Bacelli, and J. Ringwood. "Control-Influenced Layout Optimization of Arrays of Wave Energy Converters". In: *Proceedings of the International Conference on Offshore Mechanics and Arctic Engineering - OMAE* 9 (2014-06). DOI: 10.1115/OMAE2014-24136 (cit. on p. 3).

[24] J. Engström et al. "Performance of large arrays of point absorbing direct-driven wave energy converters". In: *Journal of Applied Physics* 114.20 (2013), p. 204502. DOI: 10.1063/1.4833241. eprint: https://doi.org/10.1063/1.4833241 (cit. on p. 3).

[25] P. Garcia Rosa et al. "Modelagem da dinâmica de um conversor hiperbárico de energia das ondas em energia elétrica". In: (2010-09), pp. 1107–1113. URL: https://www.researchgate.net/publication/262007185_Modelagem_da_dinamica_de_um_conversor_hiperbarico_de_energia_das_ondas_em_energia_eletrica (cit. on pp. 4, 13).

[26] A. Henderson and M. Patel. "On the Modelling of a Floating Offshore Wind Turbine". In: *Wind Energy* 6 (2003-01), pp. 53–86. DOI: 10.1002/we.83 (cit. on p. 7).

[27] T. Hallak et al. "Numerical and Experimental Analysis of a Hybrid Wind-Wave Offshore Floating Platform's Hull". In: (2018-06). DOI: 10.1115/OMAE2018-78744 (cit. on p. 7).

[28] I. López and G. Iglesias. "Efficiency of OWC wave energy converters: A virtual laboratory". In: *Applied Ocean Research* 44 (2014), pp. 63–70. ISSN: 0141-1187. DOI: https://doi.org/10.1016/j.apor.2013.11.001 (cit. on p. 8).

[29] J. P. Kofoed et al. "Prototype testing of the wave energy converter wave dragon". In: *Renewable Energy* 31.2 (2006). Marine Energy, pp. 181–189. ISSN: 0960-1481. DOI: https://doi.org/10.1016/j.renene.2005.09.005 (cit. on p. 9).

[30] S. Ding, D. Han, and Y. Zan. "The application of wave energy converter in hybrid energy system". In: *The Open Mechanical Engineering Journal* 8.1 (2014) (cit. on p. 10).

[31] H. Lee, S. K. Poguluri, and Y. H. Bae. "Performance Analysis of Multiple Wave Energy Converters Placed on a Floating Platform in the Frequency Domain". In: *Energies* 11.2 (2018). ISSN: 1996-1073. DOI: 10.3390/en11020406 (cit. on p. 10).

[32] F. Bernardo. "Estudo numérico da eficiência de um conversor hiperbárico de energia das ondas". MSc thesis. Universidade Nova de Lisboa, 2020 (cit. on pp. 11, 21).

[33] S. Estefen et al. "Design Analyses Applied to a Hyperbaric Wave Energy Converter". In: *11th International Symposium on Practical Design of Ships and Other Floating Structures, PRADS 2010* 2 (2010-07) (cit. on p. 12).

[34] P. Garcia Rosa et al. "Efficiency Optimization in a Wave Energy Hyperbaric Converter". In: *2009 International Conference on Clean Electrical Power, ICCEP 2009* (2009-07), pp. 68–75. DOI: 10.1109/ICCEP.2009.5212079 (cit. on p. 13).

[35] J. Falnes. *Ocean Waves and Oscillating Systems: Linear Interaction including Wave-Energy Extraction*. USA: Cambridge University Press, 2002 (cit. on p. 14).

[36] D. V. Evans. "A theory for wave-power absorption by oscillating bodies". In: *Journal of Fluid Mechanics* 77.1 (1976), pp. 1–25. DOI: 10.1017/S0022112076001109 (cit. on p. 14).

[37] M. Pontes, R. Aguiar, and H. Pires. "A Nearshore Wave Energy Atlas for Portugal". In: *Journal of Offshore Mechanics and Arctic Engineering-transactions of The Asme - J OFFSHORE MECH ARCTIC ENG* 127 (2005-08). DOI: 10.1115/1.1951779 (cit. on pp. 15, 16).

[38] Z. Xu, Z. Han, and H. Qu. "Comparison between Lagrangian and Eulerian approaches for prediction of particle deposition in turbulent flows". In: *Powder Technology* 360 (2020), pp. 141–150. ISSN: 0032-5910. DOI: https://doi.org/10.1016/j.powtec.2019.09.084 (cit. on p. 16).

[39] E. B. Agamloh, A. K. Wallace, and A. von Jouanne. "Application of fluid–structure interaction simulation of an ocean wave energy extraction device". In: *Renewable Energy* 33.4 (2008), pp. 748–757. ISSN: 0960-1481. DOI: https://doi.org/10.1016/j.renene.2007.04.010 (cit. on p. 17).

[40] T. Tan Loh et al. "Numerical Modelling of the WaveRoller Device Using OpenFOAM". In: (2016-10). DOI: 10.3850/978-981-11-0782-5_61 (cit. on p. 17).

[41] Y. Luo et al. "Numerical simulation of a heave-only floating OWC (oscillating water column) device". In: *Energy* 76 (2014), pp. 799–806. ISSN: 0360-5442. DOI: https://doi.org/10.1016/j.energy.2014.08.079 (cit. on p. 17).

[42] R. A. Gingold and J. J. Monaghan. "Smoothed particle hydrodynamics: theory and application to non-spherical stars". In: *Monthly Notices of the Royal Astronomical Society* 181.3 (1977-12), pp. 375–389. ISSN: 0035-8711. DOI: 10.1093/mnras/181.3.375 (cit. on p. 17).

[43] M. Becker and M. Teschner. "Weakly Compressible SPH for Free Surface Flows". In: *Proceedings of the 2007 ACM SIGGRAPH/Eurographics Symposium on Computer Animation* 9 (2007-01), pp. 209–217. DOI: 10.1145/1272690.1272719 (cit. on p. 17).

[44] D. Jackson and B. Launder. "Osborne Reynolds and the Publication of His Papers on Turbulent Flow". In: *Annual Review of Fluid Mechanics* 39.1 (2007), pp. 19–35. DOI: 10.1146/annurev.fluid.39.050905.110241 (cit. on p. 18).

[45] I. M. Cohen and P. K. Kundu. *Fluid mechanics*. Elsevier, 2004 (cit. on p. 19).

[46] L. Holthuijsen. "Waves in Oceanic and Coastal Waters". In: *Waves in Oceanic and Coastal Waters, by Leo H. Holthuijsen, pp. 404. Cambridge University Press, January 2007. ISBN-10: . ISBN-13:* (2007). DOI: 10.2277/0521860288 (cit. on pp. 20, 21, 23, 24).

[47] B. L. Méhauté. *An introduction to hydrodynamics and water waves*. Springer Science & Business Media, 2013 (cit. on p. 22).

[48] W. J. Pierson Jr and L. Moskowitz. "A proposed spectral form for fully developed wind seas based on the similarity theory of SA Kitaigorodskii". In: *Journal of geophysical research* 69.24 (1964), pp. 5181–5190 (cit. on p. 23).

[49] U. A. C. of Engineers. "USACE (U.S. Army Corps of Engineers)". In: *1110-2-1100* (2006) (cit. on p. 24).

[50] *CFD Direct - The Architects of OpenFOAM, About OpenFOAM*. URL: https://cfd.direct/openfoam/about/ (visited on 2022-06-20) (cit. on p. 25).

[51] "OpenFOAM - The OpenFOAM Foundation - User Guide, version 9." In: (2021). URL: http://foam.sourceforge.net/docs/Guides-a4/OpenFOAMUserGuide-A4.pdf (cit. on p. 25).

[52] *OpenFOAM - User Guide*. URL: https://www.openfoam.com/documentation/user-guide/contents (visited on 2022-06-14) (cit. on p. 26).

[53] P. Higuera. *olaFlow: CFD for waves [Software]*. 2017. DOI: 10.5281/zenodo.1297013 (cit. on p. 26).

[54] P. Higuera. "Aplicación de la Dinámica de Fluidos Computacional a la Acción del Oleaje Sobre Estructuras". PhD thesis. Universidad de Cantabria, 2015 (cit. on pp. 26–31, 36, 37).

[55] C. Hirt and B. Nichols. "Volume of fluid (VOF) method for the dynamics of free boundaries". In: *Journal of Computational Physics* 39.1 (1981), pp. 201–225. ISSN: 0021-9991. DOI: https://doi.org/10.1016/0021-9991(81)90145-5 (cit. on p. 28).

[56] J. Davidson et al. "Implementation of an OpenFOAM Numerical Wave Tank for Wave Energy Experiments". In: (2015-09) (cit. on pp. 28, 35).

[57] *OpenFOAM Wiki - GroovyBC*. URL: https://openfoamwiki.net/index.php/Contrib/groovyBC (visited on 2022-07-06) (cit. on p. 29).

[58] *OpenFOAM Wiki - waves2Foam*. URL: https://openfoamwiki.net/index.php/Contrib/waves2Foam (visited on 2022-07-06) (cit. on p. 29).

[59] *OpenFOAM Wiki - olaFlow*. URL: https://openfoamwiki.net/index.php/Contrib/olaFlow (visited on 2022-07-06) (cit. on pp. 29, 30).

[60] R. Eymard, T. Gallouët, and R. Herbin. "Finite volume methods". In: Handbook of Numerical Analysis 7 (2000), pp. 713–1018. ISSN: 1570-8659. DOI: https://doi.org/10.1016/S1570-8659(00)07005-8 (cit. on p. 31).

[61] H. K. Versteeg and W. Malalasekera. *An introduction to computational fluid dynamics - the finite volume method*. Addison-Wesley-Longman, 1995, pp. I–X, 1–257. ISBN: 978-0-582-21884-0 (cit. on pp. 31, 38).

[62] L. Chen. "FINITE VOLUME METHODS". In: (). URL: https://www.math.uci.edu/~chenlong/226/FVM.pdf (cit. on p. 32).

[63] S. Rapuc et al. "Towards guidelines for consistent wave propagation in CFD simulations". In: *Technology and Science for the Ships of the Future*. IOS Press, 2018, pp. 515–524 (cit. on pp. 32, 33).

[64] *OpenFOAM - User Guide*. URL: https://www.openfoam.com/documentation/user-guide/a-reference/a.4-standard-boundary-conditions (visited on 2022-07-13) (cit. on p. 33).

[65] *Parameter Definitions - dynamicMotionSolverFvMesh*. URL: https://openfoamwiki.net/index.php/Parameter_Definitions_-_dynamicMotionSolverFvMesh (visited on 2022-04-15) (cit. on p. 35).

[66] ITTC. "Uncertainty Analysis in CFD Verification and Validation - Methodology and Procedures". In: *International Towing Tank Conference* (). URL: https://www.ittc.info/media/8153/75-03-01-01.pdf (cit. on pp. 41, 45).

[67] S. S. Rao and Y. F. Fah. *Mechanical vibrations; 5th ed. in SI units*. Singapore: Prentice Hall, 2011. URL: https://cds.cern.ch/record/1398617 (cit. on p. 49).

A

Bash scripts

```
#!/bin/bash

mkdir 0

echo Preparing 0 folder...
rm -fr 0
cp -r 0.org 0

echo Setting the fields...
setFields > setFields.log

echo Running...

# USER INPUTS ------------------------------------------------------------------
processors=40    # number of PC processors for parallel computation
#-------------------------------------------------------------------------------

decomposePar                                  > log.decomposePar
./cleanData                     > log.cleanData &
mpirun -np $processors olaDyMFlow -parallel  > log.olaFlow
./cleanData_final                > log.cleanData_final
reconstructPar                                > log.reconstructPar

rm -r processor*

./movement_script.sh

echo Simulation complete.
```

Listing A.1: Bash script used to run complete simulations automatically.

```
#!/bin/bash

sleepHours=1

toDeleteFields="alphaPhi0.water p yPlus ddt0(rho,U) ddtCorrDdt0(U)
  ddtCorrDdt0(Uf) meshPhi meshPhiCN_0 phi rAU U_0 Uf Uf_0 V0"
```

```
6
7   echo Deleting fields $toDeleteFields
8   for name in $toDeleteFields; do
9   find ./processor* -name $name -not -wholename "*/0/*" | xargs rm -v
10  done
11  sleep ${sleepHours}h
```

Listing A.2: Bash script used to delete unnecessary variables from time directories during runtime.

```
1   #!/bin/bash
2
3   ###clearDATA###
4   rm -dr data
5   mkdir data
6
7   ###Time###
8   cat log.olaflow | grep -e "^Time = " | cut -d " " -f 3 > data/times_Extract
9
10  ##centreRotation
11  cat log.olaflow | grep 'Centre of rotation' | cut -d '(' -f 2 | tr -d ")" >
      data/centreRotation_Extract
12  awk '(NR-1) % 3 == 0' data/centreRotation_Extract > data/
      centreRotation_Extract1
13  paste data/times_Extract data/centreRotation_Extract1 > data/
      cmMotion_parcial
14  sed -e 's/ [ ]*/\t/g' data/cmMotion_parcial > data/centreRotation
15  sed -i '1i#Time, x, y, z' data/centreRotation
16  rm data/cmMotion_parcial
17  rm data/centreRotation_Extract data/centreRotation_Extract1
18
19  ###centreMass###
20  cat log.olaflow | grep 'Centre of mass' | cut -d '(' -f 2 | tr -d ")" > data
      /centreMass_Extract
21  awk '(NR-1) % 3 == 0' data/centreMass_Extract > data/centreMass_Extract1
22  paste data/times_Extract data/centreMass_Extract1 > data/cmMotion_parcial
23  sed -e 's/ [ ]*/\t/g' data/cmMotion_parcial > data/centreMass
24  sed -i '1i#Time, x, y, z' data/centreMass
25  rm data/cmMotion_parcial
26  rm data/centreMass_Extract data/centreMass_Extract1
27
28  ###orientation###
29  cat log.olaflow | grep 'Orientation' | cut -d '(' -f 2 | tr -d ")" > data/
      orientation_Extract
30  awk '(NR-1) % 3 == 0' data/orientation_Extract > data/orientation_Extract1
31  paste data/times_Extract data/orientation_Extract1 > data/cmMotion_parcial
32  sed -e 's/ [ ]*/\t/g' data/cmMotion_parcial > data/orientation
33  sed -i '1i#Time, ' data/orientation
34  rm data/cmMotion_parcial
35  rm data/orientation_Extract data/orientation_Extract1
```

```
36
37  ##linearVelocity###
38  cat log.olaflow | grep 'Linear velocity' | cut -d '(' -f 2 | tr -d ")" >
      data/linearVelocity_Extract
39  awk '(NR-1) % 3 == 0' data/linearVelocity_Extract > data/
      linearVelocity_Extract1
40  paste data/times_Extract data/linearVelocity_Extract1 > data/
      cmMotion_parcial
41  sed -e 's/ [ ]*/\t/g' data/cmMotion_parcial > data/linearVelocity
42  sed -i '1i#Time, Vx, Vy, Vz' data/linearVelocity
43  rm data/cmMotion_parcial
44  rm data/linearVelocity_Extract data/linearVelocity_Extract1
45
46  ##angularVelocity###
47  cat log.olaflow | grep 'Angular velocity' | cut -d '(' -f 2 | tr -d ")" >
      data/angularVelocity_Extract
48  awk '(NR-1) % 3 == 0' data/angularVelocity_Extract > data/
      angularVelocity_Extract1
49  paste data/times_Extract data/angularVelocity_Extract1 > data/
      cmMotion_parcial
50  sed -e 's/ [ ]*/\t/g' data/cmMotion_parcial > data/angularVelocity
51  sed -i '1i#Time, Wx, Wy, Wz' data/angularVelocity
52  rm data/cmMotion_parcial
53  rm data/angularVelocity_Extract data/angularVelocity_Extract1
54
55  ##damperForces###
56  cat log.olaflow | grep 'Restraint linearDamper' | cut -d '(' -f 2 | tr -d ")
      " > data/damperForces_Extract
57  awk '(NR-1) % 3 == 0' data/damperForces_Extract > data/damperForces_Extract1
58  paste data/times_Extract data/damperForces_Extract1 > data/cmMotion_parcial
59  sed -e 's/ [ ]*/\t/g' data/cmMotion_parcial > data/damperForces
60  sed -i '1i#Time, Fx, Fy, Fz' data/damperForces
61  rm data/cmMotion_parcial
62  rm data/damperForces_Extract data/damperForces_Extract1
63
```

Listing A.3: Bash script used to extract WEC's simulation values.

B

Python scripts

```
import matplotlib.pyplot as plt
from sympy import symbols, nsolve, tanh, solve_linear, pi

H = 0.05
T = 3
w = 2*np.pi/T
d= 0.4
L = symbols('L')
sol = nsolve(((9.81*T**(2))/(2*pi))*tanh(2*pi*d/L)-L,1000)
L = float(sol)
k = 2*np.pi/L

x_lim =9.01
y_lim = 0.04
t = np.arange(0, 9.1, 0.01);


amplitude1    = (H/2)*np.cos(2*np.pi/T*t)
amplitude2    = k*(H/2)**(2)*np.cosh(k*d)/(4*(np.sinh(k*d))**(3))*(2+np.cosh
  (2*k*d))*np.cos(2*w*t)
amplitude3    = (H/2)*np.cos(w*t)+k*(H/2)**(2)*np.cosh(k*d)/(4*(np.sinh(k*d))
  **(3))*(2+np.cosh(2*k*d))*np.cos(2*w*t)


plt.plot(t, amplitude1, label='linear theory')
plt.plot(t, amplitude2, label = 'Stokes correction')
plt.plot(t, amplitude3, label = 'Stokes II wave')


font = {'family': 'serif',
  'color':  'darkred',
  'weight': 'normal',
  'size': 14,
}

plt.title('Stokes II wave')
```

```
  plt.xlabel('Time (s)')
  plt.ylabel('\u03B7 (m)')
  plt.xlim(0,x_lim)
  plt.ylim(-y_lim,y_lim)
  plt.legend(bbox_to_anchor=(1.01,0.5), loc="center left")
  plt.savefig("stokesII_wave.png", dpi=300, bbox_inches="tight")
  plt.show()
```

Listing B.1: Python script used to plot Stokes II wave.

```
def calc_power(drive):
  text_file = open(drive + "\data\\times_Extract")
  time_lines = text_file.read().splitlines()

  name_file = drive + "\\power_calculation.txt"
  file = open(name_file, "w")
  file.close()

  file = open(drive + "\data\\linearVelocity")
  content_velocity = file.readlines()
  file.close()
  file = open(drive + "\data\\damperForces")
  content_damperForces = file.readlines()
  file.close()

  power_total = 0

  for i in range(len(time_lines)):
    time = time_lines[i]
    line = content_velocity[i + 1]
    values = line.split()
    velocity_value = values[3]
    line = content_damperForces[i + 1]
    values = line.split()
    damper_value = values[3]
    power = abs(float(velocity_value)*float(damper_value))#*(10**(-3))
    power_total = power_total + power
    file = open(name_file, "a")
    file.write(time + " " + velocity_value + " " + damper_value + " " + str(
    power) + "\n" )
    file.close()
```

Listing B.2: Python script used to calculate the WEC's power output.

C

OpenFOAM files

```
1
2  /*--------------------------------*- C++ -*----------------------------------*\
3  | =========                 |                                                 |
4  | \\      /  F ield         | OpenFOAM: The Open Source CFD Toolbox           |
5  |  \\    /   O peration     | Version:  5                                     |
6  |   \\  /    A nd           | Web:      www.OpenFOAM.org                      |
7  |    \\/     M anipulation  |                                                 |
8  \*---------------------------------------------------------------------------*/
9  FoamFile
10 {
11   version     2.0;
12   format      ascii;
13   class       dictionary;
14   object      motionProperties;
15 }
16 // * * * * * * * * * * * * * * * * * * * * * * * * * * * * * * * * * * * * * * * * *
       //
17
18 dynamicFvMesh       dynamicMotionSolverFvMesh;
19
20 motionSolverLibs    ("libsixDoFRigidBodyMotion.so");
21
22 motionSolver        sixDoFRigidBodyMotion;
23
24 sixDoFRigidBodyMotionCoeffs
25 {
26   patches         (floatingObject);
27   innerDistance   0.25;
28   outerDistance   6.00;
29
30   centreOfMass    (65 0 29.76);
31
32
33   // Density of the solid
34   rhoSolid        638;
35
```

```
36    // Cuboid mass
37    mass            86896.99;
38
39    // Cuboid moment of inertia about the centre of mass
40    momentOfInertia ( 520386.50 520386.50 991522.61);
41
42    report          on;
43    accelerationRelaxation 0.05;
44    accelerationDamping 0.9;
45
46    solver
47    {
48      type Newmark;
49    }
50
51    constraints
52    {
53      fixedLine
54      {
55        sixDoFRigidBodyMotionConstraint line;
56        centreOfRotation (65 0 31.8);
57        direction (0 0 1);
58      }
59
60      fixedAxis
61      {
62        sixDoFRigidBodyMotionConstraint axis;
63        axis (0 1 0);
64      }
65    }
66
67    restraints
68    {
69      linearDamper
70      {
71        sixDoFRigidBodyMotionRestraint  linearDamper;
72        coeff             500000;
73      }
74
75      sphericalAngularDamper
76      {
77        sixDoFRigidBodyMotionRestraint        sphericalAngularDamper;
78        coeff                                 1000000000;
79      }
80    }
81
82  }
83
84
```

```
// ************************************************************************
    //
```

Listing C.1: dynamicMeshDict file

```

/*--------------------------------*- C++ -*----------------------------------*\
| =========                 |                                                 |
| \\      /  F ield         | OpenFOAM: The Open Source CFD Toolbox           |
|  \\    /   O peration     | Version:  5                                     |
|   \\  /    A nd           | Web:      www.OpenFOAM.org                      |
|    \\/     M anipulation  |                                                 |
\*---------------------------------------------------------------------------*/
FoamFile
{
  version     2.0;
  format      ascii;
  class       dictionary;
  location    "system";
  object      fvSchemes;
}
// * * * * * * * * * * * * * * * * * * * * * * * * * * * * * * * * * * * * *
   //

ddtSchemes
{
  default         CrankNicolson 0.5;
}

gradSchemes
{
  default         Gauss linear;
}

divSchemes
{
  div(rhoPhi,U)  Gauss limitedLinearV 1;
  div((rhoPhi|interpolate(porosity)),U)  Gauss vanLeerV;
  div(phi,alpha)  Gauss vanLeer;
  div(phirb,alpha) Gauss linear;
  div(phi,k)      Gauss upwind;
  div(phi,epsilon) Gauss upwind;
  div(((rho*nuEff)*dev2(T(grad(U))))) Gauss linear;
}

laplacianSchemes
{
  default         Gauss linear corrected;
}

interpolationSchemes
```

```
46   {
47     default          linear;
48   }
49
50   snGradSchemes
51   {
52     default          corrected;
53   }
54
55
56   // ************************************************************************
        //
57
```

Listing C.2: fvSchemes file

```
1  /*--------------------------------*- C++ -*----------------------------------*\
2  | =========                 |                                                 |
3  | \\      /  F ield         | OpenFOAM: The Open Source CFD Toolbox           |
4  |  \\    /   O peration     | Version:  5                                     |
5  |   \\  /    A nd           | Web:      www.OpenFOAM.org                      |
6  |    \\/     M anipulation  |                                                 |
7  \*---------------------------------------------------------------------------*/
8  FoamFile
9  {
10   version     2.0;
11   format      ascii;
12   class       dictionary;
13   location    "system";
14   object      fvSolution;
15 }
16 // * * * * * * * * * * * * * * * * * * * * * * * * * * * * * * * * * * * * * *
       //
17
18 solvers
19 {
20   "alpha.water.*"
21   {
22     nAlphaCorr      2;
23     nAlphaSubCycles 1;
24     cAlpha          1;
25
26     MULESCorr       yes;
27     nLimiterIter    5;
28     alphaApplyPrevCorr  yes;
29
30     solver          smoothSolver;
31     smoother        symGaussSeidel;
32     tolerance       1e-8;
33     relTol          0;
34   }
```

```
35
36  "pcorr.*"
37  {
38    solver          PCG;
39    preconditioner
40    {
41      preconditioner  GAMG;
42      tolerance       1e-5;
43      relTol          0;
44      smoother        DICGaussSeidel;
45      cacheAgglomeration no;
46    }
47
48    tolerance       1e-05;
49    relTol          0;
50    maxIter         100;
51  }
52
53  p_rgh
54  {
55    solver          GAMG;
56    tolerance       1e-8;
57    relTol          0.01;
58    smoother        DIC;
59  }
60
61  p_rghFinal
62  {
63    solver          PCG;
64    preconditioner
65    {
66      preconditioner  GAMG;
67      tolerance       1e-8;
68      relTol          0;
69      nVcycles        2;
70      smoother        DICGaussSeidel;
71      nPreSweeps      2;
72    }
73
74    tolerance       1e-8;
75    relTol          0;
76    maxIter         20;
77  }
78
79  "(U|k|epsilon)"
80  {
81    solver          smoothSolver;
82    smoother        GaussSeidel;
83    tolerance       1e-6;
84    relTol          0.1;
```

```
85      nSweeps         1;
86    }
87
88    "(U|k|epsilon)Final"
89    {
90      solver          smoothSolver;
91      smoother        GaussSeidel;
92      tolerance       1e-6;
93      relTol          0;
94      nSweeps         1;
95    }
96  }
97
98  PIMPLE
99  {
100   momentumPredictor   no;
101   nOuterCorrectors    3;
102   nCorrectors         1;
103   nNonOrthogonalCorrectors 0;
104   correctPhi          yes;
105   moveMeshOuterCcorrectors yes;
106 }
107
108 relaxationFactors
109 {
110   equations
111   {
112     ".*" 0.8;
113   }
114 }
115
116
117 // ************************************************************************
      //
```

Listing C.3: fvSolution file

2022

Numerical simulation of 3D fluid-structure interaction in floating wave energy converter devices

João Lopes

NOVA

NOVA SCHOOL OF